ACTIVE SILICON PHOTONICS

HYBRID INTEGRATION FOR HIGH-SPEED APPLICATIONS

AND PERFORMANCE EVALUATION AFTER COSMIC ENVIRONMENT

by

Dun Mao

A dissertation submitted to the Faculty of the University of Delaware in partial fulfillment of the requirements for the degree of Doctor of Philosophy in Electrical and Computer Engineering

Spring 2023

ACTIVE SILICON PHOTONICS

HYBRID INTEGRATION FOR HIGH-SPEED APPLICATIONS

AND PERFORMANCE EVALUATION AFTER COSMIC ENVIRONMENT

by

Dun Mao

Approved: ____
Jamie D. Phillips, Ph.D.
Chair of the Department of Electrical and Computer Engineering

Approved: ____
Levi T. Thompson, Ph.D.
Dean of the College of Engineering

Approved: ____
Louis F. Rossi, Ph.D.
Vice Provost for Graduate and Professional Education and Dean of the Graduate College

I certify that I have read this dissertation and that in my opinion it meets the academic and professional standard required by the University as a dissertation for the degree of Doctor of Philosophy.

Signed: ____

Tingyi Gu, Ph.D.
Professor in charge of dissertation

I certify that I have read this dissertation and that in my opinion it meets the academic and professional standard required by the University as a dissertation for the degree of Doctor of Philosophy.

Signed: ____

Matthew Doty, Ph.D.
Member of dissertation committee

I certify that I have read this dissertation and that in my opinion it meets the academic and professional standard required by the University as a dissertation for the degree of Doctor of Philosophy.

Signed: ____

Shouyuan Shi, Ph.D.
Member of dissertation committee

I certify that I have read this dissertation and that in my opinion it meets the academic and professional standard required by the University as a dissertation for the degree of Doctor of Philosophy.

Signed: ____

Po Dong, Ph.D.
Member of dissertation committee

ACKNOWLEDGMENTS

First of all, I want to appreciate my advisor, Dr. Tingyi Gu. Her tremendous, selfless support and guidance lead me to the field of photonics. She is always full of many new ideas and strong scientific motivation to explore cutting-edge science and makes great breakthroughs in this field. A lot of internal and external collaborators are introduced to us to work in the interdisciplinary fields of photonics, optical materials, applied physics, and electrical engineering. I couldn't reach so far without her invaluable support and encouragement all the way.

Then, I would like to express my appreciation to my committee members: Dr. Po Dong, Dr. Matthew Doty, and Dr. Shouyuan Shi. Working as a summer intern at Nokia Bell Labs under the supervision of Dr. Dong, he taught me not only to work hard but also to work smart. His creative ideas on research deeply shocked me. Dr. Doty guided me on the setup of free space laser alignment and provided many valuable suggestions on laser-material interactions. Dr. Shi gave me a lot of useful advice on the design and measurement of high-speed devices and shared many interesting research topics with me.

Also, I want to thank those internal and external collaborators: Dr. Anthony W. Yu, Michael A. Krainak, Serhat Altunc from NASA; Dr. Xiangyu Ma, Dr. Patrick Sohr, Dr. Yong Wang, Dr. Stephanie Law, Hanyuan Gao, Dr. Xinqiao Jia from MSEG department at Udel; Dr. Andrew J. Mercante, Dr. Abu Naim R Ahmed, Dr. Dennis Prather from ECE department at Udel. Without their help, suggestion, and support, my experiment project couldn't run smoothly.

Next, I want to say thanks to those lab members during my PhD study: Dr. Tiantian Li, Dr. Anishkumar Soman, Dr. Chen Cheng, Dr. Yixiu Wang, Dr. Zi Wang, Dr. Kaleem Ullah, Dr. Heijun Jeong, Dr. Feifan Wang, Dr. Guangyang Lin, Dr. Peng Cui, Dr. Hwaseob Lee, Thomas Kananen, Yahui Xiao, Lorry Chang, Haochen Zhao, Xiaofeng Zhu, Tuofu Zhama, Masudur Rahim, Boshu Sun, Zia Uddin, Dustin Fang, Mingkun Chen, and Darren Wu. I appreciate those days and nights working with them on experiments, discussing ideas, and solving problems and doubts.

I want to say thanks to my friends Dr. Jielin Li, Dr. Jie Zhang, Dr. Cheng Zhang, Dr. Liangyi Yue, and Jifeng Liu, who helped me settle down when I first came to this nation and delivered courage during my study. Wish you great success in industry and academia in future.

Also, I want to thank the technical staff from laboratories at UD: Dr. Paul Horng, Dr. Kevin Lister, Dr. Chao Wang, Scott McCracken, Dr. Iulian Codreanu (UD nanofab); Dr. Jing Qu, Dr. Chin Chen Kuo, Gerald Poirier (Advanced Materials Characterization Lab); Dr. Yong Zhao (Keck Center for Advanced Microscopy and Microanalysis) for their experiment support.

I want to thank my previous advisors in my bachelor, master, and post-master periods: Dr. Dapeng Yu, Dr. S.W. Cheung, Dr. Qingfeng Zhang, and Dr. Yifan Chen. They brought me into the fields of telecommunications, RF, and microwave engineering and open the door for research.

Last but not least. Thanks to my parents for their unconditional support. I couldn’t go further without them.

TABLE OF CONTENTS

Appendix

LIST OF TABLES

LIST OF FIGURES

ABSTRACT

Silicon (Si) photonics offers great opportunities for on-chip optical interconnects, optical communications, signal processing, and sensing for its advantages of complementary metal-oxide semiconductor (CMOS)-compatibility, high yield, low power consumption, and high data rates. However, conventional Si photonics components may have bottlenecks due to the limited material property of silicon for high-speed, high efficient, and tunable operations. Also, the performance reliability of silicon devices under harsh (such as cosmic) environments is unknown. This thesis focuses on a few topics addressing those concerns. First, it evaluates the performance change of silicon Mach-Zehnder Modulators after cosmic radiation, laying a fundamental step for future deploying silicon based on chip optical communications in aerospace. Then, the hybrid integration of low-dimensional materials on silicon is demonstrated for high-speed optoelectronic devices and all-optical trimming devices. Last, direct laser writing technique is proposed to have direct patterning and material phase change on some thin film materials for low-cost and mask-free device patterning and tunable device applications.

Chapter 1

INTRODUCTION

1.1 Overview

The tremendously increasing needs for data require a rapid evolution of optical communications for a higher data transmission capacity [1]. This makes the conventional fiber-optic communication systems reach the bottleneck for the increasing needs. Utilizing the CMOS manufacturing processes, photonics integrated circuits (PICs) can provide high yields and large-scale integration of components in photonic circuits.

Silicon (Si) photonics is the optical analogy of microelectronics. Using mature CMOS-compatible technology, complex structures could be created, thereby leading to orders-of-magnitude reduction of communication system components in size, power, and cost [2]. The generation, processing, and transmission of optical signals on silicon platforms are extensively studied and developed for various low loss, low power consumption, and high-speed optoelectronic applications. It has been recognized as an advanced technology for applications of data-center communication, Aerospace communication, LiDAR, sensing, imaging, etc. [3]

1.2 Motivation and challenges

For the application scenario of aerospace communication, conventional microwave/RF communication has limited data rates and relatively large transceiver components, high power consumption, and cost [4]. For future improving communication speed and quality, the next generation of on-chip silicon optical communications with the advantages of compact size, low weight, and high speed is necessary to be deployed [4]. While in an aerospace environment, cosmic rays and ions may have radiation effects to affect the performance of chip-scale silicon photonic devices. The performance reliability of silicon photonics after real cosmic radiation is unknown and needs investigation.

With the increasing need for more data, high-speed optical transceivers in data centers are fast developing and in high demand. High-speed modulators and photodetectors are important modules in optical transceivers. Using CMOS technology, silicon photonics brings benefits of high yields, low-cost and high integration to photonic integrated circuits. High-speed devices such as modulators and photodetectors based on silicon photonic platforms are highly developing. For the intrinsic material properties of silicon, it has some inherent limitations for optoelectronic applications. Such as silicon modulators, its modulation efficiency is limited by the nonlinear carrier plasma effect [5][6]; and high-speed response is limited by the RC constant and the limited hole and electron mobility. Design tradeoffs exist in the performance matrix of silicon modulators [7]-[10]. For carrier depletion-based high-speed modulators (such as Mach-Zehnder modulator), to reduce RC constant for high-speed, decreased doping levels in *p-n* junction may reduce capacitance and loss, but the resistance will be increased [9]. For micro-ring modulators, to achieve reduced RC constant for high-speed response and high modulation efficiency, increasing the doping concentration of *p-n* junction is desired, but with the penalty of reduced quality factors and loss [10]. Seeking alternative ways that are capable of high-speed operation is in demand.

Introducing novel materials with unique properties is one of the promising options to improve the performance of silicon devices. Low-dimensional materials are a type of crystals that are covalently bonded in-plane and held together out-of-plane. Emerging low dimensional materials with different bandgaps spanning from metals to semiconductors and insulators make them interact with light over a very wide range of the electromagnetic spectrum from visible, to infrared, even to microwave regimes. Those materials are easily transferred to photonic structures (e.g., waveguides, cavities) to enhance the light-material interactions. Vertical hetero-structure can be constructed by transferring different materials on silicon [11].

Graphene (G) is two-dimensional (2D) material which attracts tremendous research attention owning to its unique properties such as high mobility, good thermal conductivity, etc. As the zero-bandgap material, it's able to interact with light from microwave to ultraviolet wavelengths, making it very promising for light detection, modulation, etc [11]. Research work has demonstrated its intrinsic bandwidth of up to 500 GHz due to its high mobility [12]. By tuning its Fermi level and carrier density, Graphene can work as a modulator [13]. There are many works for G-based modulators, most of them using the carrier accumulation scheme in which an oxide layer is placed between an optical waveguide and graphene [14][15][16]. This can largely accumulate carriers to have high modulation efficiency but suffers from limited bandwidth due to the large capacitance from the oxide layer. There are spaces (e.g., change hybrid device configuration other than carrier accumulation scheme) to improve for high-speed G-based modulators [17].

Nanofabrication-induced random variation brings unwanted resonance deviation of silicon (Si) microring resonators (MRRs) that limits the applications of modulators and lasers in photonic integrated circuits. Conventional resonance tuning methods such as using phase change materials, material strain, carrier injection, and thermal tuning may have the limits of extra loss, inefficient tuning, or large device footprint [18]-[21]. With unique properties such as potential photocatalytic reactions, 2D materials can be easily integrated on CMOS-compatible silicon platforms and can be tuned the response. Group VI element tellurium (Te) with one-dimensional chiral atomic structure has recently received a broad range of attention from electronic, optoelectronic to piezoelectric applications. Especially, the reduced number of layers and van der Waals structure significantly modify the band diagram and enable novel optical nonlinear responses. The potential photocatalytic reactions of Tellurium integrated on a silicon platform to tune the optical response of resonators need to be investigated.

There is an increasing need for low-cost and versatile micro-device fabrication and material processing. By controlling the dosage, the nanosecond pulsed laser can interact with materials with photo-thermal process-enabled ablation patterning and non-thermal melting-based phase change. A direct laser platform should be proposed to have a low-cost and mask-free fabrication process and material processing.

1.3 Thesis outline and original contribution

To address the challenges mentioned in the previous section, this work mainly focuses on a few topics related to silicon photonics and applications of laser writing technique: the performance evaluation of silicon modulators after cosmic radiation; materials (graphene, tellurium) hybrid integration on a silicon platform for high-speed optoelectronic devices and all-optical applications. At last, the laser writing technique for micro-device patterning and material phase change has been demonstrated. Specifically:

Chapter 2 mainly introduces fundamentals related to research topics, including a few active and passive components in silicon photonics, such as Mach-Zehnder interferometers, ring resonators, and modulators. Low-dimensional materials (such as graphene, Tellurium, and phase change materials) with unique properties are introduced since they may bring advantages and opportunities for functional electro-optical devices, all-optical devices, and reconfigurable devices. The mechanism of laser material interaction is also presented to utilize the direct laser writing technique.

Chapter 3 investigates the monolithic silicon modulators against cosmic radiation. After nearly 1 year of cosmic radiation in low earth orbit, device performance was compared and evaluated with the same device from a different die before radiation. The portion of devices which are able to work is investigated. The increased refractive index of silicon increased dark current in *p*-*n* junction, reduced carrier recombination lifetime, and improved 3dB bandwidth of high-speed response are observed after radiation.

Chapter 4 focuses on the small signal analysis of graphene silicon junctions for optoelectronic applications, and also numerically proposes a device architecture of direct contact graphene silicon modulators. For direct contacted graphene silicon heterogeneous junction, the voltage-dependent variation of multi-junction in the hybrid Graphene-Si *p*-*i*-*n* junction is investigated by fitting the small-signal model to the broadband RF response. The results are compared with the simulated built-in electric field distribution to analyze the junction variation and potential RC constant. It shows that the forward bias through the Si *p*-*i*-*n* junction substrate can alter the G doping levels and vertical built-in electric field on the G-Si interface. Additionally, the fitting results show a very small RC constant for the potential high bandwidth of the hybrid device’s photoresponse.

Based on the configuration of the directly contacted G-Si hybrid structure, the device architecture of G-Si modulators is numerically investigated. This device configuration enables the modulation of graphene’s carrier density by the silicon layer. Also, the out-of-plane built-in electric field enables the reduced RC constant and ultrafast carrier transportation in G between G-Si interface for high efficient and high-speed operation. By optimizing doping profiles in Si and graphene contact region, photonic crystal (PhC) waveguide-based Mach-Zehnder modulator (MZM) numerically shows a very low $V_{\pi}{\cdot}L$ and fast high-speed response for efficient and high-speed modulator applications.

Chapter 5 investigates the photorefractive response of one type of low-dimensional materials: Tellurium (Te). Tellurium was predicted to have large optical nonlinearities (such as second-order susceptibility), but there are very few works to experimentally show other nonlinear responses for thin film. The Tellurium flake is integrated into a silicon ring resonator with low loss and high-quality factors to probe the nonlinearity. A significant photorefractive effect was discovered. As the optical input signal is increasing, the resonance of Te integrated silicon ring resonator has a blue shift, indicating the decreased effective index. Raman spectrum showed that laser irradiated Te samples have partial oxidization to TeO_2 which has a smaller refractive index, leading to resonance blue shift. This material may be used for wavelength trimming of fabrication-induced resonance randomness in photonic circuits.

Chapter 6 demonstrated a laser writing platform for micro-device patterning and material processing. By using a nanosecond laser with controllable dosages, it is able to achieve the low-cost, mask-free micrometer-scale device patterning and enables the phase change on some chalcogenide material ($Ge_2Sb_2Te_5$). By using the phase change nature of chalcogenide materials such as $Ge_2Sb_2Te_5$, tunable devices are demonstrated.

Chapter 7 summarizes this dissertation and provides some thoughts for future research.

The related journal publications are listed (* contributed equally):

1. **D. Mao**, T. Kananen, T. Li, A. Soman, J. Sinsky, N. Petrone, J. Hone, P. Dong, T. Gu, "Bandwidth limitation of directly contacted graphene–silicon optoelectronics," *ACS Applied Electronic Materials*, 1, 2, 172–178 (2019). (**Chapter 4**)

2. **D. Mao**, M. Chen, X. Ma, A. Soman, H. Xing, T. Kananen, N. Augenbraun, C. Cheng, M. Doty, T. Gu, "Sub-bandgap pulsed laser patterning of planar chalcogenide microphotonics," *Optical Materials Express*, 10, 9, 2126-2134 (2020). (**Chapter 6**)

3. **D. Mao***, C. Cheng*, F. Wang, Y. Xiao, T. Li, L. Chang, A. Soman, T. Kananen, X. Zhang, M. Krainak, P. Dong, T. Gu, " Device Architectures for Low Voltage and Ultrafast Graphene Integrated Phase Modulators," *IEEE Journal of Selected Topics in Quantum Electronics*, 27, 2, 1-9 (2020). (**Chapter 4**)

4. **D. Mao**, Y. Wang, H. Lee, L. Chang, F. Wang, D. Wu, Y. Xiao, B. Sun, and T. Gu, " Structural transition induced dispersive nonlinearities in Tellurene with low power in-waveguide excitations," To be submitted. (**Chapter 5**)

5. **D. Mao***, L. Chang*, H. Lee, A. W. Yu, M. A. Krainak, P. Dong, T. Gu, " Cosmic radiation hardness of silicon photonic modulators," In preparation. (**Chapter 3**)

6. Y. Xiao, F. Wang, **D. Mao**, T. Kananen, T. Li, H. Lee, Z. Wang T. Gu, " Scalable photonic crystal waveguides with 2 dB component loss," *Photonic Technology Letters*, 34, 637-640 (2022). (**Chapter 5**)

The related conference publications are listed:

1. **D. Mao**, T. Kananen, J. Sinsky, N. Petrone, J. Hone, P. Dong, T. Gu, "Small-signal model for heterogeneous integrated graphene-silicon photonics," *Conference on Lasers and Electro-Optics (CLEO)*, SM2B.4, (*2018*). (**Chapter 4**)

2. **D. Mao**, M. Chen, N. Augenbraun, A. Soman, X. Ma, T. Kananen, M. Doty, and T. Gu, "Micromachining of chalcogenide waveguides by picosecond laser," *Conference on Lasers and Electro-Optics (CLEO)*, SF3O.5, (2019). (**Chapter 6**)

3. **D. Mao**, L. Chang, H. Lee, T. Li, Z. Wang, P. Dong, A. W. Yu, M. A. Krainak, and T. Gu "Cosmic radiation effect on silicon photonic Mach-Zehnder Modulator," *Conference on Lasers and Electro-Optics (CLEO)*, SF1C.5, (2022). (**Chapter 3**)

4. **D. Mao**, L. Chang, T. Li, H. Lee, T. Gu, A.W. Yu, M.A. Krainak, S. Altunc, P. Dong, "Performance evaluation of silicon Mach-Zehnder Modulator after cosmic radiation to enable Small Satellite Laser Communication," *Small Satellite Conference*, SSC22-XII-05, (2022). (**Chapter 3**)

5. Y. Xiao, **D. Mao**, Y. Wang, T. Gu, "Photo-refractive Switching of Micro-ring Resonators via few-layer Tellurium," *Conference on Lasers and Electro-Optics (CLEO)*, SF2O.2, (2022). (**Chapter 5**)

REFERENCES

[1] Cisco Annual Internet Report (2018–2023) White Paper. Available online: https://www.cisco.com/c/en/us/solutions/collateral/executive-perspectives/annual-internet-report/white-paper-c11-741490.html

[2] W. Shi, et al, Scaling capacity of fiber-optic transmission systems via silicon photonics. Nanophotonics, 9(16), 4629–4663, 2020.

[3] D. Marpaung, et al, “Integrated microwave photonics,” Nature Photonics 13, 80–90, 2019

[4] E. A. Park, et al, "NASA's Next Generation ⩾100 Gbps Optical Communications Relay," IEEE Aerospace Conference, 1-9, 2019

[5] G. T. Reed, et al, “Silicon optical modulators,” Nature Photonics, 4, 518–526, 2010.

[6] R. Soref, et al, Electrooptical effects in silicon. IEEE J. Quant. Electron. 23, 123–129, 1987.

[7] R. Ding, et al, Design and characterization of a 30-GHz bandwidth low-power silicon traveling-wave modulator. Optics Communications, 321, 124–133, 2014

[8] H. Yu, et al, Performance tradeoff between lateral and interdigitated doping patterns for high-speed carrier-depletion based silicon modulators. Optics Express, 20, 12, 12926-12938, 2012

[9] D. Petousi, Analysis of Optical and Electrical Tradeoffs of Traveling-Wave Depletion-Type Si Mach–Zehnder Modulators for High-Speed Operation, IEEE Journal of Selected Topics in Quantum Electronics, 21, 4, 199-206, 2015

[10] J. Sun, et al, A 128 Gb/s PAM4 Silicon Microring Modulator With Integrated Thermo-Optic Resonance Tuning, Journal of Lightwave Technology, 37, 1, 110-115, 2019

[11] F. Xia, et al, Two-dimensional material nanophotonics. Nature Photonics, 8, 899–907, 2014

[12] F. Xia, et al, Ultrafast graphene photodetector, Nature Nanotechnology, 4, 839–843, 2009

[13] M. Liu, et al, A graphene-based broadband optical modulator, Nature, 474 (7349), 2011

[14] C. Phare, Y. Daniel Lee, J. Cardenas, and M. Lipson “Graphene electrooptic modulator with 30 GHz bandwidth,” Nature Photon., vol. 9, pp. 511–514, 2015.

[15] V. Sorianello et al., “Graphene–Silicon phase modulators with gigahertz bandwidth,” Nature Photon., vol. 12, pp. 40–44, 2018

[16] H. Shu et al., “Significantly high modulation efficiency of compact graphene modulator based on silicon waveguide”, Sci. Rep., vol. 8, no. 991, pp. 1–8, 2018

[17] T. Li, et al, Spatially controlled electrostatic doping in graphene *p-i-n* junction for hybrid silicon photodiode, npj 2D Materials and Applications, 2, 36, 2018

[18] C. Ríos, M. Stegmaier, P. Hosseini, D. Wang, T. Scherer, C.D. Wright, H. Bhaskaran, W. Pernice, Integrated all-photonic non-volatile multi-level memory. Nature photonics 9, 11, 725-732, 2015

[19] C. Castellan, et al, Tuning the strain-induced resonance shift in silicon racetrack resonators by their orientation. Optics express 26(4), 4204-4218, 2018

[20] Y. Xie, et al, Thermally-Reconfigurable Silicon Photonic Devices and Circuits, IEEE Journal of Selected Topics in Quantum Electronics, 26, 5, 1-20, 3600220, 2020

[21] Q. Xu, S. Manipatruni, B. Schmidt, J. Shakya, M. Lipson, "12.5 Gbit/s carrier-injection-based silicon micro-ring silicon modulators." Optics Express 15(2) 430-436, 2007

[22] X. Gan, et al, Giant and Anisotropic Nonlinear Optical Responses of 1D van der Waals Material Tellurium, Adv. Optical Mater., 8, 2001273, 2020

[23] S. Deckoff-Jones, et al, Tellurene: A Multifunctional Material for Mid-Infrared Optoelectronics, ACS Photonics, 6, 1632−1638, 2019

[24] P. Günter, et al, Photorefractive materials and their applications 1, Basic effects, Springer-Verlag, 2006.

Chapter 2

RESEARCH FUNDAMENTALS

2.1 Some components in silicon photonics

There are many active and passive components of different functionalities in the silicon photonic platform. Passive components (such as couplers, waveguides, and converters) are used for optical signals inputs/outputs, routing, filtering, mixing, and polarization control [1]. Active components (such as lasers, modulators, and photodetectors) are used for generating, modulating, and receiving optical signals. Modulators and photodetectors are available through the CMOS-compatible doping process and Ge-on-Si epitaxy [1]. These passive and active functionalities are implemented monolithically by multiple process steps on SOI wafers, usually, including multi-level (partial and full) deep UV photolithography, etch of silicon thin films, ion implantation for multi-level *p*-type and *n*-type doping, germanium deposition on silicon, etching, and implantation for photodetectors, multilevel metals, oxide deposition, and deep trench for edge coupling [1]. In this chapter, some commonly used components related to the thesis contents will be introduced, such as Mach-Zehnder Interferometer (MZI), Micro-ring resonator (MRR), and silicon modulator.

2.1.1 Mach-Zehnder Interferometer

Mach-Zehnder interferometers (MZI) are widely used in photonic integrated circuits acting as phase shifters, switches, filters, and modulators. An MZI is formed by splitting the optical signal from a common source, guiding light in two paths that generate phase shifts, and then recombining the light (Figure 2.1).

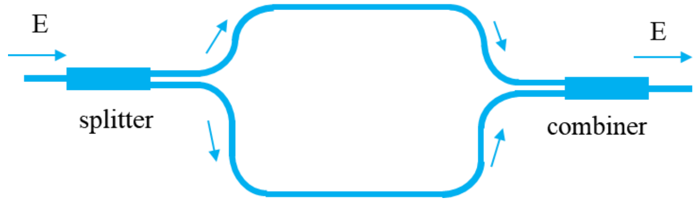

Figure 2.1 Schematics of a Mach-Zehnder interferometer. It consists of a power splitter, two arms with a length difference, and a power combiner.

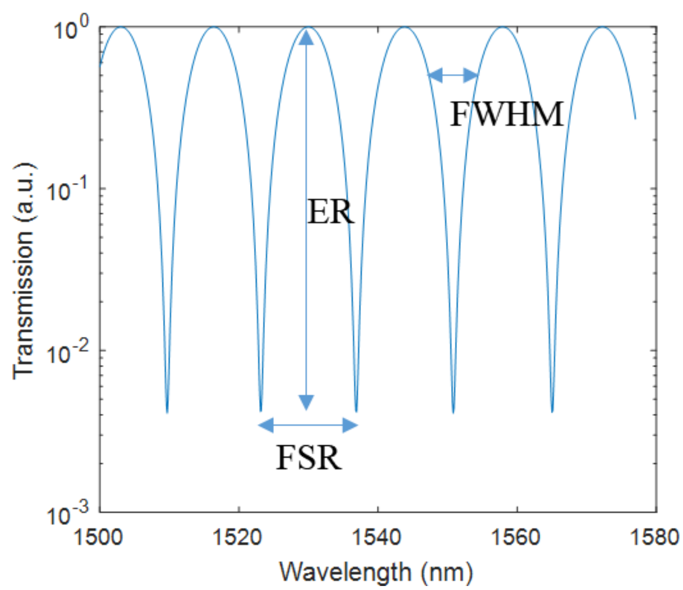

Figure 2.2 Normalized Transmission spectrum of a Mach-Zehnder interferometer.

The normalized transmission of an MZI is shown in Figure 2.2. Some parameters are introduced below:

Free Spectral Range (**FSR**) is the spacing in optical frequency or wavelength between two successive reflected or transmitted optical intensity maxima or minima of an interferometer. It is determined by:

$$FSR = \frac{\lambda^2}{n_g L}, \tag{2.1}$$

where L is the effective length, n_g is the group index.

$$n_g = n - \lambda_0 \frac{dn}{d\lambda_0}. \tag{2.2}$$

Extinction Ratio (**ER**) is the ratio of the peak transmission power to the minimum transmission power, and usually is reported in dB:

$$ER[dB] = 10log_{10}\left(\frac{T_{max}}{T_{min}}\right). \tag{2.3}$$

Full width at half maximum (**FWHM**) is defined as the width of the wavelength range where the signal power drops to 3 dB (half of the maximum value).

2.1.2 Micro-Ring Resonator

Micro-ring resonators (MRR) are one important building block in PICs for various applications, such as switches, filters, sensors, modulators, etc. The schematic of an all-pass micro-ring resonator is shown in Figure 2.3. The two coupling parameters are defined as the self-coupling coefficient t and the cross-coupling coefficient κ. In a real scenario, the micro-ring resonator has internal loss due to waveguide propagation loss and bending loss, which are defined as intrinsic losses (a).

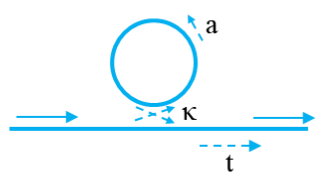

Figure 2.3 The schematic of an all-pass micro-ring resonator and some important parameters.

For a symmetric and reciprocal matrix where the coupling is lossless, the following equation is satisfied:

$$t^2 + \kappa^2 = 1\,. \tag{2.4}$$

Another important parameter is the quality (Q) factor. It is generally defined as the ratio of energy stored to the power loss per optical cycle,

$$Q = \omega \frac{Stored\ Energy}{Power\ loss}\,. \tag{2.5}$$

The higher the quality factors are, the lower the losses in the micro-ring resonator due to round-trip loss, including coupling, bending, and scattering losses. Specifically, it can be characterized by the energy decay rate:

$$Q = \frac{\omega}{\gamma}, \tag{2.5}$$

where γ is the photon energy decay rate.

Additionally, the Q-factor can be calculated using the full-width half maximum (FWHM) of the "dip":

$$Q = \frac{\lambda_{res}}{FWHM}\,. \tag{2.6}$$

The quality factor is related to the intrinsic quality factor (Q_{in}) and coupling quality factor (Q_c):

$$\frac{1}{Q} = \frac{1}{Q_{in}} + \frac{1}{Q_c}, \tag{2.7}$$

where Q_c is dependent on the external coupling, Q_{in} is inversely proportional to the intrinsic loss rate (γ_{in}). The intrinsic Q-factor (Q_{in}) of a micro-resonator is determined by:

$$\frac{1}{Q_{in}} = \frac{1}{Q_r} + \frac{1}{Q_s} + \frac{1}{Q_m}, \tag{2.8}$$

where Q_r, Q_s, and Q_m account for the Q-factor limit due to radiation loss, scattering loss, and material loss, respectively.

A matrix equation can be used to describe the basic properties of an all-pass micro-ring resonator. The two coupling parameters are the through coefficient t and cross-coupling coefficient κ. E_{i1} is the field incident into the input waveguide, and the output field is E_{1t}. The field coupled to the ring waveguide is E_{1i}, and the field coupled back towards the straight waveguide is E_{i2}. The transfer matrix can be written as follows:

$$\begin{bmatrix} E_{1t} \\ E_{1i} \end{bmatrix} = \begin{bmatrix} t & -j\kappa \\ -j\kappa & t \end{bmatrix} \begin{bmatrix} E_{i1} \\ E_{i2} \end{bmatrix}. \tag{2.9}$$

The field propagating inside the ring can be written as:

$$E_{i2} = a * e^{-j\theta} E_{t2}, \tag{2.10}$$

where α is the round-trip loss factor, θ is the round-trip phase shift.

The transmission equation is derived as:

$$\frac{P_{1t}}{P_{1i}} = \frac{|E_{1t}|^2}{|E_{1i}|^2} = \frac{\left|t - a * e^{-j\theta}\right|^2}{|1 - a * t * e^{-j\theta}|^2}. \tag{2.11}$$

Based on the two types of losses, the following three coupling mechanisms are categorized:

Under coupled (a>κ): The light coupled to the micro-ring is smaller than the light transmitted to the through port. This condition can be achieved by increasing the gap size between the bus waveguide and the micro-ring.

Critically coupled (a=κ): it is obvious that the transmitted power in this case is zero due to destructive coupling, as the light coming out of the micro-ring is 180-degree phase-shifted from the incoming light. Here the light is completely coupled to the micro-ring, and no light is transmitted to the through port.

Over coupled (a<κ): Here the light coupled to the micro-ring is greater than the light transmitted to the through port. This condition can be achieved by reducing the gap size between the bus waveguide and the micro-ring.

2.1.3 Modulators

Modulators are one important building block in Photonic integrated circuits. It modulates the optical carriers to higher frequencies for various advanced modulation formats for efficient and high-capacity transmission in fiber systems [1]. Modulation is achieved by changing either the real or the imaginary part of the refractive index by applying an external excitation to the optical field. As some contents in this thesis focus on silicon modulators, the modulation mechanism in silicon will be mainly discussed here.

Modulation in silicon is determined by the plasma dispersion effect [4][5]. The changes in carrier densities (electrons and holes) will lead to changes in the refractive index (both real and imaginary parts). Their relationship is shown below: [5]

$$\Delta n(1550nm) = -[8.8 \times 10^{-22} \times \Delta n_e + 8.5 \times 10^{-18} \times (\Delta n_h)^{0.8}], \qquad (2.12)$$

$$\Delta\alpha(1550nm) = 8.5 \times 10^{-18} \times \Delta n_e + 6.0 \times 10^{-18} \times \Delta n_h, \qquad (2.13)$$

where Δn_e and Δn_h are the changes in the electron and hole carrier concentrations, respectively.

There are three types of modulation schemes: carrier accumulation (in a MOS capacitor structure), carrier injection (in a forward-biased *p-i-n* junction structure), and carrier depletion (in a reverse-biased *p-n* junction structure) (Figure 2.4) [2][6]. Carrier accumulation in MOS capacitors can achieve high modulation efficiency, but the high-speed response is limited by the high capacitances from a thin oxide layer. Carrier injection can provide the most efficient modulation, but it is hard to achieve high speed because it suffers from high junction capacitance and slow free-carrier recombination. Finally, carrier depletion has a low modulation efficiency but can achieve high-speed performance by optimizing doping profiles to reduce the junction capacitance.

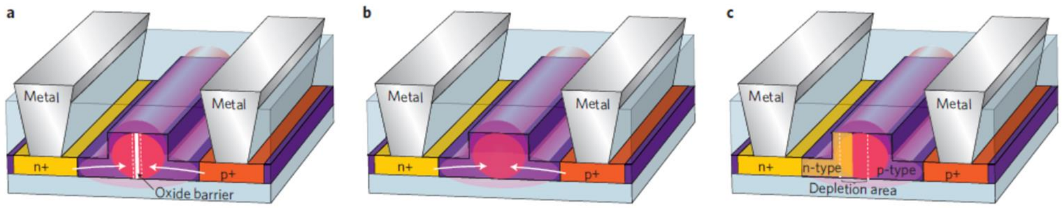

Figure 2.4 Silicon modulators of different types: (a) Carrier accumulation, (b) carrier injection, (c) carrier depletion schemes. [2]

The complex refractive index n can be expressed as:

$$\overline{n} = n + j * k, \tag{2.14}$$

where n is the real part, and k is the extinction coefficient. The absorption coefficient α from the extinction coefficient is given by:

$$\alpha = \frac{4\pi k}{\lambda_0}. \tag{2.15}$$

Some important parameters of modulators will be introduced as follows:

$V_\pi L$. Under the condition that the device achieves a π phase shift, the product of applied voltage and the length to achieve the π phase shift is defined as $V_\pi L$. The smaller the $V_\pi L$ is, the higher modulation efficiency the modulator has,

$$\Delta\varphi = \frac{\Delta n_{eff}(V_\pi)2\pi L}{\lambda_0} = \pi. \tag{2.16}$$

Insertion loss (*IL*). The insertion loss is the ratio of the peak normalized transmission and the ideal transmission. The quantity is reported in dB.

$$IL = -10log_{10}(T_{max}), \tag{2.17}$$

$$IL[dB] = P_{in,dBm} - P_{max,dBm.} \tag{2.18}$$

Modulation bandwidth: The cut-off frequency corresponds to the modulation sideband power which is reduced to 3 dB from its maximum value.

When applying an RF signal to the optical carrier, the optical sideband signal is generated (Figure 2.5). The optical sideband power is one important figure of merit for high-frequency operation. The relative power of the sidebands is directly related to the modulation frequency. The envelope of sideband intensities is the high-speed modulation response.

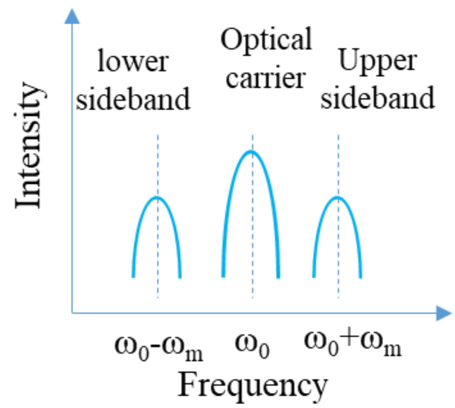

Figure 2.5 Modulation scheme of high-frequency RF modulated signal (ω_m) applied on an optical carrier (ω_0).

The bias condition for the MZM should be carefully selected based on the application. For analog high-speed measurement, a quadrature biasing point should be chosen for the most linear operation so that the largest change in the output signal is achieved for a small input signal. This operating point can be controlled by applying a DC bias voltage, which also locks the modulator at the specific stable operating wavelength and prohibits transmission spectrum drifting during operation. The quadrature biasing point is the voltage required to achieve an odd multiple of $\pi/2$ phase difference.

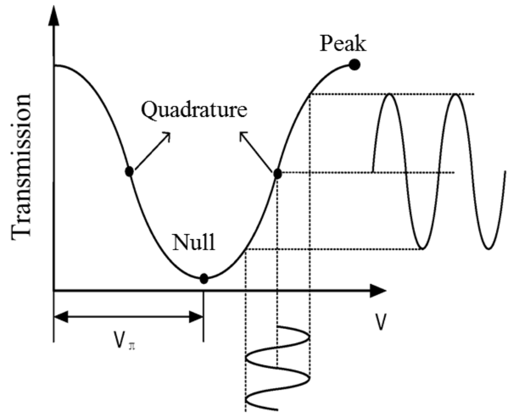

Figure 2.6 Transmission of the Mach-Zehnder modulator (MZM) and location of three different bias conditions.

The 3 dB bandwidth of silicon Mach-Zehnder modulators is dependent on the total time constant, which is limited by RC constant and carrier lifetime (recombination lifetime or transit time-dependent) : [4][6]-[8]

$$f_{3dB} = \frac{0.55}{\tau}, \tag{2.19}$$

$$\frac{1}{\tau} = \frac{1}{\tau_{RC}} + \frac{1}{\tau_{rec}} + \frac{1}{\tau_{tr}}. \tag{2.20}$$

2.2 Low Dimensional materials

With the rapid development of silicon photonics technology, the performance bottleneck of each device component gradually appeared. For example, silicon modulators' modulation efficiency is limited by the nonlinear carrier dispersion effect in silicon, also the high-speed performance is limited by the limited hole and electron mobility. For carrier injection-type modulators, it will encounter extra loss due to the carrier dispersion effect when applying a forward bias. Silicon is not an ideal candidate for photodetectors due to limited absorption. Monolithic silicon is not suitable for lasers as its indirect bandgap. To integrate other materials with different electronic and optical properties on silicon is one promising option.

Since monolayer graphene was first discovered in 2004, low-dimensional materials have been widely studied and brought many opportunities due to their diverse electronic and optic properties. They can range from insulators (e.g., hexagonal boron nitride (h-BN)), and semiconductors with various bandgaps (black phosphorous, transition metal dichalcogenides (TMDCs), e.g., MoS_2), to semi-metal graphene [9]. They show many complementary and unique characteristics including broadband absorption, ultrafast carrier mobility, strong nonlinear effects, and compatibility for hybrid integration [10]. They could provide a wide range of options for optoelectronic devices and fulfill the request of emerging photonic applications.

One effective way to interact with light is to integrate the low dimensional materials with photonic structures. Based on the CMOS platform of silicon photonics, the hybrid integration of low dimensional materials is promising for future on-chip optoelectronic devices to achieve higher device densities, lower power consumption, and faster response.

2.2.1 Graphene

Graphene is a two-dimensional (2D) material made of carbon atoms arranged in a hexagonal shape (Figure 2.7(a)). It is a semi-metal with zero bandgaps (Figure 2.7(b)). It has attracted a lot of research attention as it could interact with light from microwave to ultraviolet wavelengths, making it a potential candidate for light detection, modulation, and manipulation over a wide spectral range [9]. Due to its high carrier mobility (up to 10^5 cm^2 $V^{-1}s^{-1}$), this also makes it a promising candidate for high-speed optoelectronic devices [11].

(a) (b)

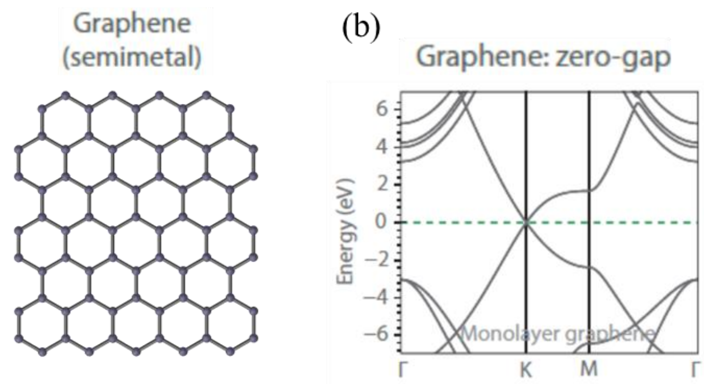

Figure 2.7 (a) Top view of Graphene atomic structure. (b) Band diagram of monolayer graphene [9].

2.2.2 Tellurium

As graphene lacks a bandgap, it's not ideal for field-effect transistors (FETs) made of graphene to effectively switch on/off. Materials with different bandgaps are desired to study a wide range of applications. For example, Transition metal dichalcogenides (TMDCs) are a type of material with sizable bandgaps around 1–2 eV and are promising for new FET and optoelectronic devices [19] [9].

Except for TMDCs, another promising low bandgap material Tellurium (Te) will be introduced and studied in one Chapter in this thesis. Tellurium is one Group VI element with an unintentionally p-type doped narrow bandgap (E_g almost direct of 0.35 eV) (Figure 2.8) [20]. The bandgap is layer dependent to increase up to 1 eV when the thickness reduces to monolayer (Tellurene). Researchers found out that it has higher hole mobility (up to 700 $cm^2\ V^{-1}s^{-1}$) than black phosphorus and is very stable at room temperature for a long time [21]. Its unique chiral chain structure makes it promising for next-generation electronics, optoelectronics, strong optical nonlinearity, chirality, and piezoelectric applications.

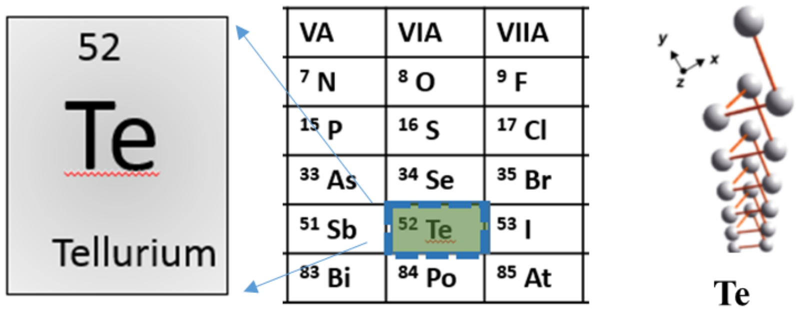

Figure 2.8 Group VI element Tellurium and its structure.

2.2.2.1 Transfer of Te flakes

As one Chapter in this thesis will focus on studying Te nonlinearity by using a silicon photonic platform, the transfer process is presented here.

After the hydrothermal synthesis [21], Te flakes can be transferred in the solution (wet transfer) (Figure 2.9). Take 5 mL raw solutions into the tube and use the centrifuge to precipitate the solution at 3000 r.p.m for 10 mins. Then remove the upper layer of liquids and use DI water to rinse a few times to remove any ions remaining in the final product. The Langmuir–Blodgett (LB) process can be followed to transfer the flakes on the chip. Use a plastic transfer pipette to absorb a few drops of solutions and release them onto the surface of the water in a bowl. The Te flakes will be floating on the surface of the water. And use the chip to scoop up the flakes.

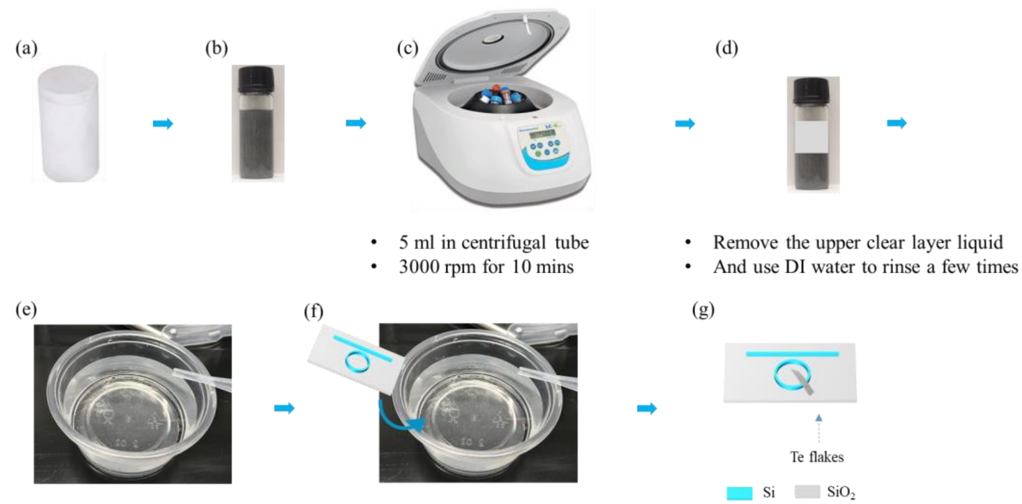

Figure 2.9 Tellurium wet transfer schematics.

The wet transfer method sometimes is not ideal because there would be a random distribution of multiple Te flakes on one device to cause large loss due to material absorption (Figure 2.10). Te flakes on the waveguide would induce very significant loss.

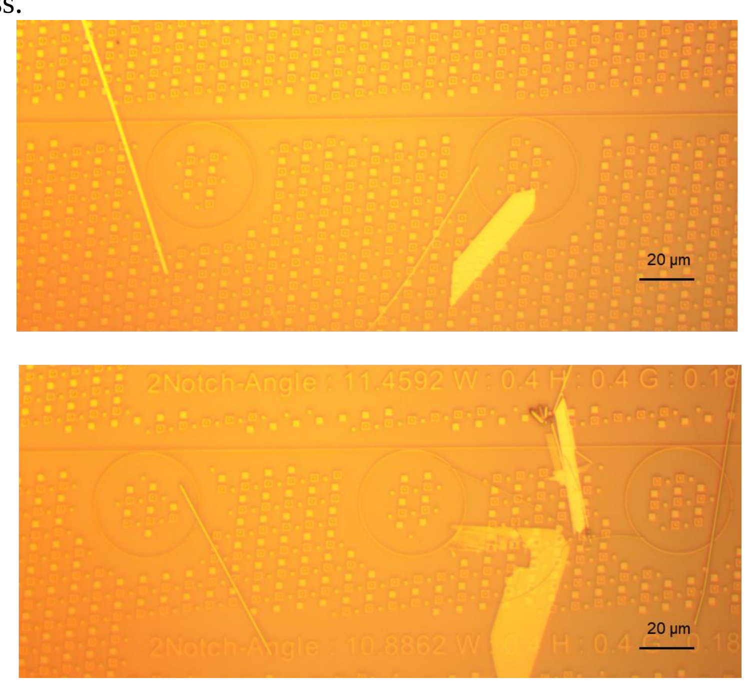

Figure 2.10 Examples of multiple Te flakes on one ring resonator after wet transfer.

To have the determined transfer of one desired Te flake on the desired position of the device, the dry transfer method is proposed. Below is the process for the dry transfer method:

(a) Take one droplet from tellurium raw solutions to drop on one synthesized transparent PDMS (Figure 2.11(a,b)).

(b) After drying the droplet at room temperature for a few minutes (Figure 2.11(c)), face down the PDMS side with tellurium flakes and fix the PDMS on the bottom side of a glass slide through clips (Figure 2.11(d)).

(c) The clips are fixed on one xyz motion stage which can control the direction and position of the Te samples. The PDMS with Te flake is illuminated and reflected to the camera to have real-time imaging. The open-window silicon photonic sample (face up) is put on one xyz stage with a heating function. Move the xyz stage that holds the silicon photonic chip under the microscope to align the desired silicon device in the center of microscope imaging. Choose one desired Te flake from the microscope imaging, then move the PDMS/Te sample through the xyz stage to closely approach and target one desired Te flake on the desired silicon device. Low down the xyz stage which holds the Te sample until its contact with the silicon device (Figure 2.11(e)).

(d) Launch the heating stage at about 70℃ and heat for about 10 mins to release the Te flake onto the silicon device. After Te falls, raise the xyz stage with the PDMS and take the hybrid Te silicon sample for usage (Figure 2.11(f)).

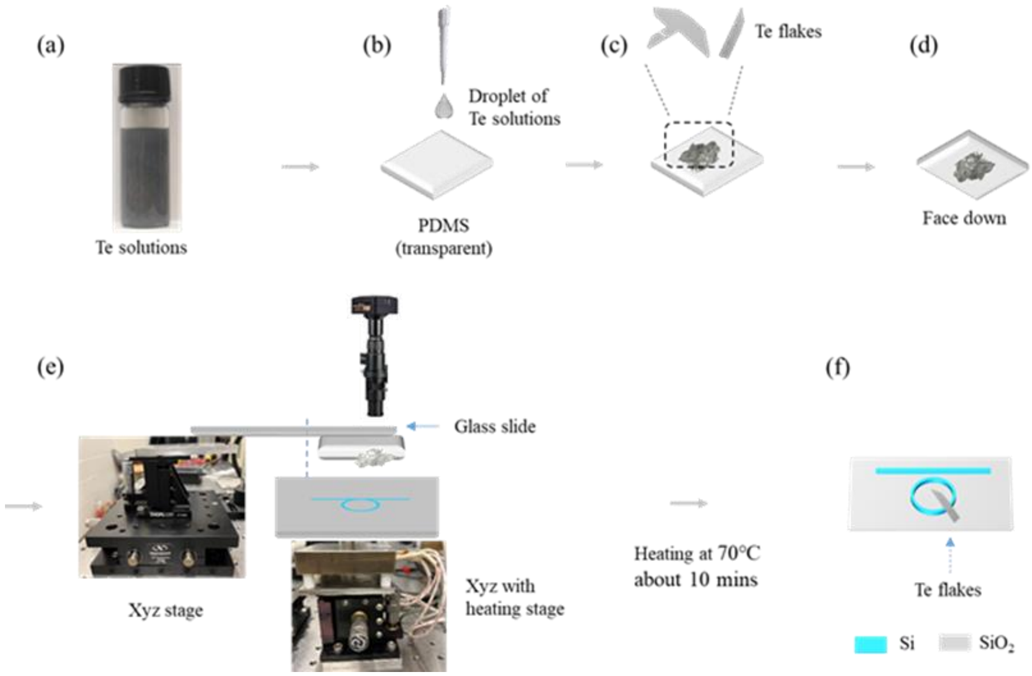

Figure 2.11 Dry transfer method for Tellurium thin film on silicon devices.

2.2.3 Phase change materials

Phase change materials (PCMs) are one kind of material that can be rapidly and reversibly switched between amorphous and crystalline states (Figure 2.12) [22][23]. The optical and electronic properties of the amorphous and crystalline states differ tremendously [25][24]. The complex refractive index of amorphous and crystalline states $Ge_2Sb_2Te_5$ is shown as an example in Figure 2.1. Under certain stimuli, if the phase change only occurs when the stimulus is turned on, then it is called volatile (e.g., VO_2). Alternatively, if the material can keep the switched state even after the external stimulus is turned off, then it's called non-volatile (e.g., $Ge_2Sb_2Te_5$) [23]. Such as $Ge_2Sb_2Te_5$, the two phases have large optical index contrast (Figure 2.13) and have a wide range of applications in photonics, including optoelectronic storage and display systems, optical switches, reconfigurable devices, photonic in-memory computing, etc. [23][24][27][28][29]

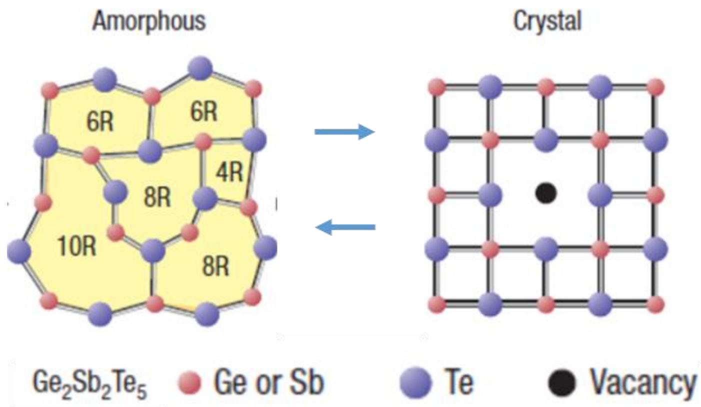

Figure 2.12 Schematic of structural transformation in the phase change between amorphous and crystalline states for PCM $Ge_2Sb_2Te_5$. [22]

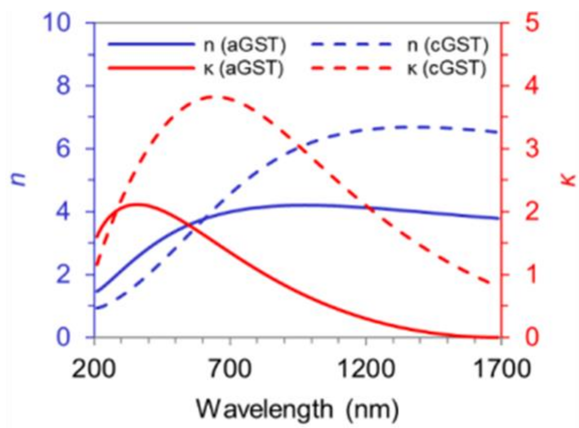

Figure 2.13 Complex refractive index of a-GST and c-GST as a function of wavelength for PCM $Ge_2Sb_2Te_5$. [25]

2.3 Direct Laser writing technique

Direct laser writing (DLW) with various pulse durations and intensities can interact with materials to provide flexible and low-cost ways for versatile mask-free patterning and material processing (Figure 2.14) [30].

Upon pulse irradiation, the material experiences several regimes: carrier excitation, thermalization, carrier removal, and thermal and structural effects (Figure 2.15). The fs- and ps- pulses with high peak pulse energies can deliver energy to the material on a timescale shorter than the electron–phonon coupling relaxation time to cause nonlinear and multiphoton absorption. During multiphoton absorption, bonds between electrons in the irradiated sample are directly broken to cause the non-thermal process. The ns- and ms- pulses interacting with materials will have the photo-thermal process to ablation and melting effects. [31]

By controlling the pulsed laser intensities and pulsed repetition rate, it is able to have the photo-thermal effect and less thermal effect which leads to ablation-based patterns and material phase change, respectively.

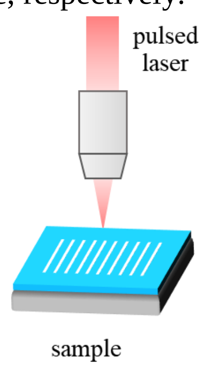

Figure 2.14 Schematics of direct laser writing on a sample to create patterns.

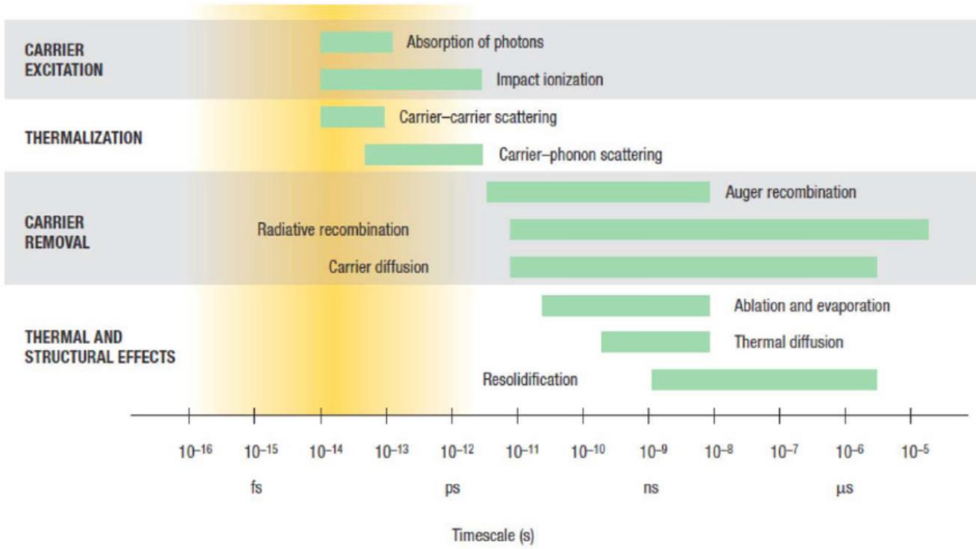

Figure 2.15 Timescales of four electron and lattice excitation regimes following ultrafast laser semiconductor interaction. For each process, the green bars represent a range Figure of time durations for carrier densities varying from 10^{17} to 10^{22} cm^{-3}.[31]

REFERENCES

[1] W. Shi, et al, Scaling capacity of fiber-optic transmission systems via silicon photonics. Nanophotonics, 9(16), 4629–4663, 2020.

[2] D. Marpaung, et al, "Integrated microwave photonics," Nature Photonics 13, 80–90, 2019

[3] C. Sun, et al, Single-chip microprocessor that communicates directly using light. Nanophotonics Nature, 528, 534–538, 2015.

[4] G. T. Reed, et al, "Silicon optical modulators," Nature Photonics, 4, 518–526, 2010.

[5] Soref, et al, B. Electrooptical effects in silicon. IEEE J. Quant. Electron. 23, 123–129, 1987.

[6] P. Dong, L. Chen, and Y. Chen, "High-speed low-voltage single-drive push-pull silicon Mach-Zehnder modulators," Optics Express, 20(6), 6163-6169, 2012

[7] N. Flöry, et al, Waveguide-integrated van der Waals heterostructure photodetector at telecom wavelengths with high-speed and high responsivity, Nat. Nanotechnol. 15, 118–124, 2020.

[8] S. Lischke, et al. Ultra-fast germanium photodiode with 3-dB bandwidth of 265 GHz. Nat. Photon. 15, 925–931, 2021.

[9] F. Xia, et al, Two-dimensional material nanophotonics. Nature Photonics, 8, 899–907, 2014

[10] J. Wu, et al, Two-Dimensional Materials for Integrated Photonics: Recent Advances and Future Challenges, Small Sci., 1, 2000053, 2021

[11] M. Jin, et al, Silicon-Based Graphene Electro-Optical Modulators, Photonics, 9, 82, 2022

[12] M. Liu et al, A graphene-based broadband optical modulator, Nature, 474, 64–67, 2011.

[13] M.Romagnoli, et al, Graphene based integrated photonics for next-generation datacom and telecom, Nature Rev. Mater., 3, 392–414, 2018.

[14] V. Sorianello et al, Graphene–Silicon phase modulators with gigahertz bandwidth, Nature Photon., 12, 40–44, 2018.

[15] Z. Sun, et al, Optical modulators with 2D layered materials, Nature Photon., 10, 227–238, 2016.

[16] C. Phare, et al, Graphene electrooptic modulator with 30 GHz bandwidth, Nature Photon., 9, 511–514, 2015.

[17] P. Ma, et al, Plasmonically enhanced graphene photodetector featuring 100 Gbit/s data reception, high responsivity, and compact size, ACS Photon., 6(1), 154–161, 2019.

[18] F. Xia, et al, Ultrafast graphene photodetector, Nature Nanotechnology, 4, 839–843, 2009

[19] Q. Wang, et al, Electronics and optoelectronics of two-dimensional transition metal dichalcogenides, Nature Nanotechnology, 7, 699–712, 2012

[20] G. Qiu, et al, The resurrection of tellurium as an elemental two-dimensional, npj 2D Materials and Applications, 6, 17, 2022

[21] Y. Wang, Field-effect transistors made from solution-grown two-dimensional tellurene, Nat. Electronics, 1, 228–236, 2018.

[22] M. Wuttig, et al, Phase-change materials for rewriteable data storage, Nature Materials, 6, 824–832, 2007.

[23] M. Wuttig, et al, Phase-change materials for non-volatile photonic applications, Nature Photonics, 11, 465–476, 2017.

[24] A. V. Pogrebnyakov, et al, Reconfigurable near-IR metasurface based on Ge2Sb2Te5 phase-change material, Opt. Mater. Express 8(8), 2264–2275, 2018.

[25] J. Zheng, et al, GST-on-silicon hybrid nanophotonic integrated circuits: a non-volatile quasi-continuously reprogrammable platform, Optical Materials Express, 8(6), 1551-156, 2018.

[26] J. Feldmann, et al, Parallel convolutional processing using an integrated photonic tensor core, Nature 589, 52–58, 2021.

[27] K. Dong, et al, A Lithography-Free and Field-Programmable Photonic Metacanvas, Adv. Mater. 30(5), 1703878, 2018.

[28] H Zhang, et al, Miniature multilevel optical memristive switch using phase change material, ACS Photonics 6 (9), 2205-2212, 2019.

[29] C Ríos, et al, Integrated all-photonic non-volatile multi-level memory, Nature photonics 9 (11), 725-732, 2015.

[30] Sergey V. Makarov, et al, Light-Induced Tuning and Reconfiguration of Nanophotonic Structures, Laser Photonics Rev., 11, 1700108, 2017

[31] K. Phillips, et al, Ultrafast laser processing of materials: a review, Adv. Opt. Photonics 7(4), 684–712, 2015.

[32] X. Gan, et al, Giant and Anisotropic Nonlinear Optical Responses of 1D van der Waals Material Tellurium, Adv. Optical Mater., 8, 2001273, 2020

[33] S. Deckoff-Jones, et al, Tellurene: A Multifunctional Material for Mid-Infrared Optoelectronics, ACS Photonics, 6, 1632−1638, 2019

[34] P. Günter, et al, Photorefractive materials and their applications 1, Basic effects, Springer-Verlag, 2006.

Chapter 3

PERFORMANCE EVALUATION OF SILICON PHOTONIC MACH-ZEHNDER MODULATORS AFTER COSMIC RADIATION

3.1 Background and motivation

Free space optical communications (FSOC) will be playing an important role in future space communication systems and networks. Optical communication links with high data rates and low latency between ground stations, satellites, and International Space Station (ISS) are preferred over conventional radio frequency (RF) systems [1]. Silicon photonics (SiPh) technology is rapidly developing and used in optical communications for its low cost, high yield, low power consumption, and high-speed merits. Consequently, it may be widely used in space optical communication in future. However, cosmic rays in space (e.g., alpha, gamma rays) have radiation effects. The reliability and robustness of silicon photonics integrated circuits (PIC) under the real cosmic environment are unknown and challenging.

Previous in-lab studies show that radiation effects could cause ionized radiation or displacement damage to affect material properties and device performance [2]-[12]. Specifically, ionization damage could generate charges to change the free carrier densities, and create traps between the silicon and silicon dioxide interface [2]-[5][12]. Displacement damage could induce lattice defects and reduce carrier lifetime in materials [6][7]. In the real cosmic environment, the radiation effects may be complicated and are contributed by different kinds of rays (alpha, gamma) and ions together. This work's aim is not to distinguish the effect coming from one certain ray or ion but only focuses on the permanent change of silicon device's performance after real cosmic radiation that may contain all possible rays and ions. In addition, no work has studied the high-speed response of silicon devices after real cosmic radiation. This work will demonstrate the change in high-speed response after cosmic radiation.

3.2 Radiation effect on the performance of silicon Mach-Zehnder Modulators

In our work, we sent our foundry fabricated PIC chips containing silicon Mach-Zehnder Modulators (MZM) for cosmic radiation evaluation. The chip was mounted on the RAM side (forward direction) of ISS for over 10 months (about 180 million miles) of radiation exposure in low earth orbit (LEO) (Figure 3.1(a)(c)). The time-varying Galactic Cosmic Ray (GCR) Dose and South-Atlantic Anomaly (SAA) Dose were recorded by the Radiation Dosimetry on the ISS (Figure 3.1(b)) [13]. The MZM has two arms with a length difference of 42 μm (Figure 3.1(c)). The *P* and *N* regions in the waveguide have doping densities of 6×10^{17} cm^{-3} (Figure 3.1(d)). And heavily doped regions *P*++ and *N*++ have doping densities of 1×10^{20} cm^{-3} to form the ohmic contact (Figure 3.1(d)) [14][15]. The effective electrical length of *p*-*n* junction is about 5 mm. Before and after launching (referring to **pre** and **post-flight** in the text), device performance, including optical transmission spectra, the electrical response of *p*-*n* junction, EO response, and the high-speed response of MZMs for the same device on a die were tested and analyzed. The radiation effect was studied from the device aspect, especially the permanent performance change of each response for MZMs.

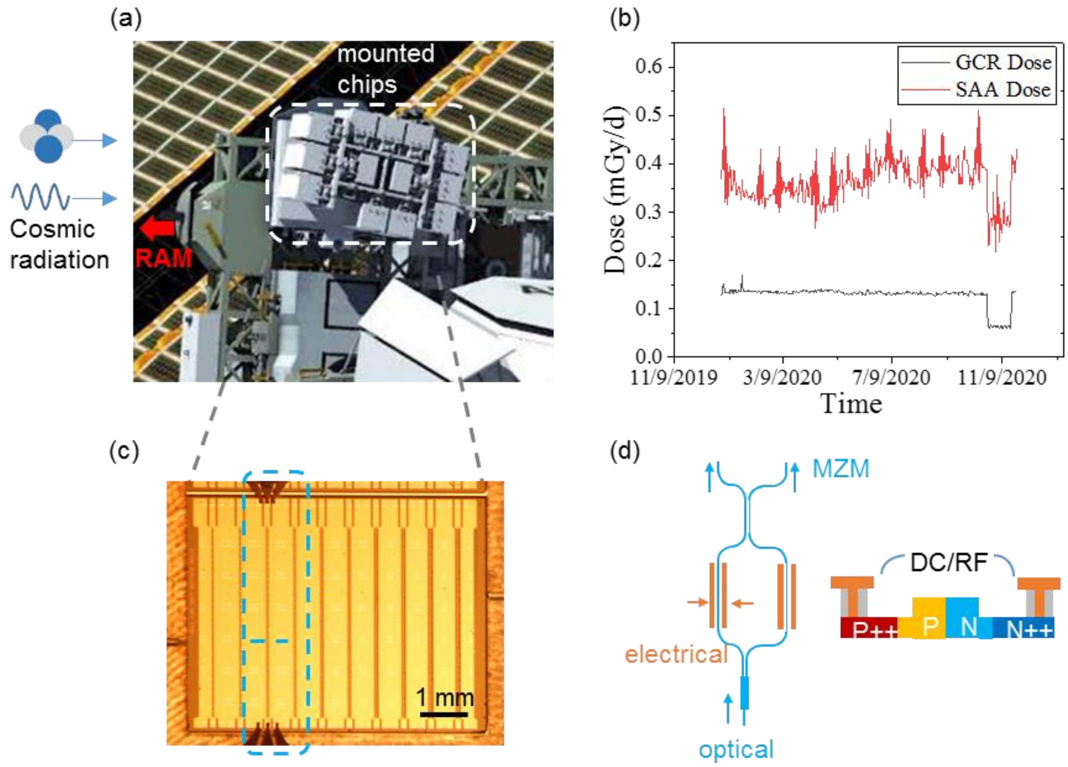

Figure 3.1 (a) Schematics of SiP chips mounted on the RAM side (forward direction) of ISS for cosmic radiation. (b) The time-varying radiation dosage diagram. (c) Optical image of one silicon MZM chip. (d) Schematics of MZM structure (top view, from the dashed frame in (c)), and electrical doping profiles of a silicon *p*-*n* junction of waveguide (the cross-section view from the dashed line in (c)).

3.2.1 Optical transmission of silicon MZMs

Optical transmission spectra were tested and compared for the same device on the same die before and after radiation. One example of MZMs with a significant change in the transmission spectra was shown in Figure 3.2(a). After flight, the transmission spectra have an Extinction Ratio (ER) reduction of about 13 dB and have a red shift. Both the change of ER and spectrum red shift are induced by the real (Δn_{eff}>0) and imaginary (Δk_{eff}>0) effective index change. Based on the equation of transmission spectra for pre flight (3.1) and post flight (3.2) samples, transmission spectra can be fitted [16]. As a result, the change of real and imaginary parts of the effective index can be extracted.

$$T_{pre} = \left|\frac{1}{1+\sigma}\left[\sigma \exp\left(j\frac{2\pi}{\lambda_0}n_{eff}(\Delta L + L)\right) + \exp\left(j\frac{2\pi}{\lambda_0}n_{eff}L\right)\right]\right|^2, \tag{3.1}$$

$$T_{post} = \left|\frac{1}{1+\sigma}\left[\sigma \exp\left(j\frac{2\pi}{\lambda_0}(n_{eff} + \Delta n_{eff} + j \times \Delta k_{eff})(\Delta L + L)\right) + \exp\left(j\frac{2\pi}{\lambda_0}(n_{eff} + \Delta n_{eff} + j \times \Delta k_{eff})L\right)\right]\right|^2, \tag{3.2}$$

where σ is the power splitting ratio, n_{eff} is the effective index, L is the length of one arm in MZM, ΔL is the length difference between the two arms of MZM, Δn_{eff} is the change of the real part of the effective index, Δk_{eff} is the change of the imaginary part of the effective index.

For the device in Figure 3.2(a), the real and imaginary parts of effective index change are on the order of 10^{-3} which are significant. Statistical results of Δn_{eff} and Δk_{eff} for 15 MZM devices on the same die are present in Figure 3.2(b). For the real part of Δn_{eff}, the average change is 0.88×10^{-3}; for the imaginary part Δk_{eff}, the average change is 0.717×10^{-3}. The error bar denotes the standard deviation relative to the average.

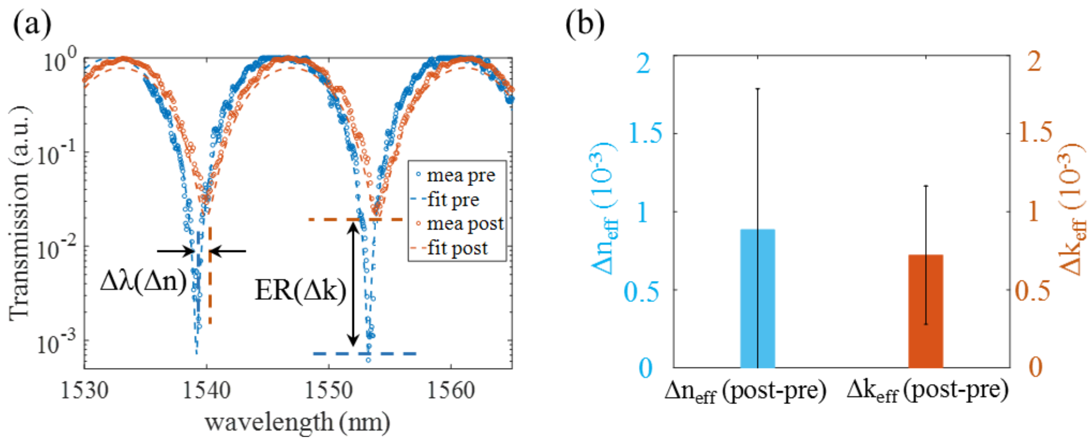

Figure 3.2 Optical transmission spectra measurement and parameter extraction. (a) Measured and fitted optical transmission for a silicon MZM before (pre) and after (post) radiation. (b) Statistics of real and imaginary effective index change extracted from 15 MZMs. Real part: $\Delta n_{eff} = n_{eff}$ *(post)*-n_{eff} *(pre)*, imaginary part: $\Delta k_{eff} = k_{eff}$ *(post)*-k_{eff} *(pre)*. The bar value is the average change in the effective index, and the error bar is the standard deviation.

3.2.2 Electrical-optical (DC) response of silicon MZMs

EO response under the reverse bias of MZM pre and post flight samples was characterized and compared in Figure 3.3(a). Under the reverse bias, the *p-n* junction will get depleted. Carrier densities around the waveguide part will decrease so that Δn_{eff} will increase and Δk_{eff} will decrease. By fitting the transmission spectra, the Δn_{eff} and the Δk_{eff} can be extracted (Figure 3.3(b)(c)). After radiation, the post flight MZM has a very trivial change in the Δn_{eff}, while has a significant change in Δk_{eff} under each bias, showing the reduced capability of carrier plasma dispersion effect in tuning Δk_{eff}.

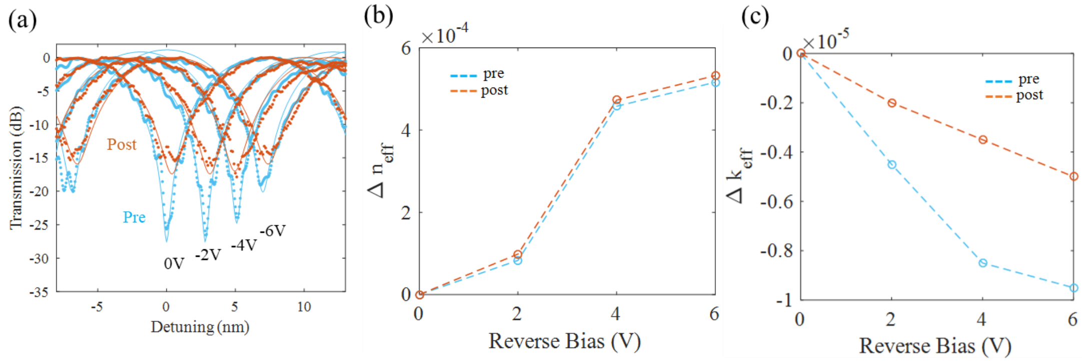

Figure 3.3 EO response under reverse bias. (a) EO response of MZMs under reverse bias (0~ -6V, 2V scanning step). (b) Real part effective index change (Δn_{eff}) under each reverse bias for pre and post flight MZMs. (c) Imaginary part effective index change (Δk_{eff}) under each reverse bias for pre and post flight MZMs.

3.2.3 Electrical response of *p-n* junction of silicon MZMs

The electrical response of *p-n* junction for pre and post flight MZM samples were also characterized. Current-voltage (I-V) and capacitance-voltage (C-V) responses were measured and compared. C-V curves (at 100 MHz) for one *p-n* junction before and after radiation were shown in Figure 3.4(a). After radiation, the capacitance increased at each reverse bias. Average capacitance per unit length (*C/L*, *L* is the electrical length of a *p-n* junction) at 0V bias was collected and averaged for 10 pre and post flight *p-n* junctions (Figure 3.4(b)). The capacitance of *p-n* junction increased by about 10% after radiation.

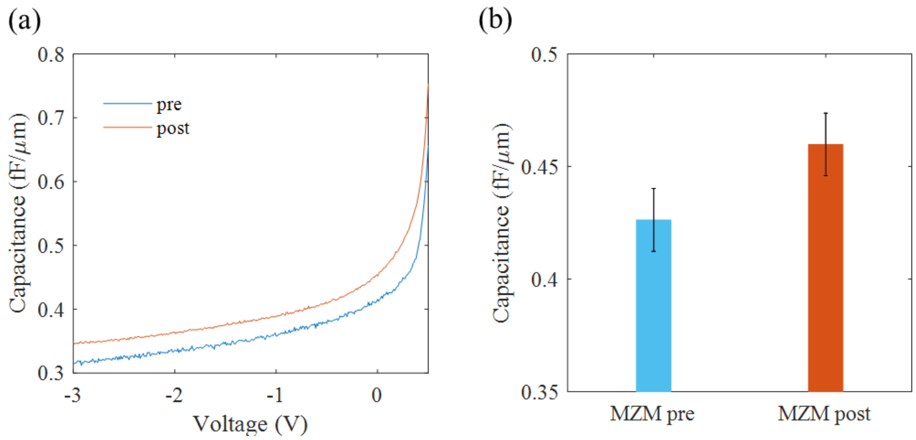

Figure 3.4 C-V test results. (a) C-V measurement of one *p-n* junction under reverse bias. (b) Average capacitance per unit length (μm) of *p-n* junctions for the pre and post flight samples (each based on 10 samples).

I-V curves for one *p-n* junction before and after radiation were shown in Figure 3.5(a). After radiation, the dark current in the reverse bias increased by nearly one order (10^{-1}). By fitting the I-V curve equation (3.3), parameters can be extracted [17].

$$I = I_0 \left[\exp\left(\frac{V - I \times R_S}{nV_T}\right) - 1\right], \tag{3.3}$$

where I_0 is the reverse saturation current, R_S is the series resistance, n is the ideality factor, and V_T is the thermal voltage ($V_T=kT/q$). k is the Boltzmann's constant (1.38×10^{-23} J/K); T is the temperature; q is absolute value of electron charge (1.602×10^{-19}C). At 300K, $V_T=kT/q=0.0259V$.

Ideality factor (n), reverse saturation current (I_0) Series resistance (R_S), and shunt resistance (R_{SH}) of 10 *p-n* junctions were extracted and averaged, respectively (Figure 3.5, Figure 3.6). After radiation, the average ideality factor increased from 1.395 to 1.43; and the average reverse saturation current got increased over two times compared with pre flight sample (Figure 3.5(d)). The change of reverse saturation current is the most significant one among those parameters.

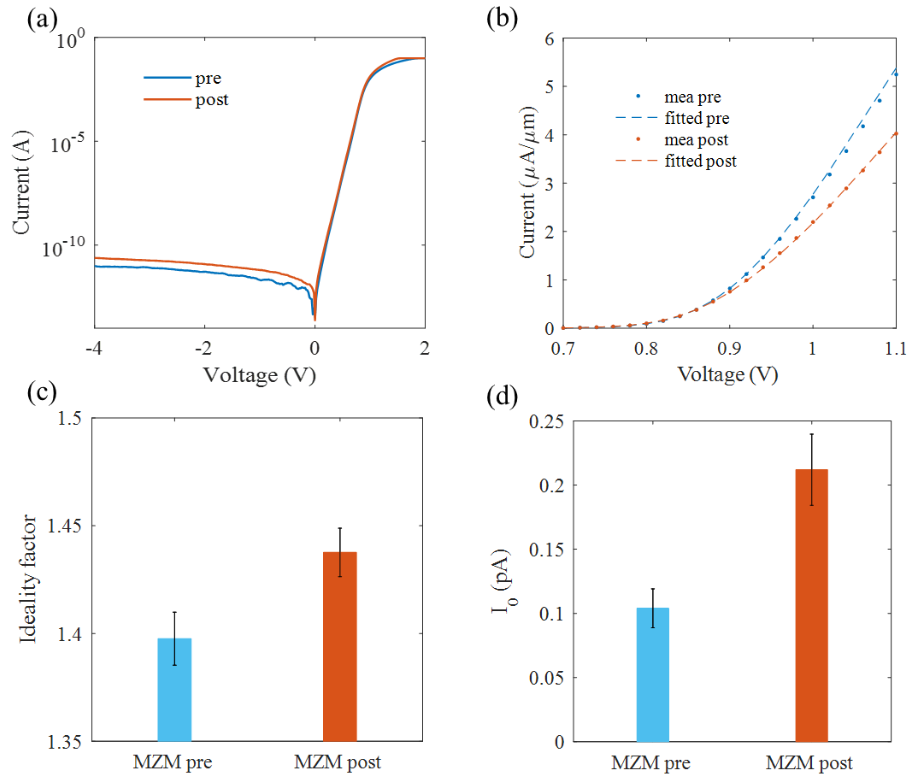

Figure 3.5 I-V tests and parameter extraction. (a) Measured I-V curves of one *p-n* junction for pre and post flight. (b) Measured and fitted I-V curves of one MZM *p-n* junction. (c) Average of extracted ideality factor n for the pre and post flight samples. (d) Average of extracted reverse saturation current I_0 for the pre and post flight samples. For n, and I_0, each is based on 10 samples. The error bar represents the standard deviation of the mean.

The average of series resistance (R_S) dropped from 7.5 to 5.5Ω, and the average of shunt resistance (R_{SH}) dropped from 4.2×10^{11} to 3.5×10^{11} Ω.

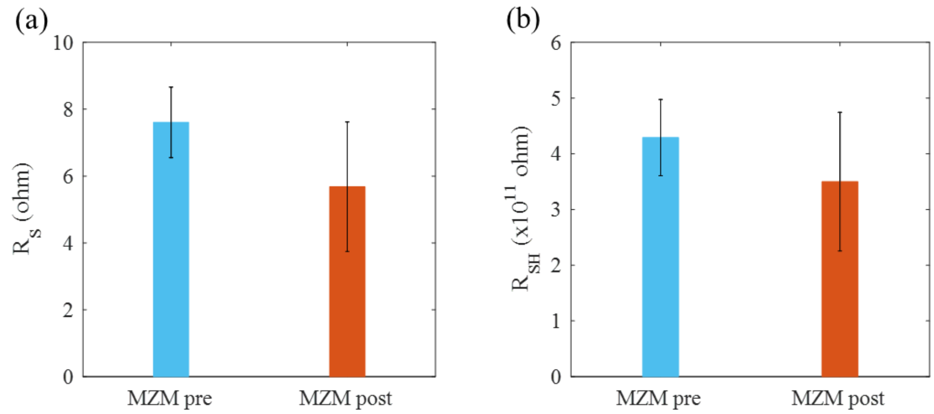

Figure 3.6 Resistance extraction from I-V tests. (a) Average of extracted series resistance (R_S) for the pre and post flight samples. (b) Average of extracted shunt resistance (R_{SH}) for the pre and post flight samples. For R_S, R_{SH}, each is based on 10 samples. The error bar represents the standard deviation of the mean.

3.2.4 High-speed response (RF) of silicon MZMs

The high-speed response was characterized by using the Optical Spectra analysis method [18]. The measurement schematics was shown in Figure 3.7(a). The optical carrier at the quadrature biasing point of MZM was generated from the tunable laser and was coupled into the input port of MZM by going through EDFA and polarization controller. For the two GSG pads of MZM electrical ports, one set of GSG pads was connected to VNA (Vector Network Analyzer, Brand: Anritsu, Model: 37397C) by RF probe, and another set of GSG pads was terminated by the 50 Ω terminator for impedance matching (Figure 3.7(a)). The output optical port of MZM was connected to the Optical spectrum analyzer to get the modulated First Sideband (FSB) signal. Reflection coefficient (S_{11}) was obtained from the VNA. For the pre and post flight sample of one MZM, there’s no obvious change in the reflection coefficient (Figure 3.7(b)).

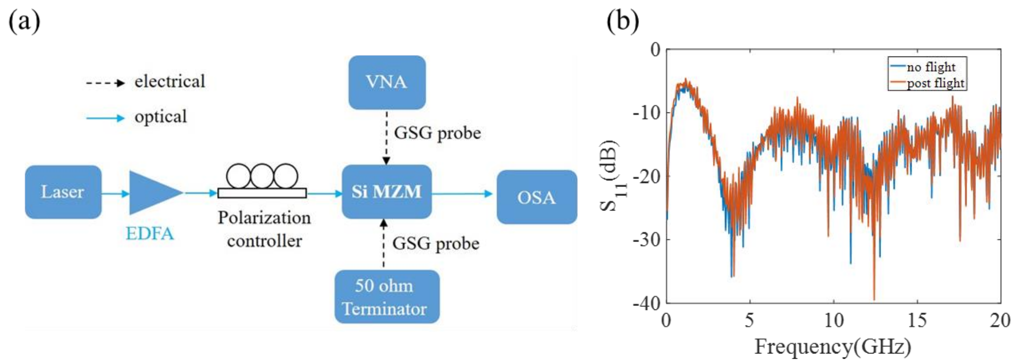

Figure 3.7 (a) Schematics of high-speed measurement. (b) Measured reflection coefficient (S_{11}) of pre and post flight MZMs.

The 3dB bandwidth of modulated FSB spectra were determined by the overall time constant τ (equation 3.4), which is related to RC constant (τ_{RC}), carrier recombination lifetime (τ_{rec}), and carrier transit time (τ_{tr}) (equation 3.4, 3.5) [19][20],

$$f_{3dB} = \frac{0.55}{\tau}. \tag{3.4}$$

The overall time constant is dependent on:

$$\frac{1}{\tau} = \frac{1}{\tau_{RC}} + \frac{1}{\tau_{rec}} + \frac{1}{\tau_{tr}}. \tag{3.5}$$

Reverse saturation current is inversely proportional to the carrier recombination lifetime:

$$I_0 \propto \frac{1}{\tau_{rec}}. \tag{3.6}$$

As the junction is a *p-n* junction for MZM, there should be a very limited width for the depleted region so that the carrier transit time (τ_{tr}) (depleted region width/fermi velocity) may be very limited and can be neglected. Overall, the 3dB bandwidth should be mainly determined by RC constant (τ_{RC}) and carrier recombination lifetime(τ_{rec}). RC constant can be obtained by multiplying the series resistance (R_S) and capacitance. RC constant of 10 *p-n* junction was averaged and normalized for comparison (Figure 3.8(a)). The reciprocal of the RC constant increased by about 20% after radiation. The carrier recombination lifetime is inversely proportional to the reverse saturation current I_0. As the I_0 increased over twice after radiation, the reciprocal of carrier recombination lifetime ($1/\tau_{rec}$) increased over two times as well. Hence, the reduced carrier recombination lifetime is dominant in the reduced total time constant.

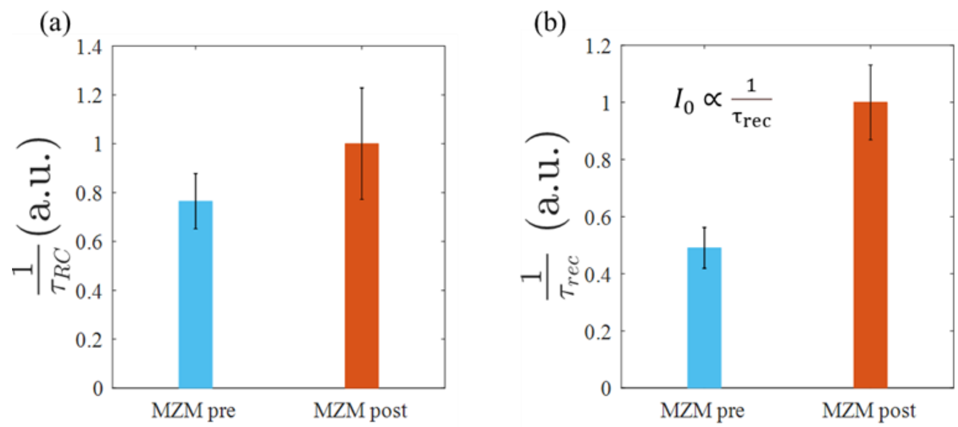

Figure 3.8 (a) The normalized reciprocal of RC constant ($1/\tau_{RC}$) extracted from C-V and I-V measurement (each based on 10 *p-n* junctions of MZM). (b) The normalized reciprocal of carrier recombination lifetime ($1/\tau_{rec}$) extracted from I-V measurement (each based on 10 *p-n* junctions of MZM). The error bar represents the standard deviation of the mean.

Figure 3.9 shows the results of the high-speed response. The compared pre and post-fight MZM was tested under the same quadrature wavelength, same optical input power, and same RF input power. The post flight MZM has broadened high-speed response compared pre flight MZM, nearly two times. Figure 3.9(b) shows the 3dB bandwidth of modulated FSB spectra of 3 for pre and post flight MZM devices. The position of 3 devices on the chip can be seen in Figure 3.9(b) inset. It can be seen that all three devices have nearly doubled 3 dB bandwidth after radiation (orange circle dots) compared with pre flight results (blue dash line). Previously it was mentioned that the bandwidth is mainly determined by the reciprocal of the RC constant ($1/\tau_{RC}$) and the reciprocal of carrier recombination lifetime ($1/\tau_{rec}$). And the reciprocal of carrier recombination lifetime ($1/\tau_{rec}$) increased over doubled after radiation, so increased bandwidth is mainly attributed to the reduced carrier recombination lifetime.

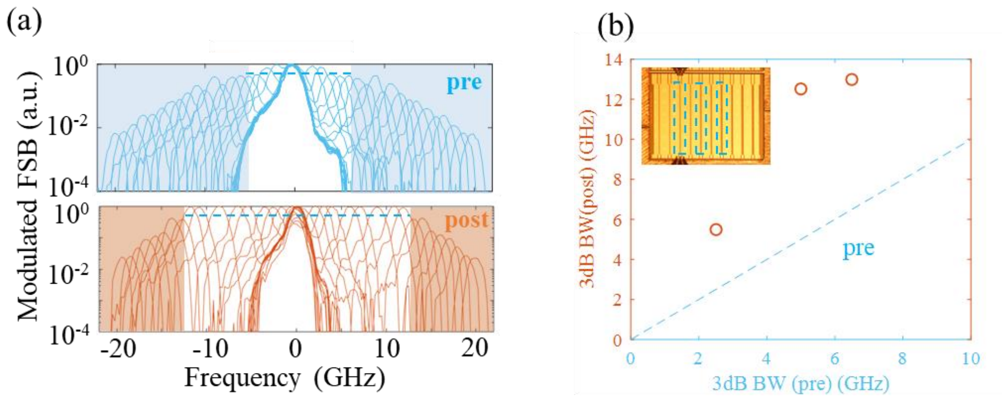

Figure 3.9 High-speed response. (a) The normalized modulated FSB (First sideband) spectra of one MZM. (b) 3dB Bandwidth before (pre) and after (post) radiation for three MZMs (inset: device positions on the chip).

3.2.5 Devices with abnormal optical transmission spectra

There are a few devices that didn't have the normal optical transmission spectra. After radiation, the optical spectra of those devices didn't have interference peaks and valleys (orange curves in Figure 3.10). The location of those devices on the chip is shown in Figure 3.11. Only 10% of devices in the whole chip have such abnormal optical transmission spectra, while the rest of the devices can work normally.

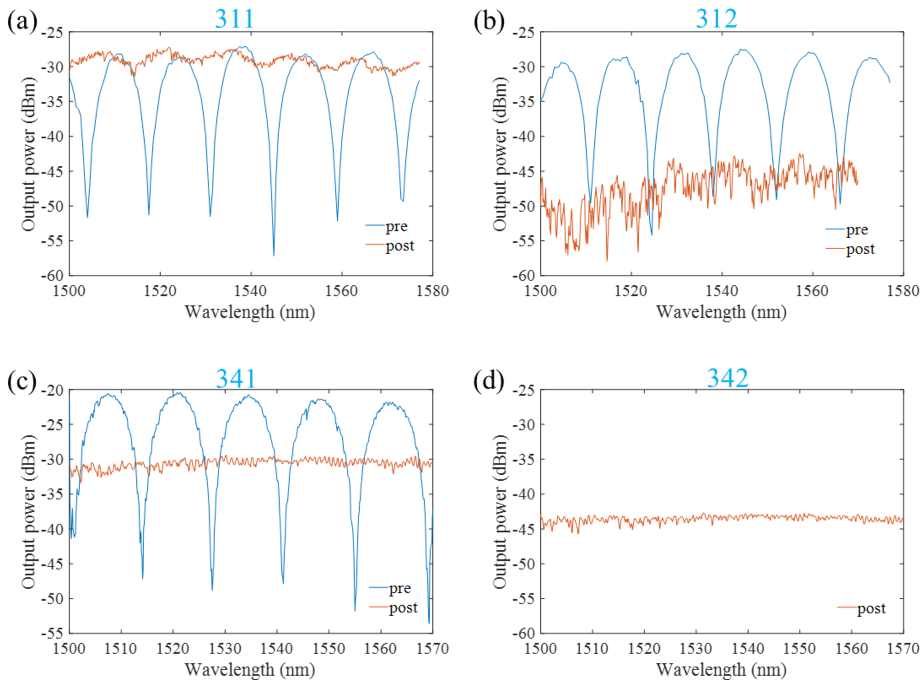

Figure 3.10 (a~d) Optical transmission spectra of pre flight devices (blue curve) and partially damaged post flight devices (orange curve).

Other responses, including electrical response (I-V), electrical high-speed response (S_{11}), and EO response under forward and reverse bias were measured for those devices with abnormal optical transmission spectra. All other responses behave normally (Figure 3.12(a~d)). It is speculated that the abnormal optical transmission spectra were due to the partial damage in the optical waveguide layer during the radiation process. Probably the power splitter or one arm of MZM got partially damaged during radiation so there's no interference peak or valley.

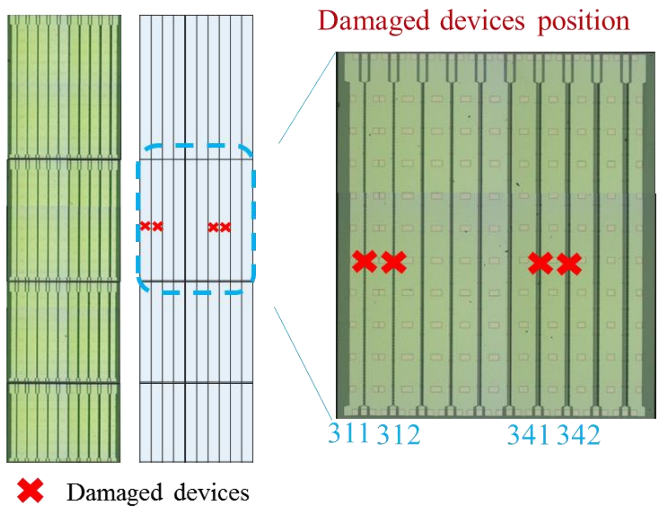

Figure 3.11 Diagram of damaged devices (10%, 2/20) position in the chiplet.

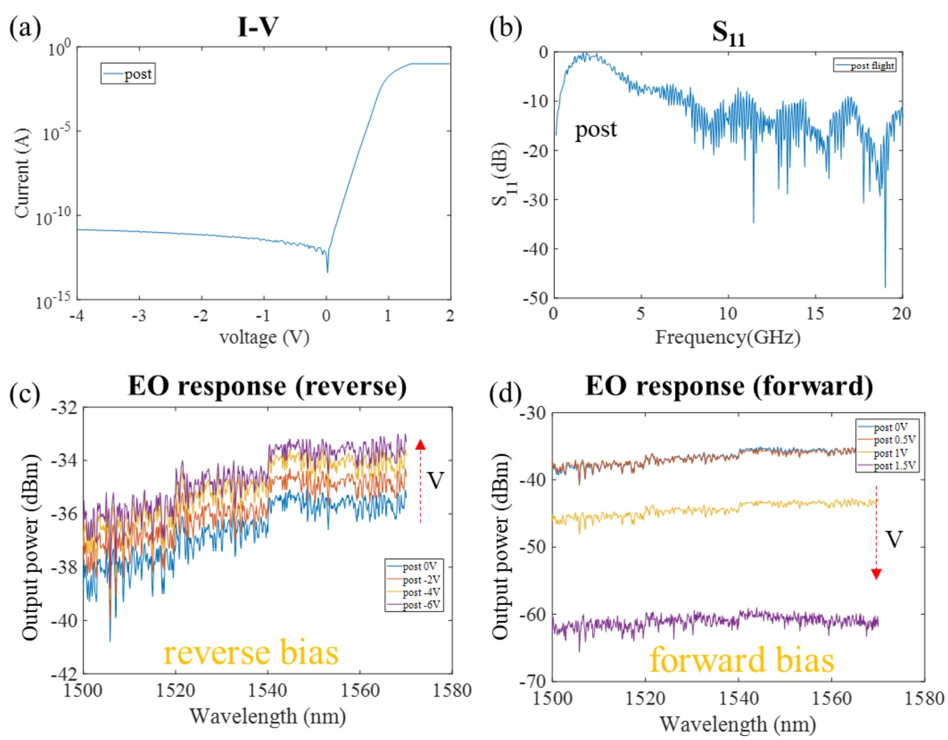

Figure 3.12 (a) Measured I-V curve, (b) S_{11}, (c) EO response under reverse bias, (d) EO response under forward bias for one device #341 (post) flight in Figure 3.10 and Figure 3.11.

3.3 Summary

In this work, we investigate the performance change of silicon MZMs after cosmic radiation. Optical transmission spectra, electrical response (I-V, C-V), EO (DC) response, and the high-speed response of MZMs have been measured, analyzed, and compared. Devices of 90% are still able to operate after radiation. Increased effective index (on the order of 10^{-3}), increased dark current, reduced carrier recombination lifetime, and increased 3dB bandwidth of high-speed response have been observed. The material property change reflected from the measurement results is probably induced by the total ionized damage. A few possible solutions may be used, such as post-radiation annealing under forward bias to neutralize the trapped holes or to utilize active devices of high doping levels to enhance the radiation tolerance [12]. This work paves the fundamental step for future deploying photonics integrated circuits in space laser communications.

REFERENCES

[1] E. A. Park, et al, "NASA's Next Generation ⩾100 Gbps Optical Communications Relay," IEEE Aerospace Conference, 1-9, 2019

[2] F. De Leonardis, et al, Modeling of Radiation Effects in Silicon Photonic Devices, IEEE Transactions on Nuclear Science, 62, (5), 2155-2168, 2015

[3] S. Nasr-Storey, et al, Effect of Radiation on a Mach–Zehnder Interferometer Silicon Modulator for HL-LHC Data Transmission Applications, IEEE Transactions On Nuclear Science, 62, 329 – 335, 2015.

[4] Q. Du, et al, Gamma radiation effects in amorphous silicon and silicon nitride photonic devices. Optics Letters, 42, 3, 587-590, 2017.

[5] G. Tzintzarov, et al, Integrated Silicon Photonics for Enabling Next-Generation Space Systems, Photonics, 8, 131, 2021.

[6] G. Messenger, A summary review of displacement damage from high energy radiation in silicon semiconductors and semiconductor devices, IEEE Transactions On Nuclear Science, 39, 468 – 473, 1992.

[7] H. Stein, Comparison of Neutron and Gamma-Ray Damage in n-Type Silicon, Journal of Applied Physics, 37, 3382, 1966.

[8] Q. Du, et al, Real-time, in situ probing of gamma radiation damage with packaged integrated photonic chips. Photonics Research, 8, 2, 186-193, 2020.

[9] F. Morichetti, et al, Alpha Radiation Effects on Silicon Oxynitride Waveguides. ACS Photonics 3, 9, 1569–1574, 2016.

[10] S. Grillanda, et al, Gamma radiation effects on silicon photonic waveguides. Optics Letters, 41, 13, 3053-3056, 2016.

[11] V. Eremin, et al, Carrier drift mobility study in neutron irradiated high purity silicon, Nuclear Instruments and Methods in Physics Research A, 362, 338-343, 1995.

[12] Q. Du, High energy radiation damage on silicon photonic devices: a review, Optical Materials Express, 13(2), 403-412, 2023

[13] C. Han, et al, Proton radiation effects on high-speed silicon Mach-Zehnder modulators for space application, Science China Information Sciences, 65, 222401, 2022

[14] P. Dong, et al, Low Vpp, ultralow-energy, compact, high-speed silicon electro-optic modulator. Optics Expres, 17, 25, 22484-22490, 2009.

[15] P. Dong, et al, Coplanar-waveguide-based silicon Mach–Zehnder modulator using a meandering optical waveguide and alternating-side *P-N* junction loading. Optics Letters, 41, 18, 4401-4404, 2016.

[16] https://support.lumerical.com/hc/en-us/articles/360042327954-Calculating-modulation-response-MZM-example

[17] S.O. Kasap, Optoelectronics and Photonics: Principles and Practices, Pearson; 2nd edition, 2012

[18] Y. Shi, et al, High-speed electrooptic modulator characterization using optical spectrum analysis. Journal of Lightwave Technology, 21, 2358, 2003.

[19] N. Flöry, et al, Waveguide-integrated van der Waals heterostructure photodetector at telecom wavelengths with high-speed and high responsivity, Nat. Nanotechnol. 15, 118–124, 2020.

[20] S. Lischke, et al. Ultra-fast germanium photodiode with 3-dB bandwidth of 265 GHz. Nat. Photon. 15, 925–931, 2021.

Chapter 4

SMALL SIGNAL ANALYSIS AND DEVICE MODELING OF GRAPHENE SILICON HETEROGENUOUS JUNCTIONS FOR HIGH-SPEED OPTOELECTRONICS

4.1 Introduction

Developing the Complementary Metal-Oxide-Semiconductor (CMOS) compatible hybrid integration of low-dimensional materials on a scalable silicon (Si) photonic platform has many promising opportunities for high-performance optical transceiver components and sensor systems [1]. The Silicon platform offered by Foundries provides low-loss and large-scale photonic integration. However, the nonlinear carrier plasma dispersion effect, the limited carrier mobility, and the indirect bandgap of Si are still the potential bottlenecks for many efficient, high-speed optoelectronic and laser applications.

As a semi-metal with zero bandgap material, Graphene (G) has arisen plenty of research attention for its superior electrical and thermal conductivity. It could interact with light over a wide spectral range from microwave to ultraviolet wavelengths, showing it a great candidate for light detection, modulation, and manipulation [2]. Since it has high carrier mobility (up to 10^5 cm^2 $V^{-1}s^{-1}$), Graphene is also studied for high-speed optoelectronic devices[3]. Hybrid integration of G on CMOS compatible silicon platform provides many chip-scale optoelectronic applications.

4.2 Small signal analysis for RC constant limited Graphene silicon optoelectronics

Directly contacted low dimensional materials (e.g., Graphene) on a CMOS-compatible silicon homojunction offer a new platform for post-fabrication free high-speed hybrid optoelectronic devices on chip. However, deterministic and scalable doping control in semimetal G still has to be studied and understood [4][5]. Electrostatic carrier distribution, as well as the dynamics of externally injected carriers, are strongly affected by the varying Schottky barriers on the vertical heterojunction [6]. Knowing more about junction formation and variation under electrical injections on the multi-junction interface between directly contacted G and Si devices is necessary for analyzing and predicting the performance limit of the device's radio frequency (RF) response [7][8].

In this work, the high-speed RF response of a graphene-directly contacted silicon *p*-*i*-*n* junction is investigated and analyzed. The multi-junction components of the hybrid structure are parameterized by fitting a small-signal model to the broadband RF response of the hybrid device under a series of carrier injection rates. The built-in electric field formed between the substrate-induced electro-static doping G and Si is also studied to analyze the variation of heterojunction components under different carrier injections. By engineering the device dimensions, it is able to further reduce the resistance-capacitance constant to be sub-picosecond and enable bandwidth towards sub-Terahertz operation. The G-Si *p*-*i*-*n* junction hybrid structure is useful for components in high-speed optical communication with low cost and a CMOS-compatible fabrication process.

4.2.1 Device schematics

The top view of the device is shown in Figure 4.1(a). Light is coupled into the PhC WG (180 μm) through channel WGs [9]. G is directly covered on heavily p, intrinsic, and heavily n doped silicon regions (Figure 4.1(b)). The ion-implanted p and n regions have the same doping density of 5×10^{18} cm^{-3}. The intrinsic region is left non-intentionally doped, which is characterized to be lightly n doped with a doping density of 10^{16} cm^{-3}. The metal electrodes are connected to the doped Si regions through via in the SiO_2 layer. The 250 nm PhC WGs are in the 250 nm Si layer, above the 2 μm oxide layer. The suspended G near the edges of the trench is removed during an Acetone bath and electrically isolated from metal electrodes, as shown in the scanning electron microscope (SEM) image in Figure 4.1(c). The atomic force microscope (AFM) image (Figure 4.1(d)) shows the full coverage of G membrane cladding on Si suspended PhC WG region. The optical mode profile shows the confined mode in Si-suspended PhC WG and coupled to the G layer (Figure 4.1(e)).

The substrate-induced electrostatic doping in G is characterized by a Micro-Raman spectrometer, with a 532 nm excitation laser and spot size of 0.6 µm (Figure 4.1 (f-g)). Low optical power below 1 mW is used to avoid any nonlinear response. The Raman spectra of the G directly contacted *n-Si*, *i-Si*, and *p-Si* regions are in the blue, black, and red curves in Figure 4.1 (f-g) (also marked as dots in Figure 4.1(d)). All the laser parameters remain the same throughout the measurement and leave the substrate doping level as the only variable. Higher doping levels decrease the free carrier lifetime and phonon lifetime, and lead to a low background signal of the G Raman spectra (red and blue curves in Figure 4.1(f-g)). From the Raman spectra, it shows the reduced intensity ratio of 2D versus G peak, and the blue shift of 2D peak for G on *p*-doped Si and G on *n*-doped Si. This verifies that Graphene is electrostatically doped by the Si substrate since 2D peaks of G are sensitive to the doping level variations in graphene. The 2D peaks have a blue shift of 5 cm^{-1} for G on *p*-doped Si and 4 cm^{-1} for G *n*-doped Si. The trends that both doping-dependent Raman spectra are consistent with the observations reported in previous work [10]. The Dirac point of G is between the Silicon's conduction and valence bands. Direct contact between graphene and *p/n*-doped Si makes positive/negative band bending in silicon and induces the electrostatic charge in graphene in opposite signs [4].

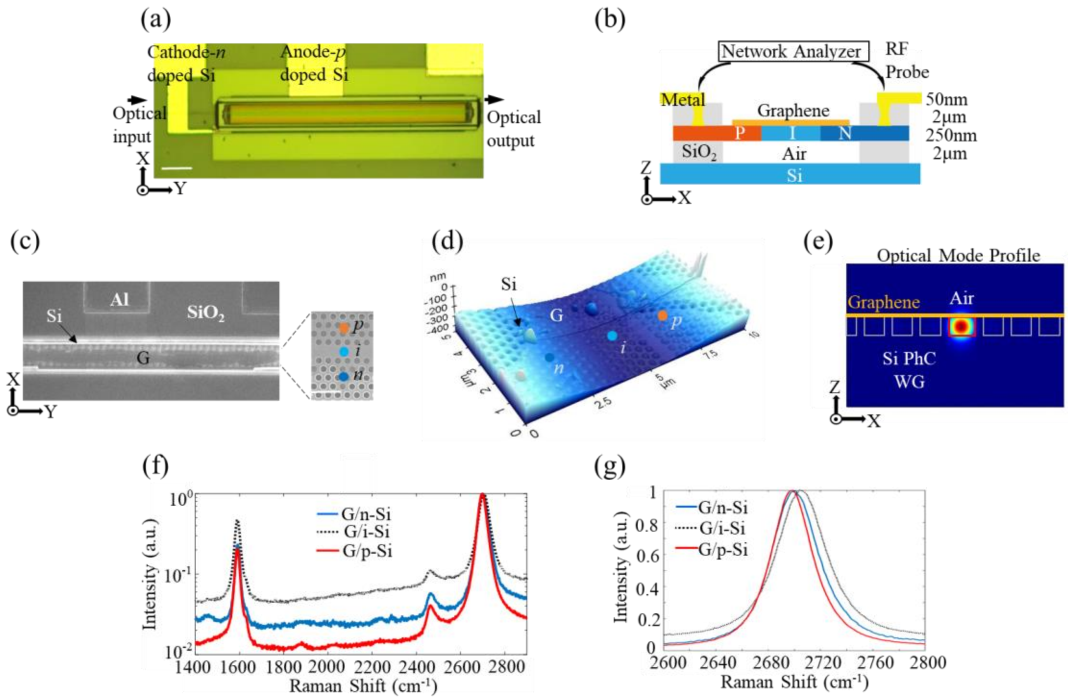

Figure 4.1 Figure Device schematics (a) Optical image of the device top view (Scale bar: 20 μm). (b) The cross-sectional electrical design of the device. (c) Scanning electron microscope (SEM) image of the G-covered Si PhC WG (Scale bar: 20 μm). Inset: an enlarged image of the device schematics, three circles from top to bottom mark the probed laser spot for G on *p*-doped Si, *i*-doped Si, and *n*-doped Si for Raman spectra, respectively (Scale bar: 1 μm). (d) Atomic Force Microscopy image of G covered Si PhC WG. (e) The cross-sectional optical mode profile at 1550 nm for G-Si photonic crystal waveguide (PhC WG). (f) Raman spectrum of G on *n*-doped, intrinsic, and *p*-doped Si. (g) Raman spectra of the 2D peak in (f). All the Raman spectra were taken without external bias.

4.2.2 Electrical (DC and RF) responses and Small Signal Model analysis

Direct current (DC) and alternating current (AC) responses of the monolithic (Si) and hybrid (G-Si) devices are measured and analyzed (Figure 4.2).

For the DC response, current-voltage (IV) measurements of monolithic (red triangular) and hybrid (blue circle) are presented in Figure 4.2(a). By fitting the diode equation 4.1 to the experiment data, it is able to extract the parameters and analyze the difference between the two devices [11][12],

$$I = I_0 e^{\frac{q(V+IR_S)}{nkT}} + \frac{V + IR_S}{R_{SH}}, \tag{4.1}$$

where I is the dark current, I_0 is the reverse saturation current, R_S is the total series resistance (including *p/n* doped region resistance, interconnect resistance, and DC probe contact resistance during the test). R_{SH} is the shunt resistance, k is the Boltzmann constant, and T is the temperature.

The series resistance (R_S) reduces from R_{S_Si} = 0.51 kΩ (monolithic device) reduces to $R_{S\_G\text{-}Si}$ = 0.29 kΩ (hybrid device). The shunt resistance (R_{SH}) reduces from R_{SH_Si} = 148 kΩ (monolithic device) to $R_{SH\_G\text{-}Si}$ = 36 kΩ (hybrid device). The reverse saturation current(I_0) increases from I_{0_Si} = 0.286 μA (monolithic device) to $I_{0\_G\text{-}Si}$ = 2.36 μA (hybrid device). The high conductivity of graphene reduces the series and shunt resistivity of the hybrid device. Since the reverse saturation current is inversely proportional to the carrier lifetime, it is speculated that the effective carrier lifetime in the hybrid device reduces to 1/10 compared to the monolithic device.

Since the DC measurement can't analyze individual components of the multiple vertical and lateral junctions in the hybrid device, broadband AC (RF) measurement (0.7 ~ 40 GHz) and corresponding Small-Signal Model are utilized for separating parameters and analyzing the variations of different junctions.

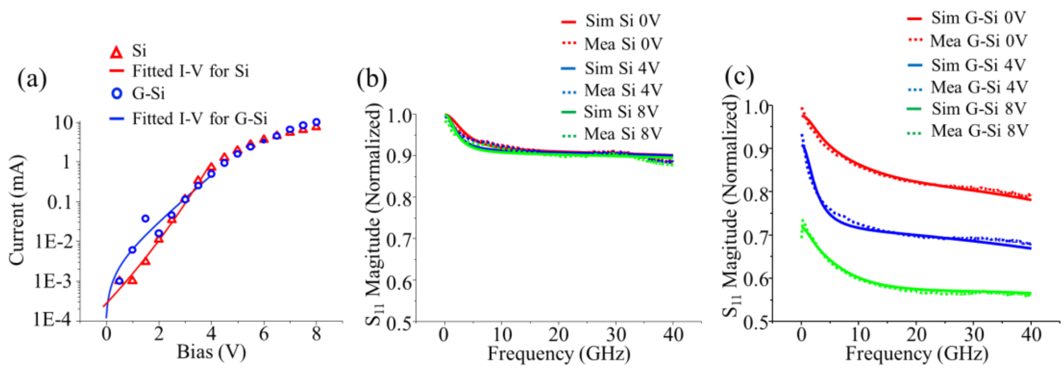

Figure 4.2 Direct current and alternating current characterization for the hybrid devices. (a) I-V curves for Si *p-i-n* (red triangular), fitted I-V for Si *p-i-n* (red line), G-Si hybrid *p-i-n* junction (blue circle), and fitted I-V for G-Si hybrid *p-i-n* junction (blue line). (b) Measured and modeled S11 magnitude of Si. (c) Measured and modeled S11 magnitude of G-Si.

For the AC response, the reflection coefficient (S_{11}) of monolithic (Figure 4.2(b)) and hybrid (Figure 4.2(c)) devices are measured from 0.7~40 GHz under the forward bias of 0, 4, 8V. The forward bias significantly modifies the RF (S_{11}) response of the hybrid device, indicating that the junction formation (capacitance, inductance, and resistance in G/Si contacts) vary significantly under bias (Figure 4.2(c)).

However, the depletion region of the monolithic device changes very little under the forward bias of 8V (Figure 4.2(b)).

Small-Signal Model is proposed to analyze the multi-junction variations for the monolithic (Figure 4.3(a)) and hybrid (Figure 4.3(b)) devices [12]-[15]. The junction components of the small-signal model for monolithic and hybrid devices are shown in Figure 4.3(a) and (b) respectively. The red, blue, and deep-blue regions represent the Si *p* doped, intrinsic, and *n* doped regions in Figure 4.3. The golden region is the Graphene contacted to the Si *p-i-n* junction for the hybrid device (Figure 4.3(b)). In the monolithic device (Figure 4.3(a)), R_3 represents the contact resistance between metal and heavily doped Si. R_5 represents the series resistances of doped Si. C_1 and R_2 are the parasitic capacitance and resistance from the substrate. The leakage current between the electrodes is presented by R_1. R_{pi} and R_{in} represent the resistances between *p-i* region, *i-n* region respectively. C_{pi}, C_{in} are the capacitances between *p-i* region, *i-n* region respectively. In the small-signal model for the hybrid device (Figure 4.3(b)), G-related components (vertical heterojunctions for G-Si contacts and G homojunctions) are added based on the monolithic model. $R_{gp\text{-}i}$ and $R_{gn\text{-}i}$ represent the series resistances of G between *p-i* and *n-i* regions respectively, $L_{gp\text{-}i}$ and $L_{gn\text{-}i}$ represent the inductances of G between *p-i* and *n-i* regions respectively. Three independent Resistance-Capacitance (RC) elements are the vertical junctions formed between G and silicon with different doping levels: junction capacitances C_{jp}, $C_{ji,}$ and C_{jn} represent the capacitances between G and *p, i, n* regions. Junction resistances R_{jp}, $R_{ji,}$ and R_{jn} are the resistances between G and *p*, *i*, *n* regions respectively.

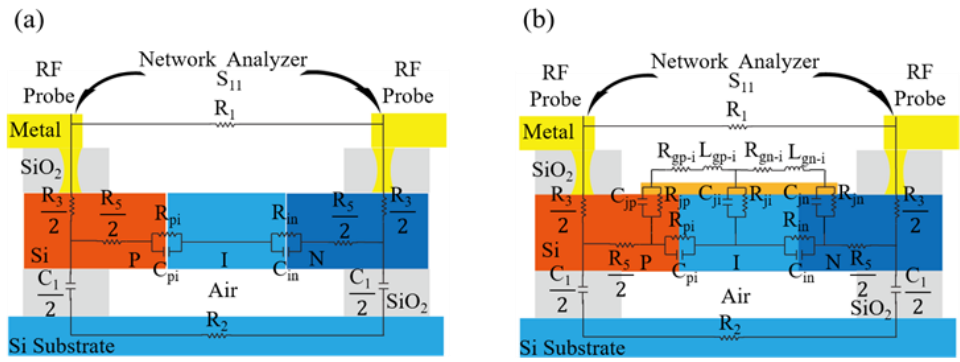

Figure 4.3 Small-signal models for (a) monolithic Si *p*-*i*-*n* junction, (b) G-Si hybrid *p*-*i*-*n* junction.

The simulated reflection coefficient (S_{11}) (solid lines in Figure 4.2(b-c)) of the Small-Signal Model is fitted to the experimental data (dash lines in Figure 4.2(b-c)) by using Keysight Advanced Design System (ADS) [16]. The Gradient algorithm was used to optimize the curve fitting results in ADS. At each bias voltage, the corresponding circuit elements (R, L, C) are optimized globally to minimize the difference between the simulated and the measurement data. Responses under the bias voltages of 0, 4, and 8 V are shown here for clear and consistent demonstration, and responses under other bias voltages can be found in the journal paper [8]. All the simulated responses for all the biases fit well with the corresponding experimental data.

The junction parameters of the monolithic device are first extracted after curve fitting (Figure 4.2(b)). Next, based on the components of monolithic devices, the proposed junction components of G-Si heterojunctions and G homojunctions are extracted after fitting for the hybrid devices (Figure 4.2(c)).

Under forward bias, the higher injection level increases the effective G doping level and conductivity [8]. Numerical estimation of G conductivity and inductance related to doping level can be seen in Section 3.2.5. By fitting the small-signal model to the S_{11} under different voltages, it is able to extract each junction variation with forward bias (Figure 4.4). For the G homojunctions (L_{gp-i}, L_{gn-i}, R_{gp-i}, R_{gn-i}), both resistance and inductance decrease with the bias, showing the increased carrier density in G with carrier injection through substrate *p-i-n* junction (Figure 4.4(a-b)). For the G-Si heterojunction components (capacitance and resistance between G and Si interface), capacitance (Figure 4.4(c)) and resistance (Figure 4.4(d)) in the *G-n* Si region vary most significantly with forward bias. The voltage-dependent capacitance variation of G-Si contacts depends on the substrate doping levels (Figure 4.4(c)). Capacitances of *G-p* Si and *G-i* Si vary little with the increasing bias while *G-n* Si capacitance increases with bias. The junction resistance shows that R_{ji} and R_{jp} change only by a small amount while R_{jn} decreases as the bias increases. For the results of junction capacitance and resistance in Figure 4.4(c-d), it is indicated that the bias-dependent RC constants have an obvious drop on the *G-n* Si contact junction. This originated from the significant decrease of both the junction capacitance C_{jn} and resistance R_{jn} with forward bias rather than the capacitance and resistance in other G-Si contacted regions (Figure 4.4 (c-d)).

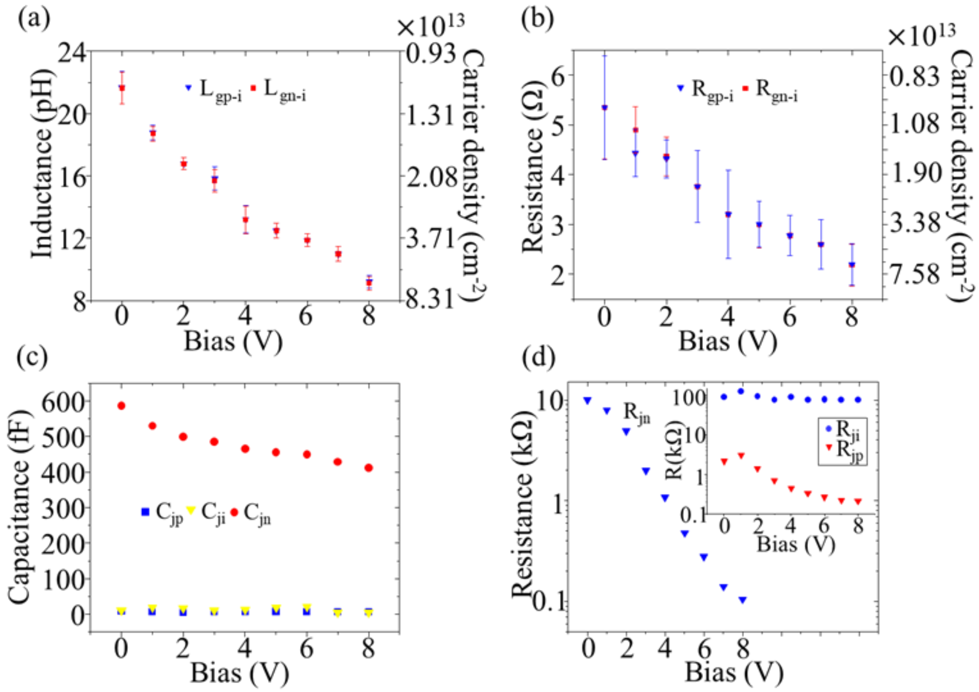

Figure 4.4 Elements of G-Si junction (in Figure 4.3(b)) varying under bias. (a) Inductance of G homojunction (L_{gp-i}, L_{gn-i}) versus bias voltage and the estimated carrier density in G; (b) Resistance of G homojunctions (R_{gp-i}, R_{gn-i}) versus bias voltage [18][19] and estimated carrier density in G. The details of G inductance and resistance estimation varying with carrier densities can be seen in the section of 3.2.5; (c) Capacitance of G-Si junction in *p, i* and *n* region; (d) Resistance of G-Si junction in *p, i* and *n* region [8]. The error bars in (c) and (d) are negligible.

4.2.3 Simulated Built-in Electrical Fields

The small-signal models in Figure 4.3 are proposed based on the junction variations under forward bias (Figure 4.5). And the junction variations are induced by the vertical built-in electric field in the hybrid device under increasing bias [8]. The built-in Electrical Fields variation should be numerically analyzed to see the relations with the results of small-signal models.

The simulated built-in electric field is performed by the Lumerical Charge solver[17]. The Finite element method is used to solve the Poisson equation for getting the electrostatic potential (as well as the electric field).

$$-\nabla \cdot (\varepsilon \nabla V) = q\rho, \tag{4.2}$$

where ε is the dielectric permittivity, V is the electrostatic potential ($E = -\nabla V$), and ρ the net charge density [17].

Simulated x component (in plane) and z component (out of plane) built-in electric field distribution on the cross-sectional plane of the monolithic devices are shown in Figure 4.5(a-b) (corresponding to Figure 4.3(a)). Simulated x component (in plane) and z component (out of plane) for the hybrid devices are presented in Figure 4.5(c-d) (corresponding to Figure 4.3(b)). In-plane built-in electric fields on the top surface of the Si membrane are compared for the monolithic and hybrid devices (Figure 4.5(e)). It shows that the in-plane electric field is formed in the highly conductive G layer (blue curve in Figure 4.5(e)). The out-of-plane built-in electric fields along the G-Si interface are also shown and compared for the monolithic and hybrid devices (Figure 4.5(f)). Since the Fermi level of G is between the *p* doped and *n* doped silicon, the out-of-plane built-in electric field changes direction for G on *p* doped Si (left side for the blue curve in Figure 4.5(f)) and *n* doped Si (right side for the blue curve in Figure 4.5(f)), which assists the transfer of the electrons (on *G-n* Si interface) and holes (on *G-p* Si interface) from G into Si.

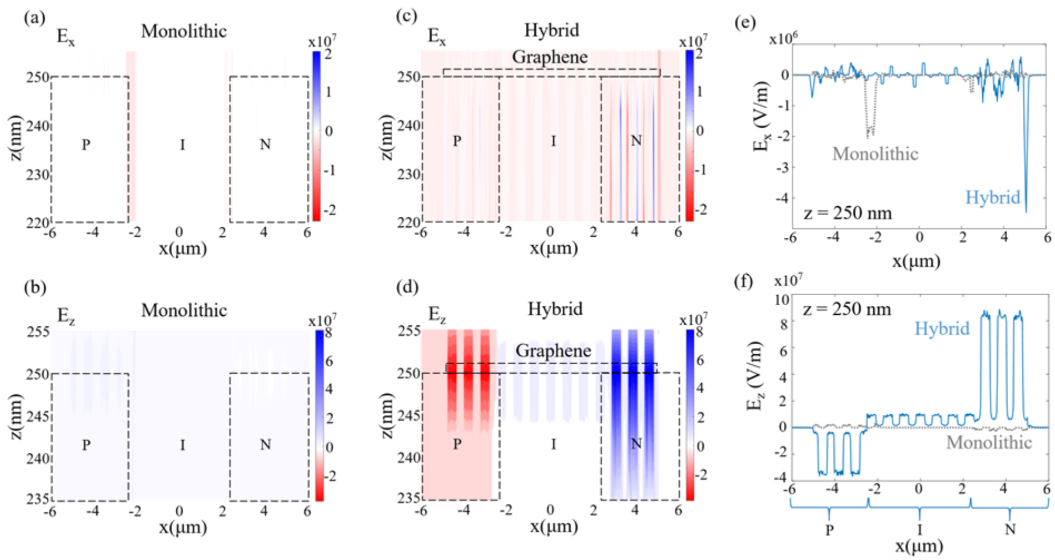

Figure 4.5 Built-in electric fields at G-Si interface under zero bias. (a) x and (b) z component of built-in electric fields on the cross-sectional plane of monolithic Si *p-i-n* junction. (c) x and (d) z components of built-in Electrical fields of the hybrid device. (e) x and (f) z components of the built-in electric field on the graphene and silicon interface.

The fitted parameters extracted from the small signal model are consistent with the simulated built-in electric fields: z component (corresponding to vertical junction) of the built-in electric field around the *G-n* junction is much larger than other junctions as shown in Figure 4.5(d).

Comparing the small signal model and built-in electric field simulations, it shows that the *G-n* Si varies most significantly with the forward bias. The in-plane (E_x) and out-of-plane (E_z) built-in electric field components at the *G-n* Si interface under a bias of 0V and 8V are compared in Figure 4.6. Under forward bias, a strong lateral electric field (E_x) is formed out of the boundary of *G/n*-Si contact (Figure 4.6(b)), while the extra vertical built-in electric field is formed under the edge of G

(Figure 4.6 (d)). The extra depletion region formed near the edge of *G/n*-Si contact leads to decreased resistance and capacitance (Figure 4.6(b)(d)).

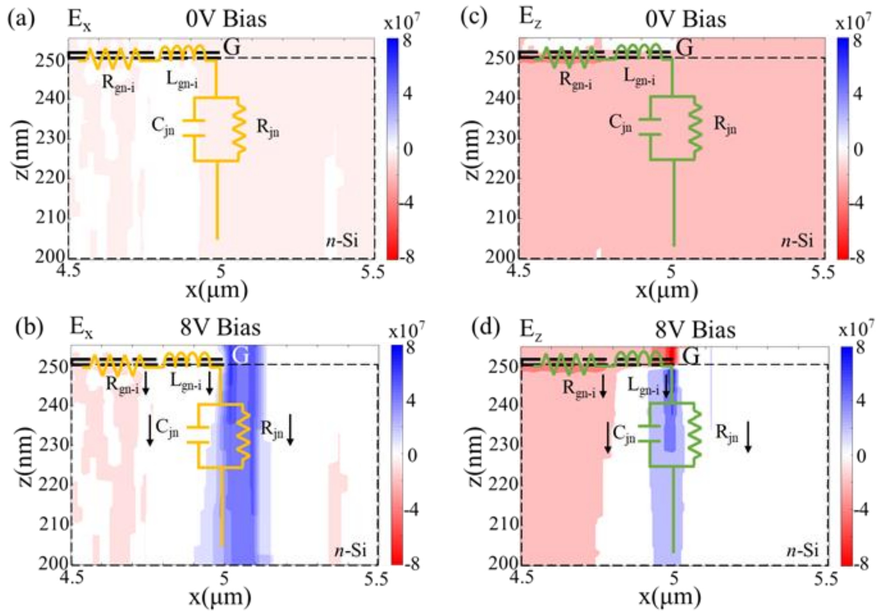

Figure 4.6 Bias-dependent depletion region on *G-n* Si. Built-in electric field components (a) E_x under 0V, (b) E_x under 8V, (c) E_z under 0V, (d) E_z under 8V bias at *G-n* region of Si interface for the vertical junction, respectively. For the built-in electric field components of the hybrid device under other intermediate biases voltage across the *p-i-n* junction can be seen in [8].

4.2.4 Estimation of graphene inductance, resistance

Based on the fitted resistance and capacitance of graphene, it is able to estimate the range and scale of G doping levels [1].

To verify the fitting results of the small signal model, the estimation of graphene inductance and resistance is conducted for reference.

Researchers have studied on-graphene kinetic inductance based on the graphene model as a transmission line. The kinetic inductance can be written as: [18]

$$L_k W = \frac{\pi \hbar}{e^2 v_F} \times \frac{1}{\sqrt{n_0}}, \tag{4.3}$$

where the parameters shown in the equation can be seen in the following table:

	Description	**Value**
v_F	Fermi velocity	$10^6\ m/s$
e	Electric charge	$1.6\times 10^{-19}\ C$
$\hbar$	Reduced Planck's constant	$1.0545718 \times 10^{-34}\ J\cdot s/rad$
n_0	Carrier density	$10^{10}\sim10^{14} cm^{-2}$
W	Width of graphene	$2.5\ \mu m$
L_k	The kinetic inductance of graphene per unit length	

Table 4. 1 Parameters used for calculating graphene inductance.

Here we estimate a range for the carrier density in graphene to be 10^{10} to 10^{14} cm^{-2}, and graphene sheet inductance is shown as follows:

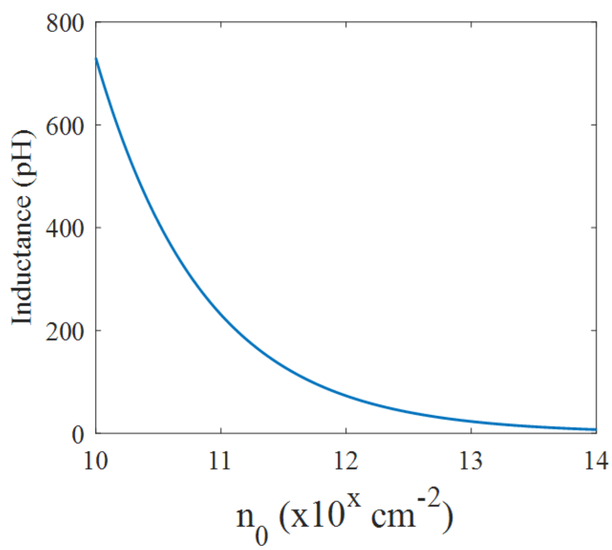

Figure 4.7 Calculated graphene inductance varying with carrier density.

As shown in Figure 4.7, the graphene inductance ranges from 7.301~730.1 pH per square as density varies from $10^{10}\sim10^{14}$ cm^{-2}. In Figure 4.4(a), extracted graphene inductance after curve fitting ranges approximately from 8~24 pH which is corresponding to the G carrier density from 8.31~0.93×10^{13} cm^{-2}.

For the graphene resistance, calculated results are compared with the fitting results in Figure 4.4(b). The calculation of graphene resistance is shown below.

Resistance is defined as the following:

$$R = \frac{\rho l}{A}. \tag{4.4}$$

Resistivity ρ is inversely proportional to the conductivity σ:

$$\rho = \frac{1}{\sigma}. \tag{4.5}$$

Conductivity σ is determined by the mobility μ and carrier density n, mean free path l_c is shown as [19][20]

$$\sigma = en\mu = \frac{2e^2(k_F l_c)}{h}, \tag{4.6}$$

where 2D Fermi wave vector k_F is determined by:

$$k_F = (\pi n)^{\frac{1}{2}}. \tag{4.7}$$

The resistance of graphene can be written as the following:

$$R = \frac{\rho l}{A} = \frac{l}{\sigma A} = \frac{h \cdot l}{2e^2(k_F l_c)A} = \frac{h \cdot l}{2e^2\left((\pi n)^{\frac{1}{2}} l_c\right)A}. \tag{4.8}$$

Based on the equation above, for the hybrid device, parameter values of graphene resistance can be cited in Table 4.2. And the carrier density of G is estimated to be 10^{10} to 10^{14} cm^{-2}:

	Description	**Value**
$\boldsymbol{h}$	Planck's constant	$6.626 \times 10^{-34}\, J \cdot s$
$\boldsymbol{l}$	length	*2.5 μm*
$\boldsymbol{e}$	Electric charge	*1.6*$\times 10^{-19}\, C$
$\boldsymbol{l_c}$	Mean free path	*3.5 μm*
$\boldsymbol{A}$	Area of graphene	*3 μm*
$\boldsymbol{n_0}$	Carrier density	10^{10}~$10^{14}/cm^2$

Table 4. 2 Parameters used for calculating graphene resistance.

Thus, graphene sheet resistance varying with carrier density is shown as follows:

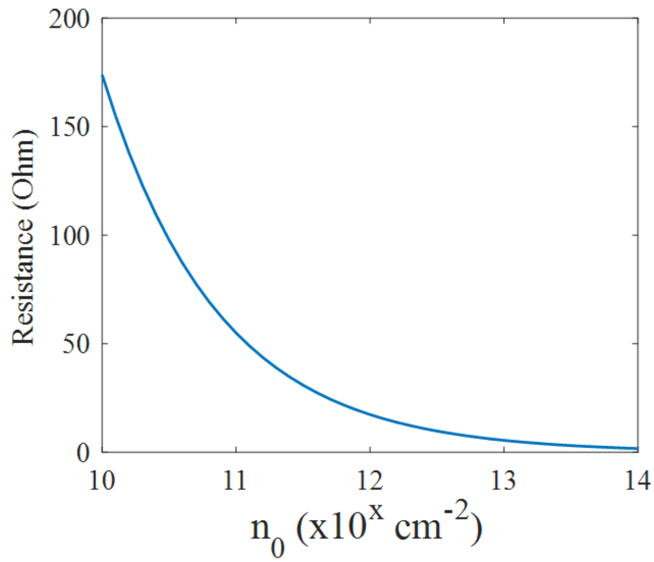

Figure 4.8 Graphene resistance varying with carrier density.

Based on calculated results, it shows that the graphene resistance ranges from 1.7~173.8 Ohm as the carrier density varies from 10^{10}~10^{14} cm^{-2} (Figure 4.8). In Figure 4.4(b), extracted graphene resistance after curve fitting ranges approximately from 2~6 Ohm which corresponds to the carrier density 7.58~0.83×10^{13} cm^{-2} referring to Figure 4.8. The estimated carrier density based on graphene resistance is very close to the estimated carrier density based on graphene inductance. These results show the consistency and reasonableness of the carrier density estimation based on the fitting results. The carrier density in G is estimated to be around 10^{13} cm^{-2}.

4.2.5 Bandwidth analysis

The proposed small-signal model of the hybrid device is able to extrapolate the RC constant (1.5 ps) based on the device's RF response (S_{11}) and simulate the S_{11} over a wider frequency range (Figure 4.9(a)). The 3dB bandwidth of the optoelectronic device's photoresponse is limited by both RC constant and carrier transit time. Experimentally the photoresponse is verified up to 40 GHz beyond the instrument bandwidth limitation (Figure 4.9(b)). Furthermore, the RC constant could be further reduced by decreasing the capacitance of G and *n-Si* contact. Among the multi-components (*R*, *L*, *C*) variation under bias in the small signal model, the capacitance variation on *G/n* Si region is most sensitive to the forward bias (Figure 4.4(d)). Decreasing *G/n* Si capacitance will lead to the reduction of the overall RC constant and further improve the 3 dB bandwidth. The capacitance of *G/n* Si contact can be reduced by increasing the depletion region in *n* Si. Reducing the doping density in *n* Si can effectively enhance the depletion region.

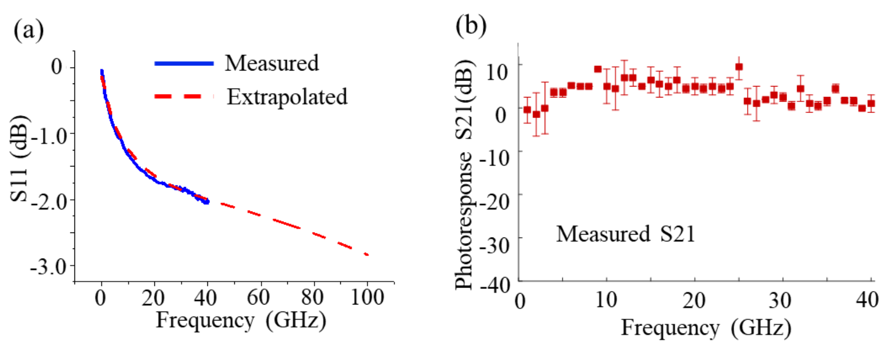

Figure 4.9 Broadband RF response of the device. (a) Measured (solid blue curve) and small signal model extrapolated S_{11} (red dashed line) from 0 to 120 GHz under zero bias (b) measured photo-response S_{21} from 0 to 40 GHz for G-Si *p*-*i*-*n* junction.

4.2.6 Summary

In this work, we investigate the voltage-dependent multi-junction variation in the hybrid Graphene-Si *p*-*i*-*n* junction. Based on the graphene integrated Si CMOS compatible platform, the multiple G-Si junctions and G homojunctions are parameterized by curve-fitting the small-signal model to the RF experimental data. The results are compared to the simulated built-in electric field distribution. The simulation results show that the RC constant of the hybrid device is about 1.5 ps based on the curve fitting of RF response S_{11}. The applied forward bias through Si *p*-*i*-*n* junction substrate can effectively modify the G doping levels and vertical built-in electric field on G-Si contact, And the *G*-*n* Si space varies most significantly with forward bias. As the RC constant limit is always the bottleneck of hybrid 2D material-based active silicon photonic components, the result will be useful for designing high-speed integrated active optoelectronic devices based on the active Si photonics platform.

4.3 Device Modeling of Directly Contacted Graphene Silicon Modulators

Gradually growing data traffic has rising demands on the capacity of optical networks. Functioning as one important component in optical transceivers, modulators with low drive voltage and high speed are essential to satisfy the needs. Compatible with CMOS electronic systems, silicon photonics based on silicon on insulator (SOI) platform is acting the dominating role in producing low-cost, high-volume, and large-scale photonic integrated circuits (PICs) for on-chip components in optical networks. Silicon modulator based on the free-carrier dispersion effect is intrinsically absorptive and has the nonlinear electro-optic (EO) response to limit the performance of an ideal modulator. To integrate materials with superior properties on a silicon platform is one option for improving the performance of the building blocks in the optical communication network.

With atomic layer thickness and zero-bandgap semi-metal properties, graphene (G) is able to easily integrate on a monolithic silicon platform to improve the device performance matrix. Its tunable Fermi-level allows graphene to serve as an active layer for electro-optic modulation. As a low-loss metal layer, graphene can be placed much closer to the active layer for low-voltage operation. G has been demonstrated as an active medium for both amplitude [21]-[25] and phase modulators [26][27]. The modulation bandwidth is tested up to between a few GHz to 30 GHz, which is far below the material limitation of ~ 500 GHz bandwidth (2.2 ps response time) in G[28]. The bandwidth is limited by either RC constant or carrier transient time. Those limitations by device design are well studied in G photodetectors with G-metal contact [29]-[33]and G-Si Schottky junction [34]-[36].

In the previous work, we demonstrated that the directly contacted G-Si *p-i-n* junctions can employ both ultrafast carrier transportation in G and small RC constant in *p*-*i*-*n* junction with 1.5 ps [4][8]. In this work, following the directly contact hybrid configuration, we propose the device architecture for high-speed modulators. Different from other works on G-Si modulators using oxide capacitors based on the carrier accumulation scheme, our device utilizes directly contacted G-Si heterojunction so that the carrier density of graphene can be modulated by the silicon layer. It allows efficient carrier injection and depletion for high-speed and high efficient operation [26][27]. In the directly contacted G-Si hybrid device, the carrier transportation will be dominated by the high mobility of G, and the RC constant will be reduced by the out of plane built-in electric field between G-Si interface to improve the device speed [8]. By optimizing doping profiles in Si and graphene contact region, photonic crystal (PhC) waveguide-based Mach-Zehnder modulator (MZM) has numerically shown a very low $V_{\pi}{\cdot}L$ (1.19V·mm) and fast EO response (67 GHz) for high-speed and efficient modulator applications.

4.3.1 Device schematics

Modulation in G-Si will largely depend on refractive index change in silicon, as atomic thick G (~0.34 nm) only takes a very small proportion in the total effective index change, compared to the thickness of the Si layer (220 nm). There are three types of modulation in silicon: carrier accumulation in a MOS capacitor structure, carrier injection in a forward-biased *p*-*i*-*n* junction structure, and carrier depletion in a reverse-biased *p*-*n* junction structure [37][38]. Carrier accumulation in MOS capacitors can achieve high modulation efficiency, but the speed of the MOS-type modulator is limited by the high capacitances from a thin oxide layer. Carrier injection is the most efficient modulation mechanism, but it is hard to achieve high speed because it suffers from high junction capacitance and slow free-carrier recombination.

Carrier depletion has low modulation efficiency but can achieve high-speed performance by optimizing doping profiles to reduce the junction capacitance [38]. For the hybrid G-Si modulators, most efforts use the oxide structure of the charge accumulation scheme to enhance the efficiency while having limited speed [26]. Here, we propose direct contact G-Si modulators based on carrier injection and carrier depletion schemes to see how efficient and high speed they could achieve.

A Mach-Zehnder modulator (MZM) with two arms of the proposed G-Si structure is illustrated in Figure 4.10(a) [4][39][40]. G is integrated on one Si photonic crystal (PhC) waveguide (WG) to consist of one arm of MZM. Photonic crystal waveguides have a lattice constant of 440 nm, and different radii of 135 nm and 140 nm [41]. Each arm of MZM can be driven by electrical signals to achieve refractive index change under bias. The simulated optical mode profile of TE mode at 1550 nm is shown in Figure 4.10(b). Here, two doping profiles are proposed for graphene silicon hybrid modulators: G-Si *p*-*n* junction under reverse bias for the carrier depletion scheme and G-Si *p*-*i*-*n* junction under forward bias for the carrier injection scheme (Figure 4.10(c) and (d)). A Wider *N* region (4 μm) region makes the optical mode profile overlap with the strong built-in electric field around G and *Si/n* region to enhance the electric-optical interaction. Single-layer graphene will be transferred onto PhC WG covering *P+*, *P*, and *N* regions (Figure 4.10(b) and (c)) [8]. Also, for *p*-*i*-*n* junction, graphene covers from *P+* to the intrinsic region (width of 6 μm) for good electric-optical interaction. For the doping profile, lightly doped *P* (1×10^{18} cm^{-3}) and *N* (1×10^{18} cm^{-3}) regions in the middle to form the *p*-*n* junction (Figure 4.10(c)). High-doped regions of *P+* (5×10^{18} cm^{-3}) and *N+* (5×10^{18} cm^{-3}) are at each side of *P* and *N* region to connect heavily doped *P++* (8×10^{19} cm^{-3}) and *N++* (8×10^{19} cm^{-3}) regions which form the ohmic contact with the anode and cathode, respectively. Intrinsic region has a lightly *p* doped concentration of 10^{16} cm^{-3}. Graphene supposes to have a *p*-type doping of about 10^{12} cm^{-2}. SEM imaging showing the fabricated PhC WC is presented in Figure 4.10(e). The measured transmission spectra of PhC waveguides with different radii can be seen in Figure 4.10(f).

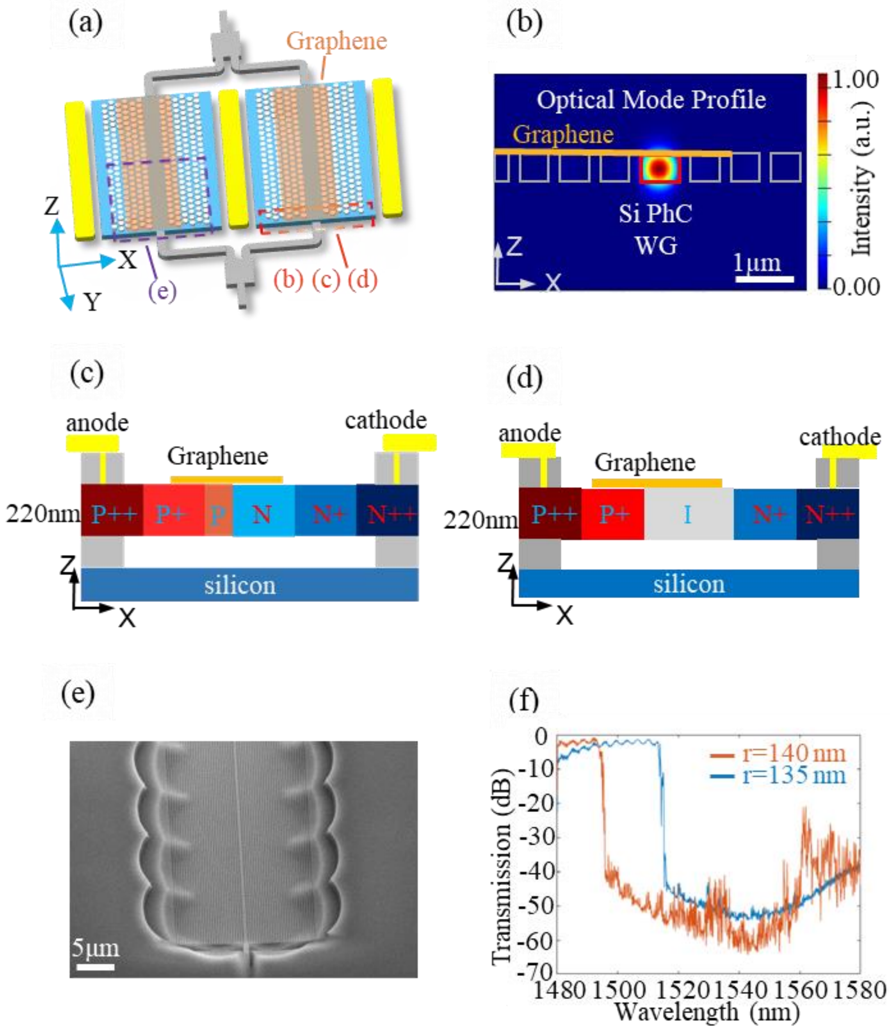

Figure 4.10 Device schematics. (a) Schematic of proposed G-Si photonic crystal waveguide (PhC WG) MZM modulators. (b) Cross-sectional optical mode profile (TE mode) of PhC WG at 1550 nm. (c) The doping profile of graphene silicon *p-n* junction modulator. (d) The doping profile of graphene silicon *p-i-n* junction modulator. (e) SEM imaging of the foundry-processed silicon PhC WG. (f) Measured transmission spectra of PhC WG after undercut. r: radii of the holes in the PhC slab [41][42].

4.3.2 Numerical simulation and calculation

To investigate the modulation efficiency of this hybrid G-Si modulator, effective index variation induced by the charge carrier density changes in both graphene and silicon under bias is numerically studied. Lumerical DEVICE is used to simulate the charge carrier dynamics in the cross-section (Figures 4.10(c) and (d)) for this hybrid junction under bias. Charge carrier concentrations are exported from the Lumerical DEVICE suite for numerical calculation and analysis.

The effective index change of the G-Si hybrid waveguide can be expressed as[43]:

$$\Delta n_{eff} = \frac{n c_0 \varepsilon_0 \int n\,|E|^2\,dx\,dy}{\int Re(E \times H^*) \cdot z \cdot dx\,dy}, \tag{4.9}$$

where n is the refractive index of the hybrid waveguide, c_0 and ε_0 denote light speed and permittivity in vacuum, and E and H represent the optical modal fields. The integral in the numerator is performed across the hybrid waveguide whereas the one in the denominator is integrated over the entire waveguide cross-section.

The total effective index change consists of both G and Si. Effective index changes in G and Si are numerically calculated separately based on the simulated carrier densities in G and Si, respectively. Then use equation (4.9) to numerically calculate the total effective index change of the hybrid G-Si waveguide.

In silicon, change of refractive index and absorption based on carrier density change can be expressed as [44][45]

$$\Delta n(1550nm) = -5.4 \times 10^{-22} \times \Delta N^{1.011} - 1.53 \times 10^{-18} \times \Delta P^{0.838} \qquad (4.10)$$

$$\Delta \alpha(1550nm) = 8.88 \times 10^{-21} \times \Delta N^{1.167} + 5.84 \times 10^{-20} \times \Delta P^{1.109} \qquad (4.11)$$

In graphene, complex refractive index (n_g) change is determined by its conductivity (σ). The conductivity is related to the Fermi level (μ_c), which is dependent on carrier density (n_s). The relationship between graphene complex refractive index (n_g), conductivity (σ), and Fermi level (μ_c) is shown in equation (4.12-4.14) [46][47].

Graphene's complex refractive index (n_g) is related to:

$$n_g = \sqrt{\varepsilon_g} = \sqrt{1 + \frac{i\sigma}{\omega t_g \varepsilon_0}}, \qquad (4.12)$$

where ω is the angular frequency, t_g is the thickness of graphene, and ε_0 is the relative permittivity in graphene.

Graphene's conductivity (σ) is expressed as:

$$\sigma(\omega) = \frac{\sigma_0}{2}\left(\tanh\left(\frac{\hbar\omega + 2\mu_c}{4k_B T}\right) + \tanh\left(\frac{\hbar\omega - 2\mu_c}{4k_B T}\right)\right) - i\frac{\sigma_0}{2\pi}\ln\left[\frac{(\hbar\omega + 2\mu_c)^2}{(\hbar\omega - 2\mu_c)^2 - 2(k_B T)^2}\right] + i\frac{4\sigma_0}{\pi}\frac{\mu_c}{\hbar\omega + i\hbar\Gamma}, \qquad (4.13)$$

where σ_0 single layer graphene universal conductivity, $\hbar$ is the reduced Planck constant, μ_c is Graphene's Fermi level, k_B is the Boltzmann constant, T is the temperature, and Γ is the scattering time.

Graphene's Fermi level (μ_c) is determined by:

$$\mu_c(n_s) = sgn(n_s)\hbar v_F \times \sqrt{\pi |n_s|}, \qquad (4.14)$$

where n_s is the carrier density in graphene, v_F is the Fermi velocity. The related parameters used in the above equations are listed in Table 4.3.

Symbol	QUANTITY	Values and unit[a]
μ_c	Fermi level of graphene	eV
n_s	carrier density in graphene	cm^{-2}
$\hbar$	reduced Planck constant	$6.58 \cdot 10^{-16}$ eV·s
v_F	Fermi velocity	10^6 m/s
σ_0	single layer graphene universal conductivity	60.8 μS
k_B	Boltzmann constant	$1.380649 \cdot 10^{-23}$ J/K
T	temperature	300 K
ω	angular frequency	Rad/s
Γ	scattering time	10 fs
n_g	refractive index of graphene	
ε_g	permittivity of graphene	F
t_g	graphene thickness	1 nm
ε_0	vacuum permittivity	$8.85 \cdot 10^{-12}$ F/m
ΔP	hole concentration change in silicon	cm^{-3}
ΔN	electron concentration change in silicon	cm^{-3}
Δn	real part of refractive index change in silicon	
$\Delta \alpha$	absorption change in silicon	dB/cm

[a] eV = electron volt, S = Simens; s = second, F= Farad.

Table 4. 3 Terms for Graphene Silicon Modulators.

4.3.2.1 Carrier depletion scheme of G-Si modulators

G-Si modulators based on carrier depletion scheme (*p-n* junction in Si, under reverse bias) are firstly investigated (Figure 4.10(c)). After being transferred to the silicon substrate, graphene is electrostatically doped [4][8]. Lateral bias across the *p-n* junction shifts G Fermi level and carrier density. Based on the simulated carrier density change under bias, G's complex refractive index is obtained by calculating G's parameters such as conductivity and Fermi level by equations (4.12-4.14) [46][47]. G's complex refractive index is shown in Figure 4.11(a). Under reverse bias, the real part of G refractive index increases with bias while the imaginary part decreases. In Si, refractive index change is induced by the carrier densities change under bias following the equations (4.10, 4.11) [44][45]. The real and imaginary parts of silicon refractive index increase with reverse bias (Figure 4.11(b)). Numerical calculation estimated that silicon dominates and contributes most which are about 99.6% to the total effective index change compared with graphene (0.29%) since the optical mode profile is mostly confined in the Si region (Figure 4.10(b)). The change of the total effective index of this hybrid structure is calculated up to the 10^{-3} scale with reverse bias (Figure 4.11(c)). The length required to achieve a π phase shift can be obtained in Figure 4.11(d). The minimum $V_{\pi}{\cdot}L$ is 2.15V·mm (2.87mm·0.75V). This is due to significant variation of carrier densities in directly contacted silicon and graphene under bias. The loss of this hybrid waveguide kept around 25.24 dB/cm at a different bias (Figure 4.11(e)). Assuming the length of each arm is 250 μm, the transmission spectra of MZM are calculated with a different reverse bias applied on one arm (Figure 4.11(f)) [48]. About 20 dB and 30 dB extinction ratios can be achieved with reverse 1V and 2V bias respectively.

In a Si *p-n* junction, a space charge region will be formed as the reverse bias is applied [37]. The width of the space charge region increases with the increasing built-in electric field induced by charge-induced doping [4]. This can reduce the equivalent capacitance of the junction component, further reducing the RC constant and increasing the EO bandwidth of the device [8]. Figure 4.12(a) is the built-in electric field along the z-direction (E_z) with lateral reverse bias. This reduces the junction capacitance and thus the RC constant. The S_{11} response has been simulated using the Advanced Design System (ADS 2012, by Keysight Technology) under different reverse biases [49]. For the G-Si heterogeneous structure, the overall 3 dB bandwidth of electrical-optical (EO) response is determined by RC constant limited bandwidth and carrier transit time limited bandwidth (equation 4.15) [50][51]:

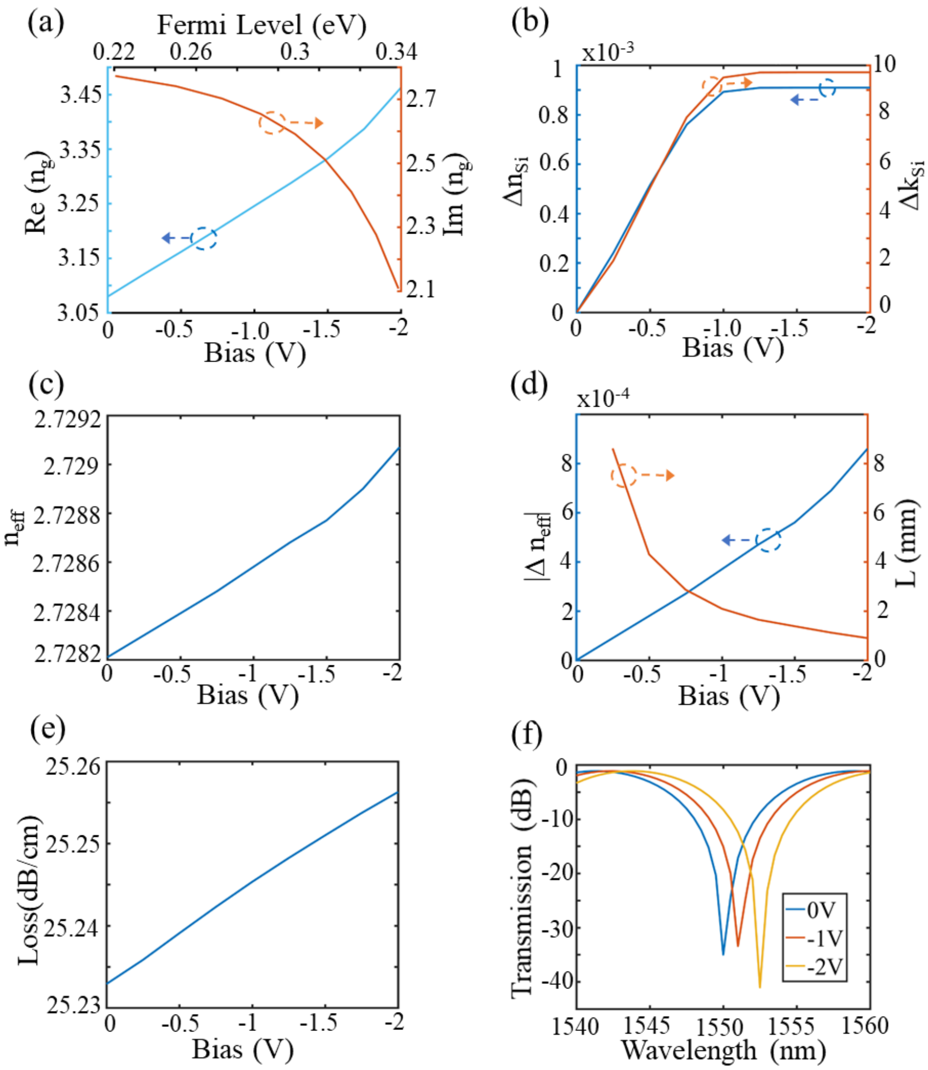

Figure 4.11 G-Si *p-n* junction modulator. (a) G Fermi level and refractive index variation under the reverse bias of 0 to -2V. (b) The real and imaginary parts of the silicon refractive index change under reverse bias from 0 to -2V. (c) Effective index variation of the hybrid structure under reverse bias from 0 to -2V. (d) Total effective index change and the length to achieve π phase shift under reserve bias from 0 to -2V. (e) Loss of the hybrid waveguide with reserve bias from 0 to -2V. (f) Transmission spectrum of driving one arm of MZM around 1550 nm under bias 0 to -2V.

$$f_{3dB} \approx \frac{1}{\sqrt{\frac{1}{f_{RC}{}^2} + \frac{1}{f_{tr}{}^2}}}, \tag{4.15}$$

where f_{RC} is the RC constant limited bandwidth which can be estimated (about 105 GHz at 0V) based on simulated RC constant from the small signal model. f_{tr} is the transit time limited bandwidth which is determined by: $f_{tr}=0.44/\tau_{tr}$, where transit time τ_{tr}= (depletion region width)/ (carrier velocity) = (5 μm)/ (10^6 m/s) =5ps (depletion width is estimated 5 μm here, carrier velocity is 10^6 m/s). As a result, the overall 3 dB bandwidth of EO response is mainly limited by carrier transit time and is about 67 GHz.

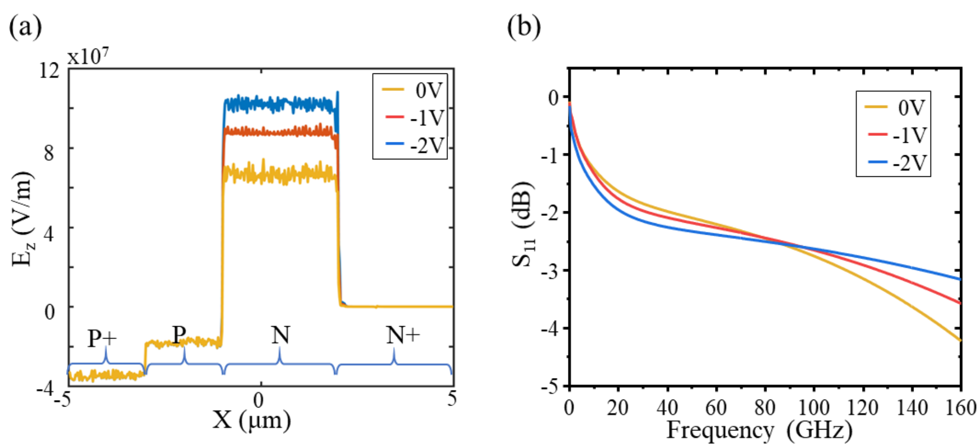

Figure 4.12 Simulated built-in electric field and reflection coefficient S_{11}. (a) E_z component of built-in electric fields at graphene layer under reverse bias for G-Si *p-n* junction modulator. (b) Simulated S_{11} response G-Si *p-n* junction modulator under bias 0 to -2V.

One concern is that the slow light effect of the photonic crystal waveguide will make a mismatch between the optical group index and microwave index to further affect the overall modulated bandwidth [52][53]. The 3dB bandwidth is estimated by: [54]

$$f_{3dB} \propto \frac{1.89c_0}{\pi|n_{\mu g} - n_{og}|L}, \tag{4.16}$$

where $n_{\mu g}$ is the microwave index, and n_{og} is the optical group index. For a short electrode (no longer than 200 μm), the velocity mismatch is less significant to affect the overall 3dB bandwidth.

4.3.2.2 Carrier injection scheme of G-Si modulators

Then, G-Si *p-i-n* modulators based on the injection scheme (under forward bias) are investigated (Figure 4.10(d)). The same method (same as the contents in Section 4.3.2.1) is used for simulating carrier density changes and calculating the refractive index change in G and Si for this hybrid structure.

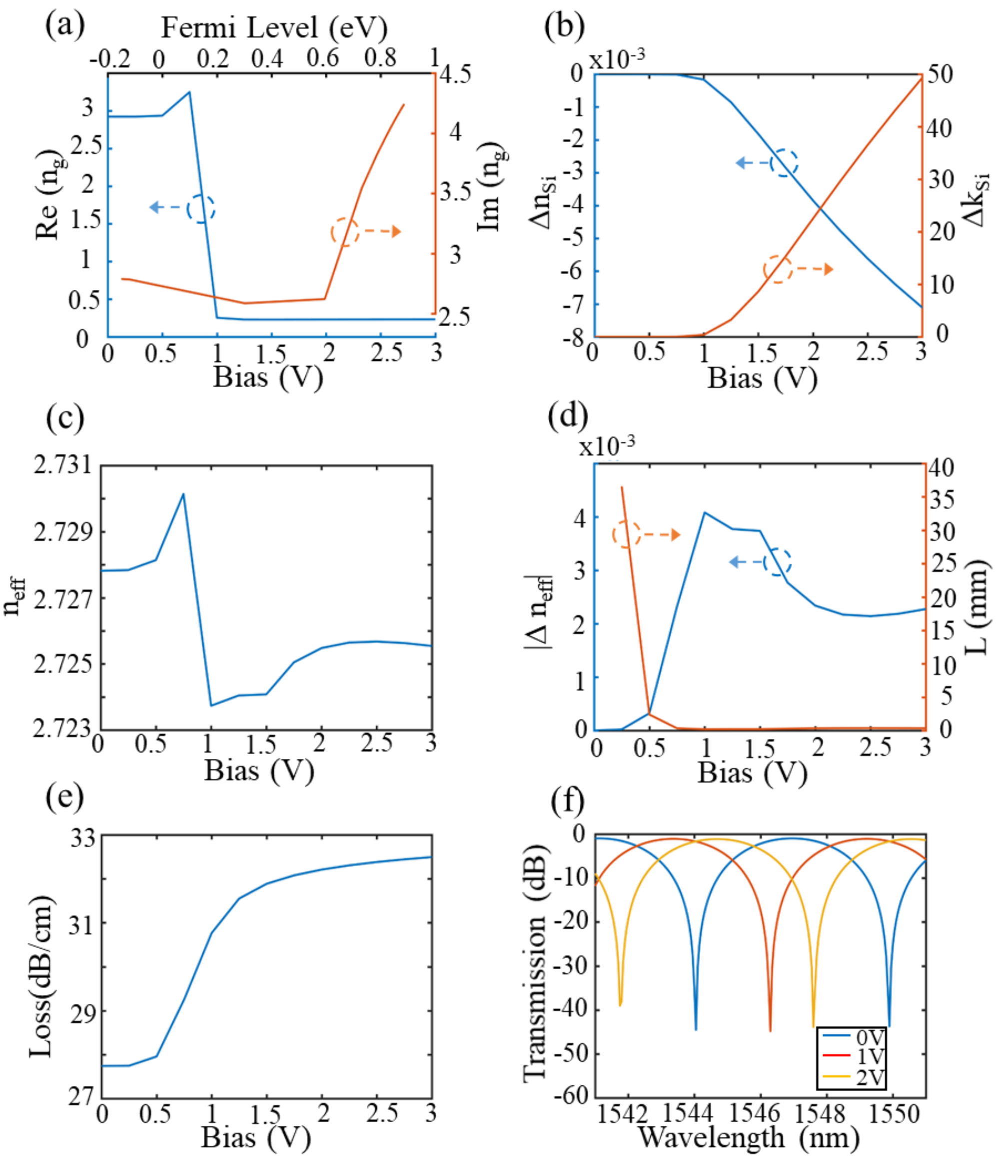

Figure 4.13 G-Si *p*-*i*-*n* junction modulator. (a) Graphene Fermi level and refractive index variation under the forward bias of 0 to 3V. (b) The real and imaginary parts of the silicon refractive index change under the forward bias of 0 to 3V. (c) Effective index variation of the hybrid structure under forward bias from 0 to 3V. (d) Total effective index change and the length to achieve π phase shift under forward bias. (e) Loss of the hybrid waveguide under forward bias from 0 to 3V. (f) Transmission spectrum of driving one arm of MZM around 1550 nm under bias 0 to 3V.

Under the forward bias, the Fermi level of graphene is shifted, and carrier density is changed. The calculated changes in G Fermi level and complex refractive index are shown in Figure 4.13(a). Under forward bias, the real part of the graphene refractive index increases then decreases as it experiences interband to intraband transition [46], while the imaginary part increases. Due to the change in graphene conductivity, the real part of the refractive index of graphene gets lower as the Fermi level increases. In silicon, the real part of the silicon refractive index decreases while the imaginary part increases with forward bias (Figure 4.13(b)). The change of the total effective index of this hybrid structure is calculated on the 10^{-3} scale with forward bias (Figure 4.13(c)). The total effective index changes on the order of magnitude of 10^{-3} showing good efficiency. Numerical calculation estimated that silicon dominates and contributes most 99.63% to the total effective index change compared with graphene (0.27%). At low bias voltage (<1V), G contributes obviously to the total effective index change, while Si takes over the role beyond 1V. The $V_{\pi}{\cdot}L$ of the hybrid device is derived to be 1.19V·mm at 0.5V (2.397mm·0.5V) (Figure 4.13(d)). This is due to significant variation of carrier densities in directly contacted silicon and graphene under bias. Along with the phase modulation, ~ 4 dB/cm incremental loss is observed at the reverse bias set beyond 1 V (Figure 4.13(e)). Assuming the length of the electro-optical interaction of each arm is 250 μm, the transmission spectra of the MZM with G-Si *p-i-n* junction phase modulators are calculated with different forward biases (Figure 4.13(f)). The spectrum shift is about 1.5 nm per volt.

Simulated Built-in electric field component E_z can be seen in Figure 4.14(a). By using the same method as the G-Si *p-n* junction, the overall 3dB bandwidth of the

EO response can be simulated. RC constant limited bandwidth can be obtained (about 80 GHz at 0V) from simulated S_{11} in Figure 4.14(b). The carrier transit time is about 5 ps. The estimated EO bandwidth (limited by the RC constant) is about 59 GHz.

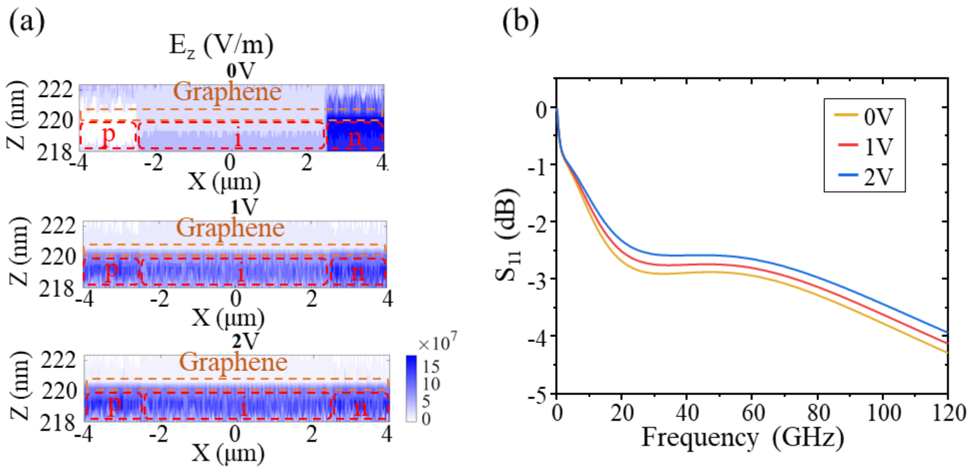

Figure 4.14 Simulated built-in electric field and S11 for G-Si *p-i-n* junction modulator. (a) E_z component of built-in electric fields at graphene silicon interface under forward bias for G-Si *p-i-n* junction modulator. (b) Simulated S_{11} response G-Si *p-i-n* junction modulator under bias 0 to 2V.

4.3.3 Summary

In this work, directly contacted graphene silicon modulators are numerically demonstrated. By designing the electrical doping profile and co-optical designing graphene integrated photonic crystal waveguide, the hybrid device is able to achieve a bandwidth of EO response of at least 59 GHz and a very low $V_\pi \cdot L$ of 1.19 V·mm while suffering from considerable loss of over 25dB/cm. This can be compromised by designing the proper length of the MZM arm for electrical-optical interaction to achieve desired phase shift without too much loss. Simulation and numerical results of the proposed devices based on direct contact G-Si *p-i-n*/*p-n* configuration show great potential for high-speed and efficiency modulator applications.

4.4 Summary

In this Chapter, the voltage-dependent variation of multi-junction in the hybrid Graphene-Si *p*-*i*-*n* junction is investigated. The G-Si heterojunctions and G homojunctions are analyzed by fitting the small-signal model to the broadband RF response. The results are compared to the simulated built-in electric field distribution to analyze the junction variation and potential RC constant. It is shown that the forward bias through Si *p*-*i*-*n* junction substrate can alter the doping levels of G and the vertical built-in electric field on the G-Si interface. The potential RC constant of the hybrid device could be 1.5 ps. This result is useful for designing a hybrid device with RC constant limited bottleneck to achieve a high-speed response of integrated optoelectronic devices based on the Si photonic platform.

Following the directly contacted G-Si hybrid device configuration, the device architecture of G-Si modulators is numerically investigated. This device configuration enables the modulation of graphene's carrier density by the silicon layer. It also utilizes both ultrafast carrier transportation in G and reduced RC constant by the out-of-plane built-in electric field between the G-Si interface for highly efficient and high-speed operation. By optimizing doping profiles in Si and graphene contact region, photonic crystal (PhC) waveguide-based Mach-Zehnder modulator (MZM) numerically shows a very low $V_{\pi}{\cdot}L$ of 1.19V·mm and fast EO response (67 GHz) for efficient and high-speed modulator applications.

REFERENCES

[1] J. Wu, et al, Two-Dimensional Materials for Integrated Photonics: Recent Advances and Future Challenges, Small Sci., 1, 2000053, 2021

[2] F. Xia, et al, Two-dimensional material nanophotonics. Nature Photonics, 8, 899–907, 2014

[3] M. Jin, et al, Silicon-Based Graphene Electro-Optical Modulators, Photonics, 9, 82, 2022

[4] T. Li, et al, Spatially controlled electrostatic doping in graphene *p-i-n* junction for hybrid silicon photodiode, npj 2D Materials and Applications, 2, 36, 2018

[5] T. Li, et al, Hybrid Graphene Tunneling Photoconductor with Interface Engineering towards Fast Photoresponse and High Responsivity, npj 2D Materials and Applications, 1, 19, 2017

[6] C. Chen, et al, Gate Tunable Graphene-Silicon Ohmic/Schottky Contacts. *Applied Physics Letters*, *101*, 223113-223113, 2012

[7] X. An, et al, Tunable Graphene–Silicon Heterojunctions for Ultrasensitive Photodetection, *Nano Letters*, *13*, 909-916, 2013

[8] D. Mao, et al, Bandwidth limitation of directly contacted graphene–silicon optoelectronics, ACS Applied Electronic Materials, 1, 2, 172–178, 2019.

[9] L. Gu, High-speed Silicon Photonic Crystal Waveguide Modulator for Low Voltage Operation. Appl. Phys. Lett. 90, 071105−071105, 2007

[10] A. Das, et al, Monitoring Dopants by Raman Scattering in an Electrochemically Top-Gated Graphene Transistor, Nature Nanotechnology, 3, 210-215, 2008

[11] S. Manipatruni, et al, Ultra-Low Voltage, Ultra-Small Mode Volume Silicon Microring Modulator, *Optics Express*, *18*, 18235-18242, 2010

[12] R. Wu, et al, Compact Models for Carrier-Injection Silicon Microring Modulators, *Optics Express*, *23*, 15545-15554, 2015

[13] Y.Yao, et al, Broad Electrical Tuning of Graphene-Loaded Plasmonic Antennas. *ACS Nano*, *13*, 1257−1264, 2013

[14] J. Kang, et al, On-Chip Intercalated-Graphene Inductors for Next-Generation Radio Frequency Electronics. *Nature Electronics*, *1*, 46–51, 2018

[15] D. Dai, et al, Resonant Normal-Incidence Separate-Absorption-Charge-Multiplication Ge/Si Avalanche Photodiodes. *Optics Express*, *17*, 16549-16557, 2009

[16] http://www.keysight.com/en/pc-1297113/advanced-design-system-ads?cc=US&lc=eng

[17] https://optics.ansys.com/hc/en-us/articles/360034917693-CHARGE

[18] H. Yoon, et al, Measurement of Collective Dynamical Mass of Dirac Fermions in Graphene, Nature Nanotechnology, 9, 594–599, 2014

[19] K. Bolotin, et al, Ultrahigh Electron Mobility in Suspended Graphene, Solid State Communications, 146, 351-355, 2008

[20] E. H. Hwang, et al, Carrier Transport in Two-Dimensional Graphene Layers, Physical Review Letters, 98, 186806, 2007

[21] C. Phare, et al, Graphene Electro-Optic Modulator with 30 GHz Bandwidth, *Nature Photonics*, 9, 511–515, 2015

[22] M. Liu, et al, A Graphene-Based Broadband Optical Modulator, *Nature*, 474, 64–67, 2011.

[23] Y. Ding, et al, Effective Electro-Optical Modulation with High Extinction Ratio by a Graphene–Silicon Microring Resonator, Nano Letters, 15, (7), 4393-4400, 2015.

[24] H. Zhou, et al, Error-free data transmission through fast broadband all-optical modulation in graphene–silicon optoelectronics, Applied Physics Letters, 116, 221106, 2020.

[25] M. Ono, et al, Ultrafast and energy-efficient all-optical switching with graphene-loaded deep-subwavelength plasmonic waveguides, Nature Photonics, 14(1), 37-43, 2019.

[26] V. Sorianello, et al, Graphene–Silicon Phase Modulators with Gigahertz Bandwidth, *Nature Photonics*, 2, 40–44, 2018.

[27] M. Mohsin, et al, Experimental verification of electro-refractive phase modulation in graphene, Scientific reports, 5, 10967, 2015.

[28] W. Li, et al, Ultrafast all-optical graphene modulator, *Nano letters*, 14(2), 955-959, 2014.

[29] R. Shiue, et al, High-Responsivity Graphene−Boron Nitride Photodetector and Autocorrelator in a Silicon Photonic Integrated Circuit, Nano Letters, 15, 7288−7293, 2015.

[30] D. Schall, et al, 50 GBit/s Photodetectors Based on Wafer-Scale Graphene for Integrated Silicon Photonic Communication Systems. *ACS Photonics*, 1, 781–784, 2014.

[31] P. Ma, et al, Plasmonically Enhanced Graphene Photodetector Featuring 100 Gbit/s Data Reception, High Responsivity, and Compact Size. ACS Photonics, 6(1), 154–161, 2019.

[32] D. Schall, et al, Graphene Photodetectors with a Bandwidth >76 GHz Fabricated in a 6″ Wafer Process Line, Journal of Physics D: Applied Physics, 50, 124004, 2017.

[33] J. Guo, et al, High-performance silicon−graphene hybrid plasmonic waveguide photodetectors beyond 1.55 μm, Light: Science & Applications, 9, 29, 2020.

[34] X. Wang, et al, High-Responsivity Graphene/Silicon-Heterostructure Waveguide Photodetectors. Nature Photonics, 7, 888–891, 2013.

[35] X. An, et al. Tunable Graphene-Silicon Heterojunctions for Ultrasensitive Photodetection, *Nano Letters*, 13, 909–916, 2013

[36] S. Schuler, et al. Controlled Generation of a *p-n* Junction in a Waveguide Integrated Graphene Photodetector. *Nano Letters*, 16, 7107–7112, 2016

[37] G. Reed, et al, Silicon optical modulators, *Nature Photonics*, 4, 518–526, 2010

[38] P. Dong, et al, High-speed low-voltage single-drive push-pull silicon Mach-Zehnder modulators, *Optics Express*, 20, 6, 6163-6169, 2012

[39] H. Nguyen, et al, Compact and fast photonic crystal silicon optical modulators, *Optics Express*, 20(20), 22465-22474, 2012

[40] H. Zhou, et al, Enhanced photoresponsivity in graphene-silicon slow-light photonic crystal waveguides, *Applied Physics Letters*, 108, 111106, 2016

[41] F. Wang, et al. Low-loss photonic crystal platform by foundry processing, in *Conference on Lasers and Electro-Optics*, JTu2D.2, 2020

[42] Y. Xiao, et al, Scalable photonic crystal waveguides with 2 dB component loss, Photonic Technology Letters, 34, 637-640, 2022.

[43] S. Deckoff-Jones, et al, Tellurene: A Multifunctional Material for Midinfrared Optoelectronics, ACS Photonics, 6, 1632−1638, 2019

[44] R. Soref, et al, Electrooptical effects in silicon, IEEE J. Quantum Electron., 23(1), 123–129, 1987

[45] M. Nedeljkovic, et al, "Free-Carrier Electrorefraction and Electroabsorption Modulation Predictions for Silicon Over the 1–14- μm Infrared Wavelength Range," *IEEE Photonics Journal*, vol. 3, no. 6, pp. 1171-1180, 2011

[46] K. Ooi, et al, Nonlinear graphene plasmonics, *Proceedings of the Royal Society A*, 473, 20170433, 2007

[47] M. Romagnoli, et al, Graphene-Based Integrated Photonics for Next-Generation Datacom and Telecom, *Nature Reviews Materials*, 3, 392–414, 2018

[48] R. Hui, et al, Fiber Optic Measurement Techniques, Academic Press, 1st ed., Chap. 2, 2009

[49] B. Lee, et al, High performance integrated graphene electro-optic modulator at cryogenic temperature, Nanophotonics, 10(1), 99-104, 2021

[50] B. Saleh, et al, Fundamentals of Photonics, 2nd ed., Wiley-Interscience, 2007

[51] J. Liu, Photonic Devices, 1st ed., Cambridge University Press, 2010

[52] A. Mercante, et al, Thin film lithium niobate electro-optic modulator with terahertz operating bandwidth, Opt. Express, 26(11), 14810-14816, 2018

[53] A. Mercante, et al, 110 GHz CMOS compatible thin film LiNbO3 modulator on silicon, Opt. Express, 24(14), 15590-15595, 2016

[54] D. Patel, Design, analysis, and performance of a silicon photonic traveling wave Mach-Zehnder modulator, Thesis, McGill Unviersity, 2015

[55] Y. Hinakura, et al, Wide Spectral Characteristics of Si Photonic Crystal Mach-Zehnder Modulator Fabricated by Complementary Metal-Oxide-Semiconductor Process, Photonics, 3, 2(17), 2016

Chapter 5

PHOTOREFRACTIVE EFFECT IN TELLURIUM THIN FILM

5.1 Introduction

Nanofabrication-induced variation leads to random resonance deviation of silicon (Si) microring resonators (MRRs), limiting the applications of modulators and lasers in photonic integrated circuits. Conventional tuning methods such as using phase change materials, material strain, thermal tuning, and carrier injection have the limits of extra loss, inefficient tuning, and large device footprint, etc [1]-[4]. With unique properties such as potential photocatalytic reactions, 2D materials can be easily integrated into CMOS-compatible silicon platforms and are able to tune the optical response.

Group VI element Tellurium (Te) is one kind of 2D material possessing a one-dimensional chiral atomic structure and stable properties under room temperature [5]-[8][6]. It has arisen research interests in electronic, optoelectronic to piezoelectric applications. Especially, the decreased layer numbers and van der Waals structure could change the bandgap and enable novel optical nonlinear responses. An optical nonlinear response such as Second Harmonic Generation (SHG) has been observed on Te nanowires (NW), showing a giant response compared with NWs of other materials[9][10]. Besides that, light-induced oxidation of Te thin film hasn't been studied, which may have potential applications in catalysis and oxidation material-related applications.

In this work, we studied the optical nonlinear response of tellurium by integrating the material on a foundry-fabricated silicon platform. Solution-synthesized tellurium flakes were transferred to a silicon ring resonator to utilize the low loss and high quality (Q) factor device platform [12][13]. As the excited optical power increases, the resonance shifts of this hybrid structure were characterized and compared with monolithic silicon devices without Te. We observed the photo-refractive response of this hybrid structure which makes the resonance have blue shifts without extra loss. The Raman spectra show that the photo-oxidation induced Te transiting to TeO_2 which has a smaller refractive index for the resonance blue shift. The degree of resonance shifts and intrinsic quality factor (Q_{in}) change with Te are dependent on material thickness and covering length on the device. The material may play an important role in future all-optical resonance trimming applications of MRRs [11] [17][22].

5.2 The photorefractive effect from Tellurium thin film

5.2.1 Post-processing for the silicon devices

To probe the nonlinearity, a directly contacted hybrid device (Te-silicon) structure is proposed to utilize the low loss and high Q silicon platform. To have the directly contacted structure, a post-processing step to remove the top oxide layer is needed for silicon chips (Figure 5.1) [12]. Silicon photonics chips are fabricated by AIM photonics. Firstly, the top oxide layer is removed through wet etching by using buffered oxide etching (BOE 1:6) at a rate of about 160 nm/min. Then, the photoresist (AZ1512) is spin-coated onto the sample, followed by laser writing to open a window above the ring region. After the laser writing, the sample is dipped into BOE for a few minutes to remove the remaining top oxide layer and reveal the silicon waveguide layer on the surface. Finally, the remaining photo-resist is stripped.

Post-Processing procedures

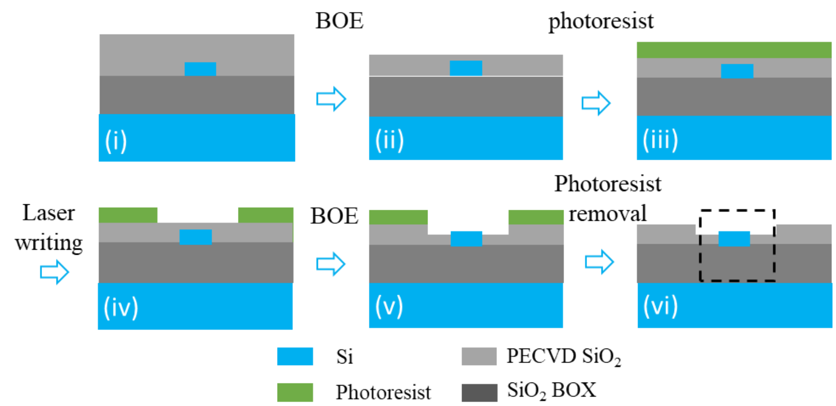

Figure 5.1 Post-processing schematics (top oxide removal) of silicon passive chips (cross-sectional view).

Silicon ring resonators after post-processing could have low loss and high Q factors. After top oxide removal, SEM images show revealed a silicon layer of ring resonator (Figure 5.2).

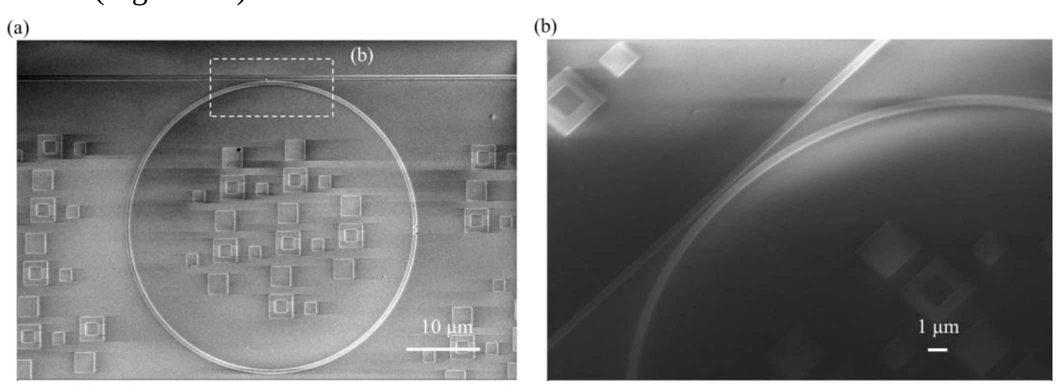

Figure 5.2 SEM images of silicon resonators after top oxide removal.

5.2.2 Photorefractive Response of a Te-Si Hybrid Device

The transfer process can be seen in section 2.2.2.1. The power-dependent nonlinear optical response from Te thin film is measured through the high Q (~10^5) micro-ring resonators (MRRs) (Figure 5.3). The tunable Continuous Wave (c.w.) laser is coupled into the MRRs through fibers, a polarization controller, a grating coupler, and a bus waveguide. The insertion loss of each component (less than -10 dBm) is considered to estimate the effective power coupled into the MRR (P_{in}). As the input power increases, only the resonance of the ring covered by Te flake exhibits a nonlinear response of blue shifts (Figure 5.3) [21]. Two hybrid devices with different Te thicknesses and covering lengths are presented in Figure 5.3. The silicon ring covered by a shorter Te flake (1.6 μm) shows the resonance shifts ($\Delta\lambda$) up to 66 pm as P_{in} increases from -13 dBm to -10 dBm (Figure 5.3(a)). The silicon ring covered by a long Te flake (15 μm) shows the resonance shifts up to 240 pm as P_{in} increases from -15 dBm to -9 dBm (Figure 5.3(b)). For these two hybrid devices, the Quality factors (Q), the resonance shifts ($\Delta\lambda$), and related effective index change (Δn_{eff} (Te-Si)) of the Te-Si hybrid device under each power level are extracted in Table 5.1. Lumerical Mode simulation was conducted to calculate the refractive index change in Te (Δn (Te)) after increasing the input power to -10 dBm. It showed the refractive index of Te decreased by about 0.2 after increasing to the highest power (Figure 5.4), leading to the total effective index of Te-Si reduction and resonance peak blue shift. The same phenomenon was observed from Lithium Niobate cavities [17]-[20][22].

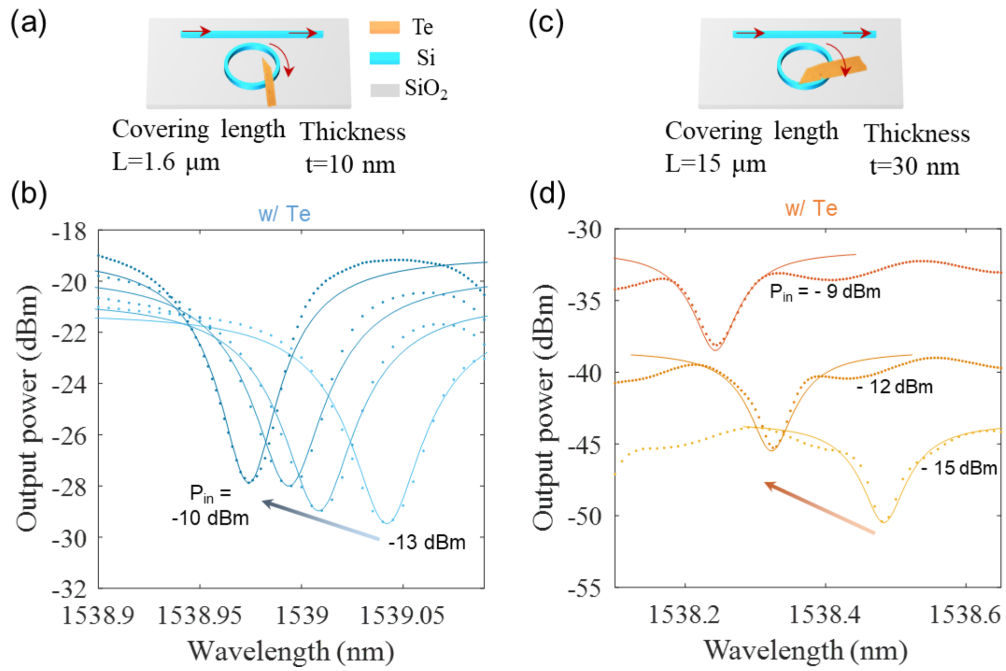

Figure 5.3 Photorefractive effect of Te thin films. (a) Schematics of one thin Te flake (thickness=10 nm, covering length=1.6 μm) directly integrated on one silicon ring resonator. (b) Measured and fitted nonlinear Photorefractive response for the hybrid device under different power levels. (c) Schematics of one Te flake with different thicknesses and covering length (thickness=30 nm, covering length=15 μm) on one silicon ring resonator. (d) Measured and fitted resonance transmission spectra for the hybrid ring resonator with the Te flake.

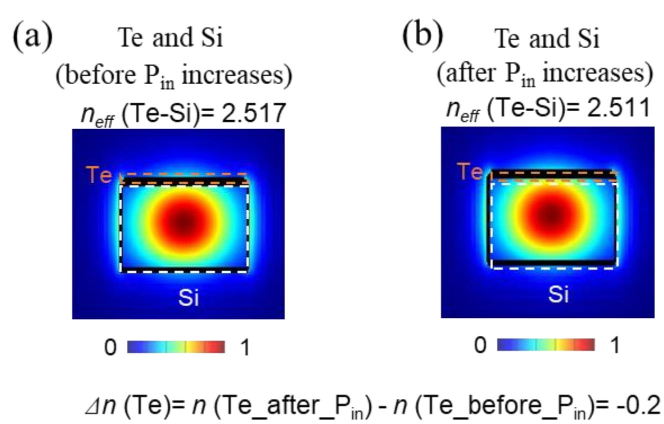

Figure 5.4 Simulation of (a) Te and Si hybrid waveguide before increasing input power P_{in}, and (b) Effective index of Te and Si hybrid waveguide after increasing input power P_{in}.

	w Te (10 nm thick)			
P_{in} (dBm)	-13	-12	-11	-10
Q_{in} (k)	67.7	67.7	67.7	76.3
Q_c (k)	30.0	30.0	30.0	35.9
Q_t (k)	20.8	20.8	20.8	24.4
$\Delta\lambda$ (pm)	0	-30	-45	-66
Δn_{eff} (Te-Si)	0	-3e-3	-4.5e-3	-6.6e-3
Δn (Te)	0			-0.2

	w Te (30 nm thick)		
P_{in} (dBm)	-15	-12	-9
Q_{in} (k)	46.3	46.3	46.3
Q_c (k)	17.7	17.7	17.7
Q_t (k)	12.8	12.8	12.8
$\Delta\lambda$ (pm)	0	-160	-240
Δn_{eff} (Te-Si)	0	-2.4e-3	-3.6e-3
Δn (Te)	0		-0.2

Table 5. 4 Resonance shifts ($\Delta\lambda$), Q factors (intrinsic Q_{in}, coupling Q_c, total Q_t) and effective index change (Δn_{eff} (Te-Si)) in the Te-Si waveguide, and effective index change in Te under different input powers for two devices in Figure 5.3. Negative signs in $\Delta\lambda$ and Δn_{eff} indicate wavelength blue shift (towards to shorter wavelength) and reduced effective index.

The curve fitting to extract Δn_{eff} is from transmission spectra which is given by [23]:

$$T = \frac{\left|\gamma - a * e^{-j\theta}\right|^2}{\left|1 - a * \gamma * e^{-j\theta}\right|^2}, \tag{5.1}$$

where γ is the transmission factor of the ring resonator, α is the linear loss of the ring, the phase $\theta = \frac{2\pi}{\lambda} n_{eff} L$, and L is the effective length.

In this case, the phase is contributed both from the Si waveguide and Te-covered Si waveguide [23]:

$$\theta = \frac{2\pi}{\lambda} n_{eff\_Si} L + \frac{2\pi}{\lambda} n_{eff_{Te-Si}}(I) L_{Te}, \tag{5.2}$$

where L_{Te} is the covering length of the Te flake, L is the perimeter of the Si ring, n_{eff_Si} is the effective index of the Silicon waveguide, $n_{eff\_Te\text{-}Si}(I)$ is the power-dependent effective index of the Te-Si waveguide.

Table 5.1 summarizes the resonance shift ($\Delta\lambda$) in wavelength under increasing power levels, for two hybrid devices with varying Te geometries. The coupled mode theory (CMT) model is used to extract the exact intrinsic (Q_{in}), coupled (Q_c), and total quality factors ($1/Q_t = 1/Q_c + 1/Q_{in}$) from the nonlinear transmission spectra (dashed curves in Figure 5.3) [14]-[16]. Q_{in} is sensitive to the change of extinction coefficient, as well as nonlinear absorptions (such as two-photon absorption, and free carrier absorption). Q_c is fixed by the geometry. Even with significant resonance shifts up to one FWHM, no additional/nonlinear absorption is reflected from that extracted Q, indicating the purely dispersive nonlinear response in Te. Te flakes with longer covering lengths can have larger wavelength shifts. The wavelength shift ($\Delta\lambda$) is proportional to both the covering length (L) and effective index change (Δn_{eff}) of the hybrid device with corresponding Te covering length [23]. In order to exclude the factor of covering length, effective index change (Δn_{eff}) was extracted considering the effect of covering length (Δn_{eff}) for further analysis based on fitting results. It reveals that nonlinear power-dependent effective index change (Δn_{eff}) of the Photorefractive (PR) effect [22].

For the hybrid device in Figure 5.3(a), the optical response was characterized by the increasing input power from -13 to -10 dBm and then decreased to -14 dBm

(Figure 5.5). Results show that the response is non-volatile. Reduction of input power to a lower level (-14dBm) comparing the original power level (-13dBm) doesn't make the response go back to the original state. Material properties have been changed. Micro-Raman spectrum is used to verify the material change in Section 5.2.4.

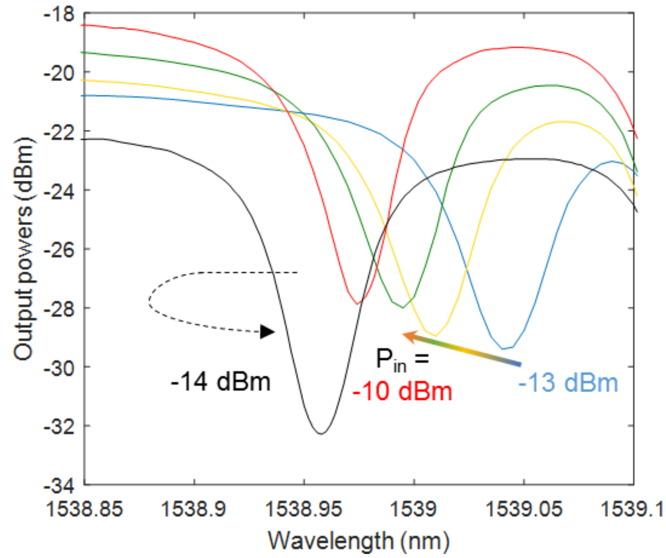

Figure 5.5 Non-volatile optical response of Te-Si hybrid device in Figure 5.3(a) under increasing input power P_{in} from -13 to -10 dBm, then decreased to -14 dBm.

5.2.3 Thickness-dependent photorefractive response

Power-dependent effective index change (Δn_{eff}) for two hybrid devices with different material thicknesses is presented in (Figure 5.6). Under the same power, the thinner Te flake exhibits a stronger Photorefractive effect.

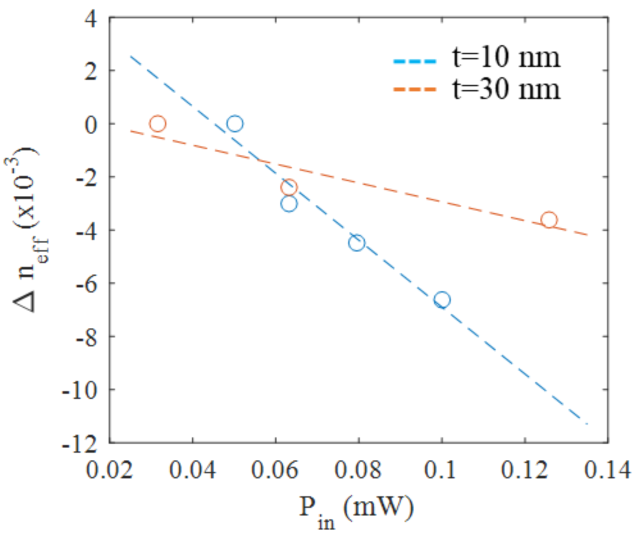

Figure 5.6 Power-dependent effective index change (Δn_{eff}) of the two hybrid devices with different Te thicknesses. The extracted effective index change has already considered the impact of covering length on the phase shift. Circles are experimental data and dashed lines are curve-fitting results for the two Te flakes.

5.2.4 Material characterization for the PR process

To study the mechanism of material change leading to the resonance blue shift in Figure 5.3, non-invasive Raman spectra were conducted to probe the laser-irradiated region of Tellurium on Si substrate (Figure 5.7 (a)). The acquisition time of 5 minutes was set for the Raman characterization. Raman spectra show not only the original peaks E_1, E_2, and A_1 of as-synthesized Te, but also peaks at 432 cm^{-1} and 670 cm^{-1} with a bump in the lower wavenumber below 100 cm^{-1} (Figure 5.7 (b)). This observation is consistent with the work reported in the literature, indicating that the Te is being oxidized to glassy-TeO_2 [26][27] (Figure 5.7 (c)). This result shows that the Te flake was partially oxidized after laser irradiation, partially transiting to TeO_2 [24]. As the glass-TeO_2 (n~2.2) has a lower refractive index than Te (n~4.7 at 1550nm), after transiting to TeO_2, the total effective index of Te-Si hybrid device decreased and led to the resonance blue shift [25]. As the thinner layer of Te is much easier to be oxidized, the oxidized proportion should be higher than the thick film, leading to a large refractive index change in Figure 5.3.

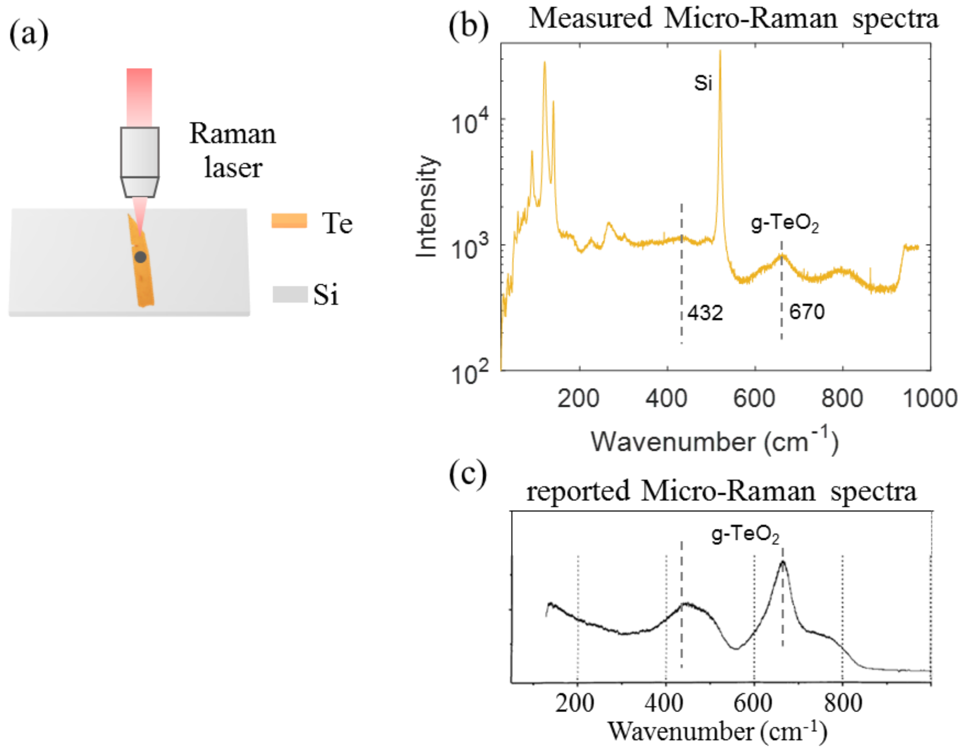

Figure 5.7 Laser irradiated Te oxidization. (a) Schematics of Raman laser irradiated Te thin film. (b) Measured Raman spectra of Te flake after 5 mins' laser irradiation. (c) Reported Raman spectra of laser irradiated Te flake after 5 mins [26][27].

5.3 Intrinsic loss induced by Tellurium thin film

The linear responses of hybrid MRRs are also analyzed. After transferring the Te flake with different covering lengths, the Intrinsic Quality factor Q_{in} has degraded for different levels. Intrinsic Quality factors are extracted based on transmission spectra for three rings without (wo Te) and with different Te (w Te) covering lengths

(Figure 5.8). And the corresponding change of intrinsic loss rate ($\Delta\gamma_{in}$) without (wo Te) and with Te (w Te) flakes for the hybrid devices are compared.

The intrinsic loss rate (γ_{in}) relating to material absorption and scattering loss is inversely proportional to Q_{in} and can be derived as:

$$\gamma_{in} = \frac{\omega_0}{Q_{in}}, \tag{5.3}$$

where ω_0 is the angular frequency of the resonance.

After transferring the Te flake to the Si ring resonator, Q_{in} degraded as more intrinsic loss is induced by the Te flake. The increasing intrinsic loss rate after transferring Te can be defined as:

$$\Delta\gamma_{in} = \gamma_{in}(w_{Te}) - \gamma_{in}(wo_{Te}), \tag{5.4}$$

where the term γ_{in} (w_Te) indicates the intrinsic loss rate after transferring the Te flake, and the term γ_{in} (wo_Te) indicates the intrinsic loss rate before transferring the Te flake.

After transferring the Te flake, the intrinsic loss rate increases (Figure 5.8). And the Te with a longer covering length has a larger increase in the intrinsic loss rate, caused by more material absorption and defect states of the hybrid device.

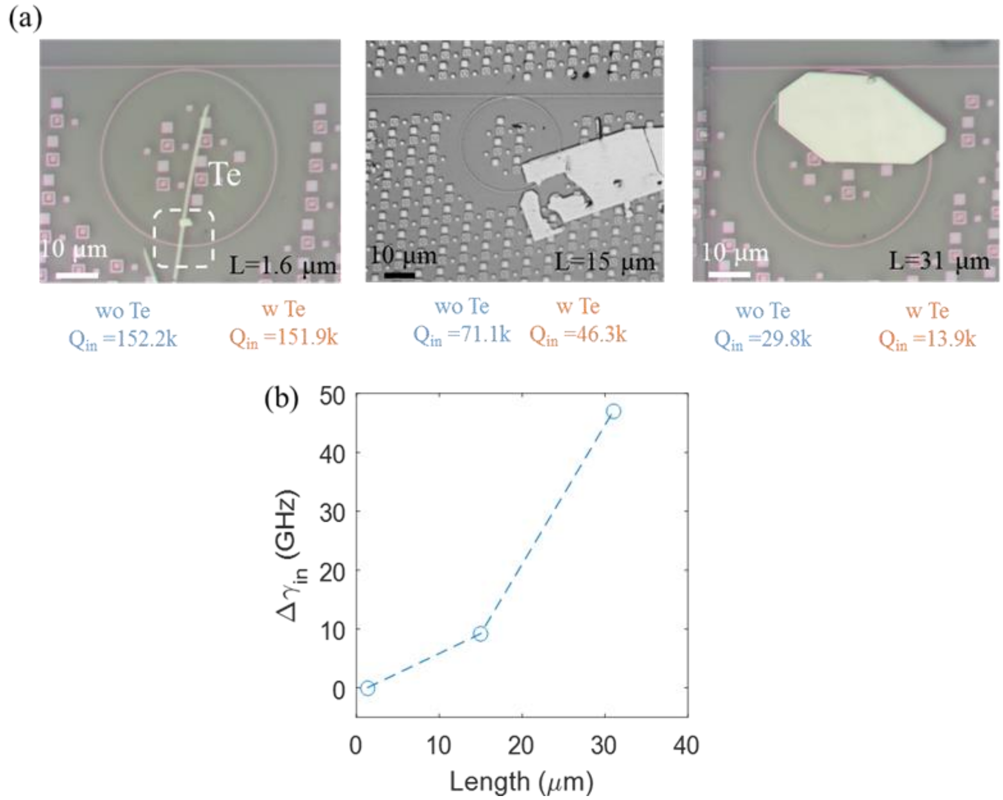

Figure 5.8 (a) Intrinsic quality factor (Q_{in}) change of three-ring resonators without and with Te thin film of different coverage lengths (L). (b) Extracted total intrinsic loss change ($\Delta\gamma_{in}$) introduced by Te with the different covering lengths for three MRRs.

5.4 Summary

In this work, we report the photorefractive response from Te flakes which can be used for resonance trimming of a Si MRR. The power-dependent and refractive index change in the 2D Te is characterized by the foundry-manufactured high Q MRR defined in the substrate. Blue-shifted resonance is associated with partial photo-oxidation of Te to TeO_2 in a hybrid device under optical excitation, and the estimated refractive index change is near -0.2 without any nonlinear loss. The resonance trimming efficiency is higher in thinner 2D-Te flakes since a thinner layer of Te is easier to be oxidized. Compared with other resonance trimming methods [28]-[31], this scheme is power efficient, highly efficient in tuning, and has a small device footprint. Given the stability and nonvolatility of the refractive index change, the Te integration in integrated photonics may pave the way for resonance trimming required for quantum optics applications.

REFERENCES

[1] C. Ríos, M. Stegmaier, P. Hosseini, D. Wang, T. Scherer, C.D. Wright, H. Bhaskaran, W. Pernice, Integrated all-photonic non-volatile multi-level memory. Nature photonics 9, 11, 725-732, 2015

[2] C. Castellan, et al, Tuning the strain-induced resonance shift in silicon racetrack resonators by their orientation. Optics Express 26(4), 4204-4218, 2018

[3] Y. Xie, et al, Thermally-Reconfigurable Silicon Photonic Devices and Circuits, IEEE Journal of Selected Topics in Quantum Electronics, 26, 5, 1-20, 3600220, 2020

[4] Q. Xu, S. Manipatruni, B. Schmidt, J. Shakya, M. Lipson, "12.5 Gbit/s carrier-injection-based silicon micro-ring silicon modulators." Optics Express 15(2) 430-436, 2007

[5] G. Qiu, et al, The resurrection of tellurium as an elemental two-dimensional semiconductor, npj 2D Materials and Applications, 6(17), 1-10, 2022

[6] Y. Wang, et al, Field-effect transistors made from solution-grown two-dimensional tellurene, Nat. Electronics, 1, 228–236, 2018

[7] Y. Xiao, et al, Scalable photonic crystal waveguides with 2 dB component loss, Photonic Technology Letters, 34, 637-640, 2022.

[8] Y.Wang, et al, Data-driven and probabilistic learning of the process-structure-property relationship in solution-grown tellurene for optimized nanomanufacturing of high-performance nanoelectronics, Nano Energy, 57, 480–491, 2019

[9] L. Wu, et al, 2D Tellurium Based High-Performance All-Optical Nonlinear Photonic Devices, Adv. Funct. Mater., 29, 1806346, 2019

[10] X. Gan, et al, Giant and Anisotropic Nonlinear Optical Responses of 1D van der Waals Material Tellurium, Adv. Optical Mater., 8, 2001273, 2020

[11] L. Thiel, et al, Precise electron beam-based target-wavelength trimming for frequency conversion in integrated photonic resonators, Optics Express, 30, 5, 6921-6933, 2022

[12] F. Wang, et al, Controlling Microring Resonator Extinction Ratio via Metal-Halide Perovskite Nonlinearity, Adv. Optical Mater., 12, 2100783, 2021

[13] Y. Xiao, et al, Scalable photonic crystal waveguides with 2 dB component loss, Photonic Technology Letters, 34, 637-640, 2022

[14] M. Borselli, et al, Beyond the Rayleigh scattering limit in high-Q silicon microdisks: theory and experiment, Opt. Express, 13, 1515-1530, 2005

[15] T. Ling, et al, Fabrication and characterization of high Q polymer micro-ring resonator and its application as a sensitive ultrasonic detector, Opt. Express, 19, 861-869, 2011

[16] M. Gao, et al, Probing material absorption and optical nonlinearity of integrated photonic materials, Nat. Commun., 13, 3323, 2022

[17] X. Sun, et al, Nonlinear optical oscillation dynamics in high-Q lithium niobate microresonators, Opt. Express, 25, 13504–13516, 2017

[18] A. Savchenkov, et al, Enhancement of photorefraction in whispering gallery mode resonators, Physical Review B, 74, 245119, 2006

[19] Z. Lin, et al, Turnkey generation of Kerr soliton microcombs on thin-film lithium niobate on insulator microresonators powered by the photorefractive effect, Opt. Express, 29, 42932-42944, 2021

[20] Y. Xu, et al, Photorefraction-induced Bragg scattering in cryogenic lithium niobate ring resonators, Opt. Letters, 46, 432-435, 2021

[21] Y. Xiao, et al, "Photo-refractive Switching of Micro-ring Resonators via few-layer Tellurium", SF2O.2 CLEO: Science and Innovations, 2022

[22] P. Günter, et al, Photorefractive materials and their applications 1, Basic effects, Springer-Verlag, 2006.

[23] I. Datta, et al, Low-loss composite photonic platform based on 2D semiconductor monolayers, Nat. Photon., 14, 256–262, 2020

[24] A. G. Kalampounias, et al, Glass-forming ability of TeO_2 and temperature induced changes on the structure of the glassy, supercooled, and molten states, J. Chem. Phys. 142, 154503 (2015)

[25] R. Nayak, et al, Optical waveguiding in amorphous tellurium oxide thin films, Thin Solid Films, 445, 118–126, 2003

[26] J.C. Champarnaud-Mesjard, et al, Crystal structure, Raman spectrum and lattice dynamics of a new metastable form of tellurium dioxide: γ-TeO_2, Journal of physics and chemistry of solids, 61(9), 1499-1507, 2000

[27] T. Vasileiadis, et al, Photo-induced oxidation and amorphization of trigonal tellurium: A means to engineer hybrid nanostructures and explore glass structure under spatial confinement, Journal Of Applied Physics 116, 103510, 2014

[28] C. Ríos, M. Stegmaier, P. Hosseini, D. Wang, T. Scherer, C.D. Wright, H. Bhaskaran, W. Pernice, Integrated all-photonic non-volatile multi-level memory. Nature photonics 9, 11, 725-732, 2015

[29] C. Castellan, et al, Tuning the strain-induced resonance shift in silicon racetrack resonators by their orientation. Optics express 26(4), 4204-4218, 2018

[30] Y. Xie, et al, Thermally-Reconfigurable Silicon Photonic Devices and Circuits, IEEE Journal of Selected Topics in Quantum Electronics, 26, 5, 1-20, 3600220, 2020

[31] Q. Xu, S. Manipatruni, B. Schmidt, J. Shakya, M. Lipson, "12.5 Gbit/s carrier-injection-based silicon micro-ring silicon modulators." Optics Express 15(2) 430-436, 2007

Chapter 6

LASER WRITING ENABLED DEVICE PATTERNING AND MATERIAL PHASE CHANGE

6.1 Introduction

Chalcogenides (ChG) are those types of materials that contain one or more chalcogen elements from group VI in the periodic table. They have the unique optical properties of infrared transparency, nonlinearity, and photosensitivity [1]. This makes chalcogenide materials have wide photonic applications such as infrared sensing, optical signal processing, and reconfigurable photonic devices [1]-[7]. The Direct laser writing (DLW) technique interacting with Chalcogenide materials could provide flexible and low-cost ways for versatile mask-free micro-fabrication and material processing [8]-[16]. In the past, there are limited studies on how to reduce the feature size of writing patterns and in the parallel process the nanomaterials. And most studies using DLW only focus on single-point dosage tests [8][14][17].

In this work, a nanosecond sub-bandgap near-infrared laser was used to conduct power-dependent ablation and phase change on chalcogenide materials. By controlling the pulsed laser dosages such as intensities, exposed pulse numbers unit time, and repetition rates, the effects on feature size reduction for device patterning and material phase change were studied. A variety of materials from dielectric materials to chalcogenide semiconductors have been tried for the dosage study to reduce the feature size. Based on the phase change nature of some chalcogenide materials ($Ge_2Sb_2Te_5$), it is able to achieve applications of laser-patterned tunable devices, such as gratings.

6.2 Experiment results

6.2.1 Experimental setup schematics

Figure 6.1 shows the schematics of the experiment setup. Three optical pathways are coupled onto the sample for alignment, illumination, and laser writing. A low-power (< 4 mW) HeNe laser (633 nm) is used for optical alignment (red pathway). A pulsed HIPPO Nd:YAG laser (center wavelength 1064 nm, pulse duration of 10 ns, repetition rate of 10k Hz-500kHz, and duty cycle of 0.05%) is focused onto the sample using a NIR objective (Mitutoyo, 50×, NA=0.42)(grey path in Figure 6.1). The objective reduces the diameter of the Gaussian beam from 0.6 mm to 6 μm. A collimated white light is used to illuminate the sample. After reflecting from the sample, it couples into a CCD camera for getting real-time images of the patterned sample (yellow path in Figure 6.1). The sample is mounted on a motion stage (Physics Instruments) with automatic translation controls in the x, y, and z directions with 50 nm spatial resolution and a 1 cm traveling distance. The speed, direction, and distance of stage movement can be programmed on the computer.

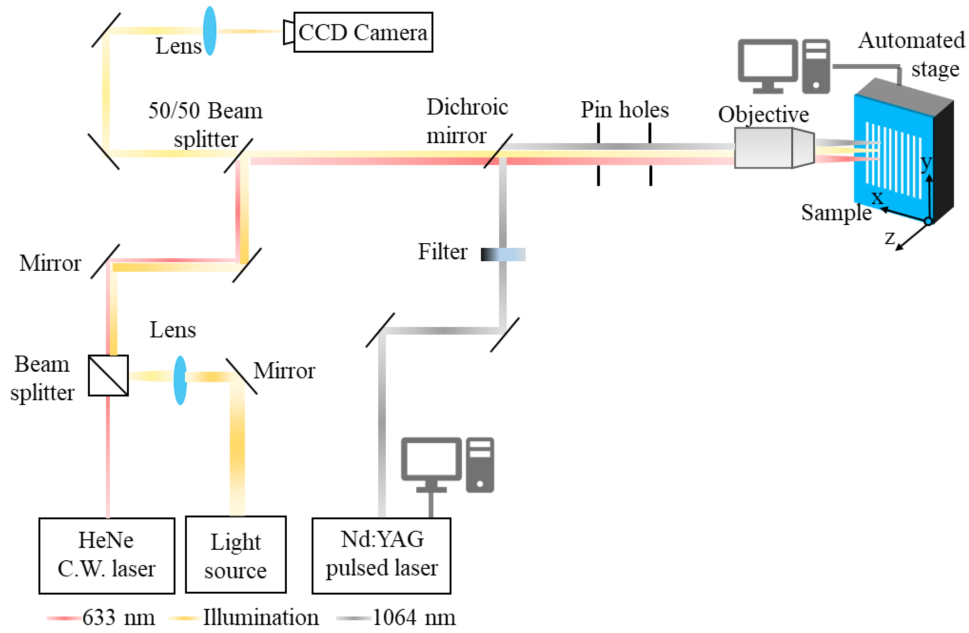

Figure 6.1 Schematics of Laser writing setup. Three well-aligned light sources (633 nm c.w. laser, illumination light, 1064 nm pulsed laser) are coupled onto the sample for alignment, illumination, and laser writing purposes, respectively. Reprinted/Adapted with permission from [25] © Optica Publishing Group.

6.2.2 Laser dosage study on different materials

Several materials from dielectrics to semiconductors are used for patterning and dosage study to realize small feature size: sapphire, Titanium-coated Lithium Niobate (Ti-LN), chalcogenide compounds $Ge_{23}Sb_7S_{70}$ and $Ge_2Sb_2Te_5$ [18][19]. Sapphire and Titanium-coated Lithium Niobate (Ti-LN) are bulk film samples (thickness of 500 µm). $Ge_2Sb_2Te_5$ and $Ge_{23}Sb_7S_{70}$ powders are purchased off-the-shelf as source material (Irradiance glass. Inc.), then deposited in a Physical Vapor Deposition chamber at room temperature to have the thickness of 80 nm and 450 nm, respectively [19]. Smooth straight lines are obtained by carefully adjusting the laser power level and the speed of the motion stage (Figure 6.2).

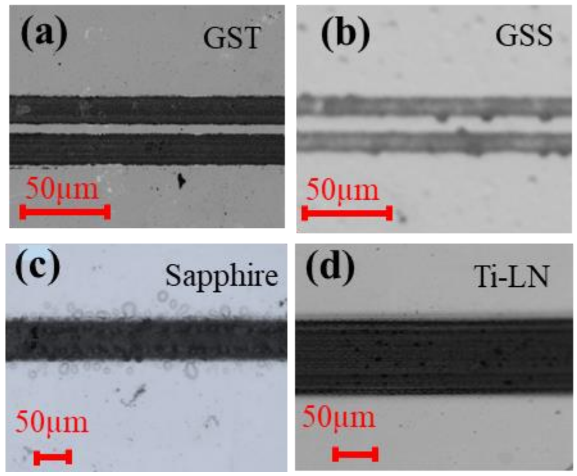

Figure 6.2 Optical images of writing inscriptions on (a) GST, (b) GSS, (c) Sapphire, and (d) Ti-LN. Reprinted/Adapted with permission from [25] © Optica Publishing Group.

To reduce the feature size, a dosage study is conducted by varying different parameters of laser pulses: pulse energy, speed of the motion stage (to reduce the exposure time of each pulse on samples), and repetition rate [20]. A surface profilometer (Dektak XT, Bruker) is used to measure the linewidth profiles of laser inscription. The width of the feature size under different parameters for those materials can be seen in Figure 6.3. First, we set the laser power levels in the range from 0 to 0.8 mJ/pulse under the same motion stage of 5mm/s and a repetition rate of 15 kHz. As the pulse energy decreases, the linewidth has a significant reduction for all materials (Figure 6.3(a)). Then keeping laser pulse energy at 0.4 mJ/pulse and a repetition rate of 15 kHz, a motion speed range of 1~12 mm/s is set. As the speed increases, the exposure time on the sample unit length is decreased and the linewidth reduces (Figure 6.3(b)). Results in Figure 6.3(b) are not the optimal results for each material, only show a varying trend. Later, under a higher repetition rate (for GST) from 150~450 kHz, and the constant laser pulse energy at 0.4 mJ/pulse and motion stage of 10 mm/s, the linewidth can be significantly reduced (Figure 6.3(c)). This is because a higher repetition rate will induce more pulse numbers in unit time, and further reduce the interaction time of each pulse with materials. From the dosage study on those materials, GST can achieve a small feature size down to 6 μm (based on results from Figure 6.3(a)(b)). In addition, owing to the attractive phase change material property, we further choose GST as the main material to study the application of laser writing.

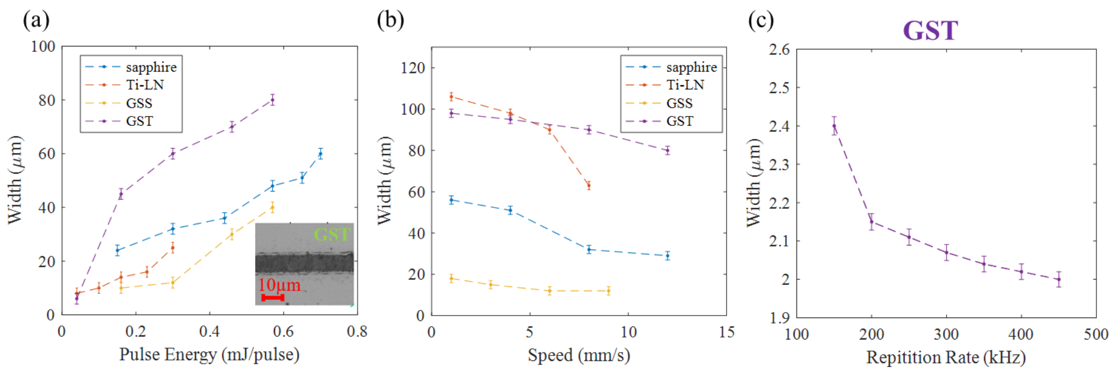

Figure 6.3 Laser dosage study for reduced feature sizes under (a) different pulse energy levels, under a constant speed of 5 mm/s and constant repetition rate 15 kHz; (b) different speeds under pulse energy of 0.4 mJ/pulse and constant repetition rate 15 kHz, and (c) different repetition rates, under the constant pulse energy of 0.4 mJ/pulse and constant speed of 10 mm/s. (a) and (b) are for a series of materials from dielectric materials to semiconductors. (c) is for GST only. Reprinted/Adapted with permission from [25] © Optica Publishing Group.

6.2.3 Laser-induced phase transition for $Ge_2Sb_2Te_5$

$Ge_2Sb_2Te_5$ is a kind of Chalcogenide compound that has unique optical properties. For the amorphous phase of GST, it can be converted into the poly-crystalline phase by adding a stimulus. By adding a stimulus of different parameters, it can reversely go back to the amorphous phase (Figure 6.4) [3][21][22]. The material doesn't need continuous stimulus to maintain the current phase (as non-volatile). The two states have a large contrast in refractive index (Δn>1) (Figure 6.5) that could be widely used in optical switches, memories, and reconfigurable devices [4]-[7].

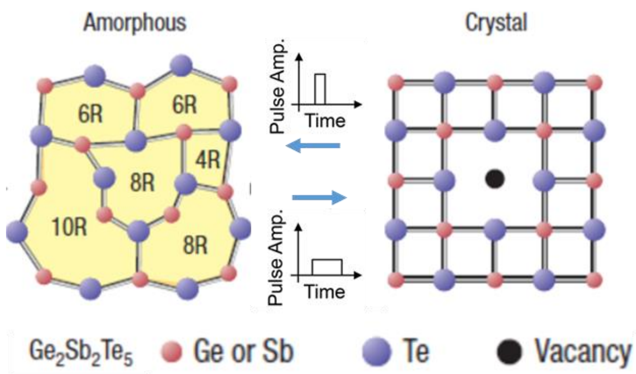

Figure 6.4 Schematics of GST phase change [22].

In this work, GST was deposited on a glass substrate as the amorphous state by using Physical Vapor Deposition [19]. After baking it at 200℃ over its phase change temperature (around 150℃), it converted to the crystalline phase. And the two phases have distinct refractive index contrast from visible to near-infrared wavelength, measured by Ellipsometer (Figure 6.5).

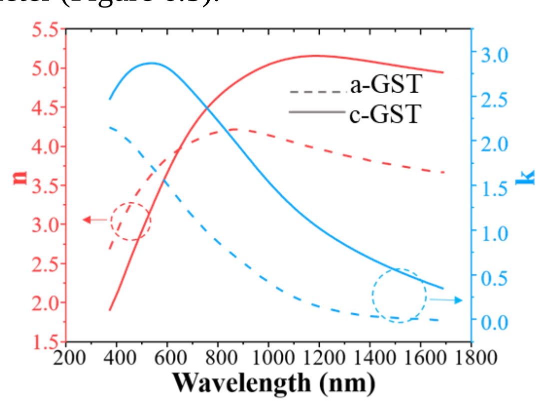

Figure 6.5 Measured Refractive index (n,k) of GST thin film before (a-GST) and after baking (c-GST) at 200°C. Reprinted/Adapted with permission from [25] © Optica Publishing Group.

For the laser interaction with thin film GST, transition regimes from the phase change to the laser ablation (e.g. non-thermal melting, thermal phase melting, and ablation) are determined by the increasing laser pulse energies (Figure 6.6(a)) [17][23]. At the very low laser pulse energies (level I in Figure 6.6(a)), the light-matter interaction leads to a phase transition in GST that enables a very slight volumetric effect and high-contrast photonic patterns (Figure 6.6(a)(b)). In this stage, a partial crystalline phase transition occurs on the top surface of an a-GST thin film. As the laser pulse energies increase (level II in Figure 6.6(a)), crystalline GST could melt so that the reflow process forms the cross-section profile [23]. At the high pulse energies (level III in Figure 6.6(a)), the GST would be completely ablated around the center of the beam [17]. The topology of the different regimes of the patterned GST under increasing pulsed energy levels is present in Figure 6.6(a). Regions labeled ii or iii in Figure 6.6(a) are crystalline states, while regions labeled i are amorphous GST. Figures 6.6(b) and (c) show the perspective view in the optical image and SEM image for the regime of level I. Figure 6.6(d) shows the optical images for the regime of level II and level III.

Raman characterization is used to study the laser-written GST for the regime of level II (Figure 6.6(e)). Three Raman peaks are shown for a-GST (black curve in Figure 6.6(e)). The dotted and solid red curves are c-GST in the reflow (ii) and middle region (iii) of the laser-exposed regions. Raman peaks for the metastable face-centered cubic (fcc) state of c-GST are shown in the ii and iii regions. Only the stable hexagonal close-packed (hcp) lattice structure is existed in region iii [24]. The phase transition temperature from the amorphous state to the crystalline fcc state is around 150°C, while the stable hcp structure starts to appear over 220°C [24]. The cross-sectional profile by AFM shows the thicker c-GST on the side than in the middle region (Figure 6.6(f)). For the laser pulse energies higher than 32 μJ (threshold energy level) (Figure 6.6(d)), the c-GST in the middle is totally ablated, transiting the regime from level II to level III. This is consistent with the prior work [17][23][24].

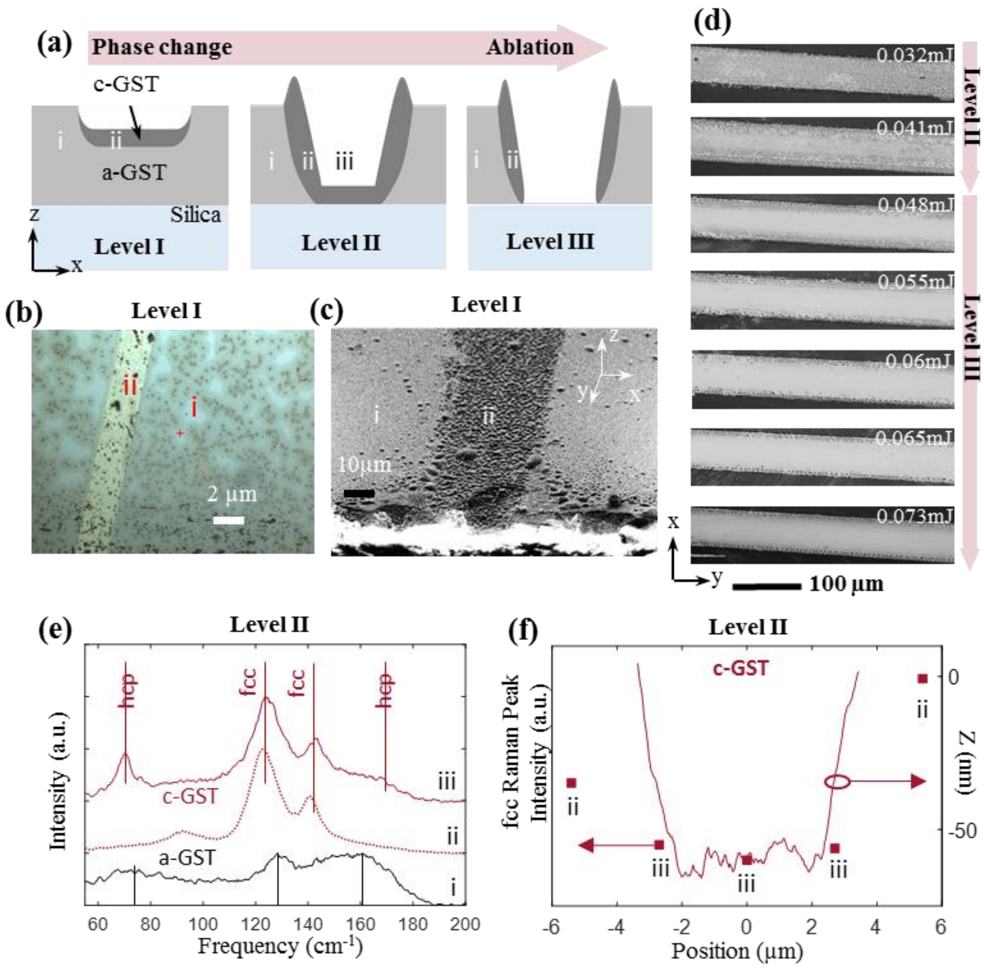

Figure 6.6 Laser-induced phase transitions and ablation on GST. (a) Schematics of GST state evolution under low (I), medium (II), and high (III) laser pulse energy dosage. The dark grey(ii), light gray(i) and blue areas represent crystalline, as-deposited amorphous GST and silica substrate respectively. (b) Optical imaging, and (c) SEM imaging of laser-induced phase transitions on GST at pulse energy level I indicated in (a). Note lines in (b) and (c) are not the same ones from laser writing, but both have the Raman spectra as Region ii in (e). (d) Laser-induced ablation on GST at higher power levels (II & III). (e) Normalized Raman spectra of GST sample exposed to laser pulse energy at the level I and II. Regions ii and iii are c-GST and region i is a-GST. (f) Raman fcc peak of c-GST (Red solid square dots) and cross-sectional profile in the z-direction (red curve) versus position along the x-axis for power levels II. The GST profile is obtained at the translation speed of 5 mm/s and laser pulse energy of 30 μJ. Reprinted/Adapted with permission from [25] © Optica Publishing Group.

6.2.4 Device patterning on Chalcogenide $Ge_2Sb_2Te_5$

Based on the dosage study results and unique material properties of GST, we adopt the laser writing technique to fabricate some basic planar photonic devices for proof-of-concept, such as gratings and metalens [20][25]. By changing the phase of GST, the patterned devices will have tunable optical responses, such as tunable gratings for sub-bandgap spectra applications and tunable focal length metalens. The rest of the contents will discuss the measurement results on grating structures.

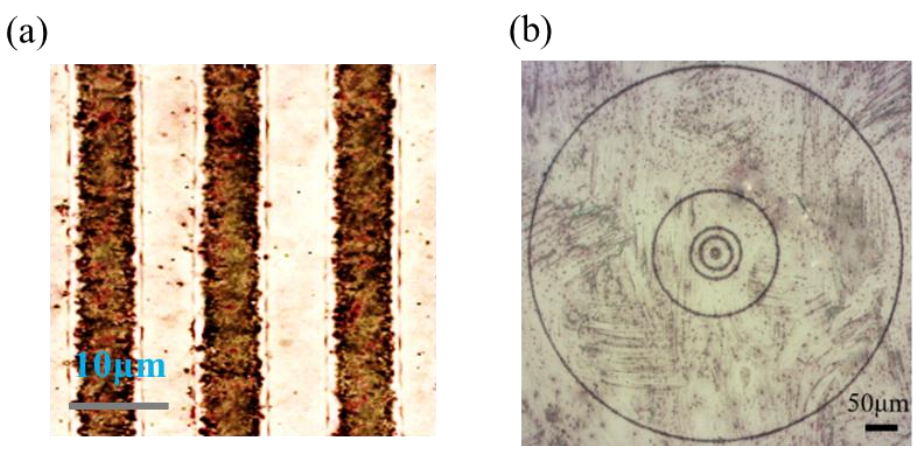

Figure 6.7 Laser patterning on GST to form (a) gratings [25], and (b) metalens [20].

Here, a laser-patterned grating structure with a micrometer scale is studied by characterizing its reflection spectra using Fourier transform infrared spectroscopy (FTIR) [26][27]. Unpatterned GST thin film before (a-GST) and after baking (c-GST) is measured as a reference compared with patterned GST structures (Figure 6.8(b), Figure 6.9). For unpatterned thin film GST samples, the reflection after baking to transit into the crystalline state (c-GST) is higher than before baking (a-GST) [21].

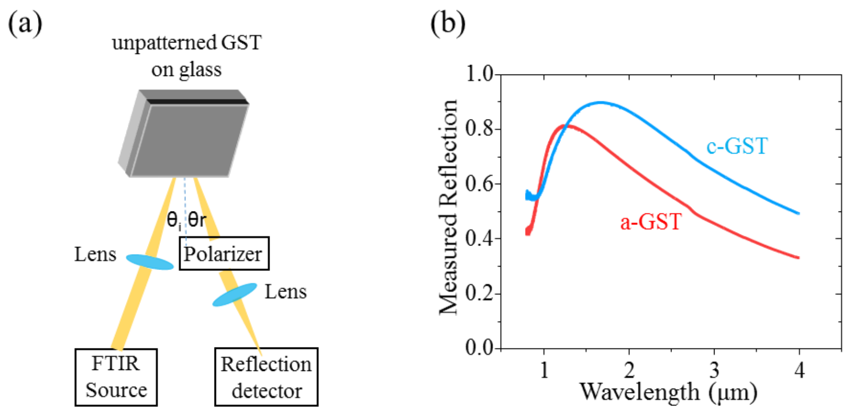

Figure 6.8 (a) Schematic of FTIR for angled reflection measurements on unpatterned GST sample. (b) The measured reflection spectrum of unpatterned thin film a-GST and c-GST samples. Reprinted/Adapted with permission from [25] © Optica Publishing Group.

To have a smooth structure, the optimized laser pulse energy (25~26 μJ) and stage speed (10 mm/s) is adopted for reducing the feature size on a-GST samples (referring to laser pulse energy level II in Figure 6.6(a)). Gap linewidths of 6 μm and 9 μm were formed under laser exposure pulse energies of 25 and 26 μJ, respectively (Insets of Figure 6.9(b)). The GST strip width is written to be 8 μm. The two samples exhibit similar reflection spectra for the first-order diffraction peak with a maximum reflection at the wavelength of around 1.7 μm. The reflection spectra show higher reflectivity for gratings with a larger lattice constant (Figure 6.9(b)). The measurement results are consistent with the numerical simulations (Figure 6.9(c)). The simulated cross-sectional mode profile around 1.7 μm shows that the highest electric field intensity is located around the side edge of the a-GST strips. For the patterned grating with the lattice constant (a) of 14 μm, the reflection spectrum is measured after baking it at 200°C. The patterned GST grating turns into the all-crystalline structure (insets in Figure 6.9(d)) with an increased reflection spectrum. This is consistent with simulated results (Figure 6.9(e)). Tunable grating structures of laser writing GST under different laser pulsed energies and different phases of GST are demonstrated.

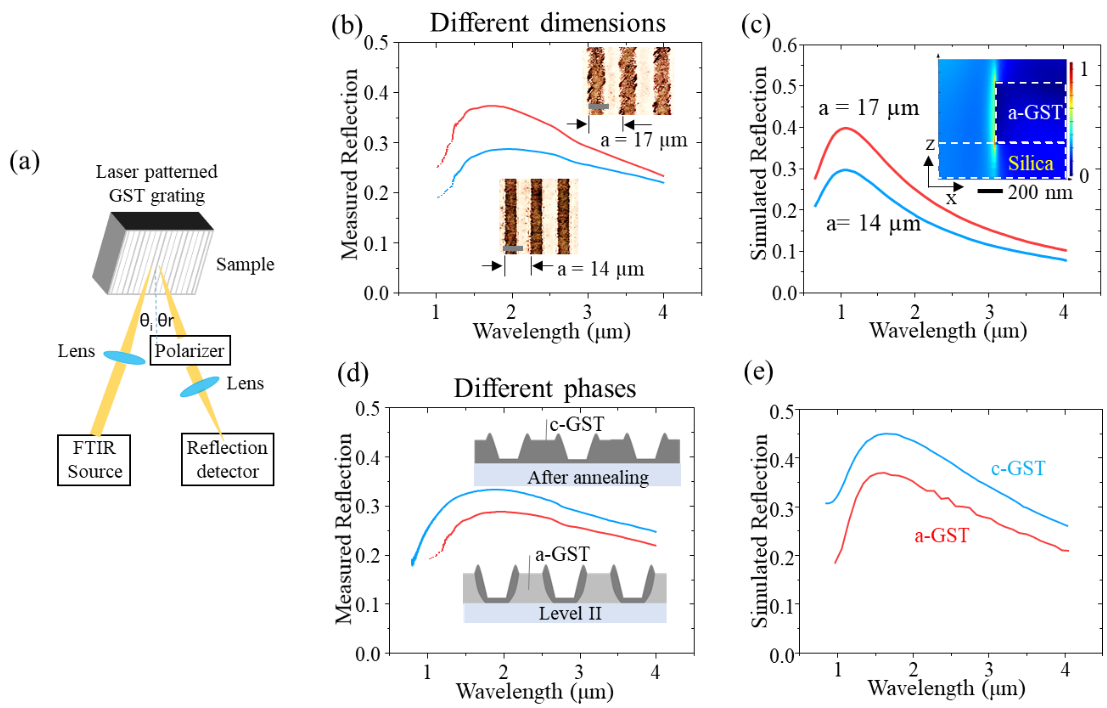

Figure 6.9 Measured and simulated reflection spectra of laser writing GST grating. (a) Schematic of FTIR setup for angled reflection measurements. The incident angle $\theta_i = 5°$. The reflection angle θ_r=25°. (b) Measured and (c) simulated reflection first-order diffraction spectra of the laser inscribed ChG grating (a-GST) has the lattice constant of 17 μm (red curve) and 14 μm (blue curve). The GST strip width is 8 μm for both devices. The laser energy levels are 25~26 μJ (level II in Figure 6.6(a)). Insets in (b): microscope images of a correspondent device (Scale bar: 10 μm). Inset in (c) Cross-sectional optical mode profile near the edge of the grating. (d) Measured and (e) simulated first-order diffraction spectra before and after GST phase change for the grating with a lattice constant of 14 μm, fabricated with laser energy of 25 μJ. Insets in (d): Cross-sectional schematics of the laser-patterned GST grating before (red curve) and after (blue curve) baking at 200°C. The light and dark grey represent the a- and c-GST regions, respectively. Reprinted/Adapted with permission from [25] © Optica Publishing Group.

6.3 Summary

In this chapter, the direct laser writing technique for micro-device patterning and material phase transition is demonstrated. By choosing an optimized pulsed laser dosage, the infrared laser can have the sub-bandgap patterning features to form high-contrast photonic features across dielectric and semiconductor materials. Under controlled exposure dosages, the nanosecond laser can have transition regimes from the non-thermal phase change to the thermal ablation on chalcogenide materials. Without the need for the mask, planar patterns like gratings are generated on phase change material GST. And the reflection spectra could be tunable by controlling its geometry spacing or transiting its phase for reconfigurable device applications.

REFERENCES

[1] B. J. Eggleton, et al, Chalcogenide photonics, Nat. Photonics, 5, 141–148, 2011

[2] S. V. Makarov, et al, Light-Induced Tuning and Reconfiguration of Nanophotonic Structures, Laser Photonics Rev., 11, 1700108, 2017

[3] S. Abdollahramezani, et al, Tunable nanophotonics enabled by chalcogenide phase-change materials, Nanophotonics, 9(5), 1189–1241, 2020.

[4] C. Ríos, et al, Color Depth Modulation and Resolution in Phase - Change Material Nanodisplays, Adv. Materials, 28, 4720-4726, 2016

[5] A. V. Pogrebnyakov, et al, Reconfigurable near-IR metasurface based on $Ge_2Sb_2Te_5$ phase-change material, Opt. Mat. Express, 8(8), 2264-2275, 2018

[6] P. Pitchappa, et al, Chalcogenide phase change material for active terahertz photonics, Advanced Materials, 31(12), 1808157, 2019

[7] K. Chaudhary, et al, Polariton Nanophotonics using Phase Change Materials, Nature Communications, 10, 4487, 2019

[8] Q. Zhang, et al, Nanogratings and nanoholes fabricated by direct femtosecond laser writing in chalcogenide glasses," Opt. Express 18(7), 6885-6890, 2010

[9] R. R. Gattass, et al, Femtosecond laser micromachining in transparent materials, Nat. Photonics 2, 219–225, 2008

[10] F. Chen, et al, Optical waveguides in crystalline dielectric materials produced by femtosecond - laser micromachining, Laser Photonics Rev. 8(2), 251 - 275, 2014

[11] E. Zgraggen, et al, Laser direct writing of single-mode polysiloxane optical waveguides and devices, Journal of Lightwave Technology, 32(17), 3036-3042, 2014

[12] M. Deubel, et al, Direct laser writing of three-dimensional photonic-crystal templates for telecommunications, Nature Mater. 3, 444–447, 2004

[13] M. Farsari, et al, Materials processing: two-photon fabrication, Nature Photon. 3, 450–452, 2009

[14] X. Liu, et al, Laser ablation and micromachining with ultrashort laser pulses, IEEE journal of quantum electronics 33(10), 1706-1716, 1997

[15] M. Kang, et al, Refractive index patterning of infrared glass ceramics through laser-induced vitrification, Opt. Mat. Express, 8(9), 2722-2733, 2018

[16] T. Gretzinger, et al, Ultrafast laser inscription in chalcogenide glass: thermal versus athermal fabrication, Opt. Mat. Express, 8(12), 2862-2877, 2018

[17] C. H. Chu, et al, Laser-induced phase transitions of $Ge_2Sb_2Te_5$ thin films used in optical and electronic data storage and in thermal lithography, Opt. Express, 18(17), 18383–18393, 2010.

[18] F. Christensen, et al, Sub-band-gap laser micromachining of lithium niobate. Applied physics letters, 66, 2772-2773, 1995

[19] A. Soman, Optimizing fabrication techniques of materials and devices for integrated nanophotonics, University of Delaware ProQuest Dissertations Publishing, 2019. 13883053.

[20] B. Sun, Laser direct writing metalens with phase change material and application, University of Delaware ProQuest Dissertations Publishing, 2021. 28315201

[21] M. Wuttig, et al, Phase-change materials for non-volatile photonic applications, Nat. Photonics 11(8), 465–476, 2017

[22] M. Wuttig et al, Phase-change materials for rewriteable data storage, Nature Materials, 6, 824–832, 2007

[23] K. Phillips, et al, Ultrafast laser processing of materials: a review, Adv. Opt. Photonics 7(4), 684–712, 2015.

[24] P. Guo, et al, Improving the performance of $Ge_2Sb_2Te_5$ materials via nickel doping: Towards RF-compatible phase-change devices, Appl. Phys. Lett., 113(17), 171903, 2018.

[25] D. Mao, et al, Sub-bandgap pulsed laser patterning of planar chalcogenide microphotonics, Optical Materials Express, 10, (9), 2126-2134, 2020

[26] D. Wei, et al, Single-material semiconductor hyperbolic metamaterials, Opt. Express 24(8), 8735–8745, 2016.

[27] P. Sohr, et al, Simultaneous large mode index and high quality factor in infrared hyperbolic metamaterials, ACS Photonics, 5(10), 4003–4008, 2018

Chapter 7

SUMMARY AND FUTURE WORK

7.1 SUMMARY

This thesis presents a few topics related to silicon photonics: performance evaluation of silicon Mach-Zehnder Modulators after cosmic radiation; hybrid integration of some low-dimensional materials (Graphene, Tellurium) on silicon platforms for applications of high-speed optoelectronic devices and all-optical trimming devices. Finally, a nanosecond direct laser writing platform is demonstrated to have low-cost, mask-free device patterning and material phase change.

First, the performance change of silicon MZMs after cosmic radiation was investigated. Low-cost and compact silicon photonics chips may be used in laser communication in aerospace in the future, replacing conventional bulky, data-rate-limited RF communications. While the performance reliability of silicon photonics devices against cosmic radiation is unknown. Silicon chips including MZMs were loading in the forward direction of ISS for 1 year of cosmic radiation. After that, device performance was re-evaluated and compared with the one before radiation. 90% of devices in the same die can work normally after cosmic radiation. Optical transmission spectra, electrical response (I-V, C-V), EO (DC) response, and the high-speed response of MZMs have been measured and analyzed. Increased effective index (on the order of 10^{-3}), and increased dark current are observed. It also shows that a reduced carrier recombination lifetime of about 50% leads to a nearly doubled 3dB bandwidth of high-speed response. Possible solutions against the radiation effect are suggested. This work paves the fundamental step for future deploying silicon photonics integrated circuits for space optical communications.

Secondly, directly contacted graphene silicon hetero-junction was analyzed by a small signal model for high-speed optoelectronic applications. For direct-contacted graphene silicon hetero-junction, the voltage-dependent hetero-junction variations are studied by fitting the small-signal model to the broadband RF response. The fitted results show the junction variations which is most significant for hetero-junction capacitance in *G-n*/Si region. This is consistent with the simulated built-in electric field which also has the largest variation in the same *G-n*/Si interface under increasing forward bias. It indicates that the forward bias could change the G doping levels, vertical built-in electric field, and junction capacitance on G and Si interface, with the RC constant of 1.5ps or even smaller. This result can be used for designing RC constant limited high-speed optoelectronic devices based on the Si platform.

Following the configuration of directly contacted G-Si hybrid structure, device modeling of G-Si modulators is numerically studied. Modulating graphene's carrier density by biasing silicon substrate, built-in electric field enables reduced RC constant and ultrafast carrier transportation in G between G-Si interface for highly efficient and high-speed operation. The designed G-Si interface and optimized doping profiles show that the hybrid G-Si Mach-Zehnder modulator (MZM) exhibits a very low $V_{\pi}{\cdot}L$ of 1.19 V·mm and high-speed response at least 59 GHz for efficient and high-speed modulator applications.

Thirdly, the photorefractive effect of Tellurium (Te) is investigated. Tellurium nanowire was predicted to have strong optical nonlinearity (such as second-order susceptibility), but there is no work to experimentally discover whether thin-film

Tellurium possesses other nonlinearity, such as the Photorefractive effect. In this work, the Tellurium flake was transferred to a silicon ring resonator with low loss and high-quality factor to probe the nonlinearity. An obvious photorefractive effect was discovered under the increasing input optical power. Raman spectra verified that the laser-irradiated Tellurium flake got oxidized to TeO_2 which has a lower refractive index than Te. Partial oxidation of Te thin film to glassy-TeO_2 leads to the reduced refractive index for the resonance blue shift. This can be used for wavelength trimming for undesired fabrication randomness of MRRs in chip-scale photonic applications.

Lastly, a nanosecond laser writing platform for micro-device patterning and material phase change is demonstrated. By controlling the laser dosages, different regimes of laser material interactions from ablation to non-thermal melting are demonstrated. The platform enables low-cost and mask-free sub-bandgap device patterning at the micrometer scale. And it could have material phase change on some chalcogenide material $Ge_2Sb_2Te_5$ for tunable device applications.

7.2 FUTURE OUTLOOK

Some topics in some chapters could be extended for future study.

For the Graphene silicon modulators, experimental parts could be conducted and further studied. The high modulation efficiency of directly contacted graphene silicon modulators should be evaluated and studied.

For the reliability of silicon devices after the harsh environment, this work only focuses on the permanent changes in the device performance after cosmic radiation. The real-time in-situ study of the performance change could be explored in future if possible. The real-time testing platform (hardware, software) needs to be customized and designed. For the contents in the Chapter, the silicon chip was only placed on the RAM (forward direction) side of ISS. The impact on the performance of the silicon chip if it is placed on the other side (e.g., back, side) of ISS is still unknown. This could be further investigated in future.

For the Tellurium-based devices, Pockels effect modulators could be explored.

For the direct laser writing technique, as the patterning resolution is dependent on the laser wavelength, a smaller wavelength, e.g., 532 nm, could be used to further reduce the writing feature size by adding the second harmonic generation head in front of the laser output port.

Appendix A

COPYRIGHT PERMISSION

Work presented in chapter 4, section 4.2 “Small signal analysis for RC constant limited Graphene silicon optoelectronics” has been published in: *ACS Applied Electronic Materials*, 1, 2, 172–178, (2019).

Work presented in chapter 4, section 4.3 “Device Modeling of directly contacted Graphene Silicon Modulators” has been published in: *IEEE Journal of Selected Topics in Quantum Electronics*, 27, 2, 1–9, (2020).

Work presented in chapter 6 “Laser Writing Enabled Device Patterning And Material Phase Change” has been published in: *Optical Materials Express*, 10, 9, 2126-2134, (2020).

Permission information is listed below.

RightsLink

Home Help Live Chat Sign in Create Account

Bandwidth Limitation of Directly Contacted Graphene–Silicon Optoelectronics

Author: Dun Mao, Thomas Kananen, Tiantian Li, et al

Publication: ACS Applied Electronic Materials

Publisher: American Chemical Society

Date: Feb 1, 2019

PERMISSION/LICENSE IS GRANTED FOR YOUR ORDER AT NO CHARGE

This type of permission/license, instead of the standard Terms and Conditions, is sent to you because no fee is being charged for your order. Please note the following:

- Permission is granted for your request in both print and electronic formats, and translations.
- If figures and/or tables were requested, they may be adapted or used in part.
- Please print this page for your records and send a copy of it to your publisher/graduate school.
- Appropriate credit for the requested material should be given as follows: "Reprinted (adapted) with permission from {COMPLETE REFERENCE CITATION}. Copyright {YEAR} American Chemical Society." Insert appropriate information in place of the capitalized words.
- One-time permission is granted only for the use specified in your RightsLink request. No additional uses are granted (such as derivative works or other editions). For any uses, please submit a new request.

If credit is given to another source for the material you requested from RightsLink, permission must be obtained from that source.

BACK CLOSE WINDOW

CCC RightsLink

Home | Help | Live Chat | Dun Mao

IEEE Requesting permission to reuse content from an IEEE publication

Device Architectures for Low Voltage and Ultrafast Graphene Integrated Phase Modulators

Author: Dun Mao

Publication: IEEE Journal of Selected Topics in Quantum Electronics

Publisher: IEEE

Date: March-April 2021

Thesis / Dissertation Reuse

The IEEE does not require individuals working on a thesis to obtain a formal reuse license, however, you may print out this statement to be used as a permission grant:

Requirements to be followed when using any portion (e.g., figure, graph, table, or textual material) of an IEEE copyrighted paper in a thesis:

1) In the case of textual material (e.g., using short quotes or referring to the work within these papers) users must give full credit to the original source (author, paper, publication) followed by the IEEE copyright line © 2011 IEEE.
2) In the case of illustrations or tabular material, we require that the copyright line © [Year of original publication] IEEE appear prominently with each reprinted figure and/or table.
3) If a substantial portion of the original paper is to be used, and if you are not the senior author, also obtain the senior author's approval.

Requirements to be followed when using an entire IEEE copyrighted paper in a thesis:

1) The following IEEE copyright/ credit notice should be placed prominently in the references: © [year of original publication] IEEE. Reprinted, with permission, from [author names, paper title, IEEE publication title, and month/year of publication]
2) Only the accepted version of an IEEE copyrighted paper can be used when posting the paper or your thesis on-line.
3) In placing the thesis on the author's university website, please display the following message in a prominent place on the website: In reference to IEEE copyrighted material which is used with permission in this thesis, the IEEE does not endorse any of [university/educational entity's name goes here]'s products or services. Internal or personal use of this material is permitted. If interested in reprinting/republishing IEEE copyrighted material for advertising or promotional purposes or for creating new collective works for resale or redistribution, please go to http://www.ieee.org/publications_standards/publications/rights/rights_link.html to learn how to obtain a License from RightsLink.

If applicable, University Microfilms and/or ProQuest Library, or the Archives of Canada may supply single copies of the dissertation.

BACK CLOSE WINDOW

Permission from Optica:

G Suite

Dun Mao <dmao@udel.edu>

Inquiry for copyright admission

Optica Publishing Group Copyright <copyright@osa.org> Wed, Nov 9, 2022 at 3:06 PM
To: Dun Mao <dmao@udel.edu>, Optica Publishing Group Copyright <copyright@osa.org>

Dear Dun Mao,

Thank you for contacting Optica Publishing Group.

For the use of material from Dun Mao, Mingkun Chen, Xiangyu Ma, Anishkumar Soman, Huadan Xing, Thomas Kananen, Nathan Augenbraun, Chen Cheng, Matthew Doty, and Tingyi Gu, "Sub-bandgap pulsed laser patterning of planar chalcogenide microphotonics," Opt. Mater. Express 10, 2126-2134 (2020):

> Because you are the author of the source paper from which you wish to reproduce material, Optica Publishing Group considers your requested use of its copyrighted materials to be permissible within the author rights granted in the Copyright Transfer and Open Access Publishing Agreement submitted by the requester on acceptance for publication of his/her manuscript. It is requested that a complete citation of the original material be included in any publication. This permission assumes that the material was not reproduced from another source when published in the original publication.
>
> If the entire article is being included, it is permissible to use the **version of record**.

While your publisher should be able to provide additional guidance, we prefer the below citation formats:

> For citations in figure captions:
>
> [Reprinted/Adapted] with permission from [ref **#**] © Optica Publishing Group. (Please include the full citation in your reference list)
>
> For images without captions:
>
> Journal Vol. **#**, first page (year published) An example: Opt. Express 19, 2720 (2011)

Please let me know if you have any questions.

Kind Regards,

Hannah Greenwood

Hannah Greenwood